NOVEL APPROACHES FOR MANIPULATION OF MAGNETIZATION IN SPINTRONIC APPLICATIONS

Mehrdad Elyasi

(*B.Sc., Sharif University of Technology, Tehran, Iran*)

A THESIS SUBMITTED

FOR THE DEGREE OF DOCTOR OF PHILOSOPHY

DEPARTMENT OF ELECTRICAL AND COMPUTER ENGINEERING

NATIONAL UNIVERSITY OF SINGAPORE

2016

DECLARATION

I hereby declare that the thesis is my original work and it has been written by me in its entirety. I have duly acknowledged all the sources of information which have been used in the thesis.

This thesis has also not been submitted for any degree in any university previously.

Mehrdad Elyasi
4th November 2016

Acknowledgement

I would like to express my sincere gratitude towards my PhD supervisors, Professor Charanjit Singh Bhatia and Professor Hyunsoo Yang. The research content of this thesis would have not been existent without the extensive support of Professor Bhatia and Professor Yang. I greatly appreciate the liberty and support that I was granted for pursuing the research topics that interested me, and following the ideas that eventually became fruitful and formed the contents of this thesis.

Special acknowledgement goes to my funding organization, Singapore Agency for Science, Technology and Reseacrh (A*STAR), that believed in me and awarded me with Singapore International Graduate Award (SINGA) scholarship, covering all my expenses throughout my PhD studies.

I thank the executive and research staff of A*STAR Institute of Microelectronics (IME), who sincerely supported me in the time I carried out a part of my PhD there. In that regard, I specially thank Professor Dim-Lee Kwong, Professor Chengkuo Lee and Dr. Vincent Pot.

My sincere full-heartedly appreciation is for the colleagues whom I shared the Spin and Energy Lab (SEL) office and cleanroom with them in the majority of my PhD studies. The energetic, motivated, respectful, and friendly environment of our research group provided a smooth and constructive research life for me.

It is a difficult task to put in words my gratitude for the contribution of my parents to all chapters of my life including my PhD studies. The emotional and mental support from these two beautiful people has kept my heart warm, and a smile of satisfaction on their kind faces has been a great reward for my achievements. I thank my brother and sister for being kind and supportive, and I thank my niece and nephew for being born and being two beautiful symbols of hope for me. I thank all

the people whom I loved, love and will love, as for great achievemnets nothing is more inspirational than love.

Table of contents

Summary

In this thesis, some obstacles in the data retention mechanisms in magnetism are addressed, and a number of methods for manipulation of spin in different contexts has been developed. Utilizing excitation of collective modes with microwave irradiation or microwave modulated spin-polarized currents for selective manipulation of magnetization in magnetic nanodot matrices, in the context of hard disk technology (also magnonic crystals) and magnetic random access memories is explored. A synchronization method for spin-Hall oscillators is developed. An ultrafast all-optical switching mechanism combining the concepts of spin-orbit interaction and diffusive transport is demonstrated. Lastly, a novel perspective for manipulation of spin wave propagation is used to cloak magnons with introducing transformation magnonics, paving the way for novel switching mechansims. Each of the chapters in the body of the thesis contains a proposal for a novel mechanism, followed by theoretical and/or numerical proof of concept and analysis for the effects of important system parameters.

List of figures

List of abbreviations

AOS: all-optical switching

DMI: Dzyaloshinskii-Moryia interaction

DW: domain wall

EM: electromagnetic

FFT: fast Fourier transform

FM: ferromagnet

FMR: ferromagnetic resonance

GMR: giant magnetoresistance

HDD: hard disk drive

IF: inverse Farday

IP: in-plane

ISHE: inverse spin-Hall effect

LLG: Landau-Lifshitz-Gilbert

MAMR: microwave assisted magnetization reversal

MRAM: magnetic random access memory

MTJ: magnetic tunnel junction

NM: non-magnet

OOMMF: object oriented micromagnetic framework

OOP: out of plane

QD: quantum dot

QDM: quantum dot molecule

QSL: quantum spin liquid

SD: spectral density

SHE: spin-Hall effect

SHO: spin-Hall oscillator

SOC: spin-orbit coupling

SOI: spin-orbit interaction

SOT: spin-orbit torque

STO: spin torque oscillator

STT: spin transfer torque

TI: topological insulator

TMR: tunneling magnetoresistance

Chapter 1: Introduction

The field of magnetism and spintronics addresses discussions on extended correlation among carrier spin polarization and orbital moments in different types of material systems. Subjects studied in magnetism and spintronics are divided into two main categories. One category comprises studies on metareial systems (e.g. magnetic metals, magnetic semiconductors, magnetic heterostructures, spin liquids, etc.) and their corresponding magnetic parameters (spin-spin correlation, chiral spin correlation, crystalline anisotropy, Lande g-factor, etc.). The other category consists of studies on the methods for the manipulation of local spins or extended magnetization.

Data retention in electronic devices has been pursued on different fronts. Among those are electric charge of floating gates in electrically erasable programmable read-only memory (EEPROM), crystallographic phase in phase change memory (PCM),[1] magnetization of magnetic structures in magnetic random access memory (MRAM) and hard disk drives, electric polarization in ferroelectric random access memory (FeRAM), resistance change due to voltage induced filament-forming in resistive random access memory (ReRAM),[2] and spatial position in nano-electromechanical memory.[3] In different applications, the memory concepts are evaluated based on different parameters such as data retention durability, cost, harsh environment tolerance, data write/read error and speed, energy consumption, and scalability. For example, hard disk drives have been the major choice for large-scale data storage for their relatively low cost, high storage capacity and moderate reliability.

Magnetization has been a major mainstream for data storage, including hard disk drives and magnetic random access memory technologies. In conjunction with magnetic data retention mechanisms and magnetic clocking, the extended waves of magnetization, spin waves, have been pursued to perform logic operations, enabling future all-magnetic computers to envision low energy consumption and scalability. In addition, in quantum computation, the spin degree of freedom is one of the forefronts of research.

In the following sections, a more detailed introduction will be provided on different methods for manipulation of spins in magnetic and spintronic devices. Specifically, the magnetic field, current, and optical manipulation of magnetization will be introduced. In addition, spin torque oscillators that can be synchronized in order to generate enough power for the magnetization switching are introduced. Finally, the concept of spin waves will be explained and the topics pursued in quantum magnetization are elucidated. This thesis is built upon the above bases, and aims to pave a way for future technological enhancement in magnetization manipulation.

1.1 Magnetic field-induced spin manipulation

A typical conservative (no damping) free energy landscape in an elliptic thin film magnetic dot with no crystalline anisotropy is demonstrated in Fig. 1-1(a). There are several ways to induce a trajectory of the magnetization vector that results in reversal of the magnetization or, in other words, to travel from a local minimum energy state to another state over the energy barrier (e.g. from

red cross to green cross in Fig. 1-1(a)). Applying an external magnetic field modifies the energy landscape, and the external magnetic field can be dc or microwave, or a combination of both. If the initial state of the magnetization (red cross in Fig. 1-1(a)) is unstable in the resulting landscape, the state of the magnetization changes, following a trajectory provided by the energy landscape. Figure 1-1(a) shows the process used for 'damping' switching, in which the energy landscape is modified with an external field (h_x in Fig. 1-1(b)) such that the energy well of the reversed state becomes deeper while the energy well of the initial state becomes shallower. If the thermal fluctuations are large enough to randomly locate the magnetization on the trajectory which surrounds both the energy wells, the magnetization equilibrates in the switched orientation due to the damping and the steeper energy well of the reversed state (the red trajectory in Fig. 1-1(b) is an example of such a reversal mechanism). Short pulses of the magnetic field can also be used to induce a landscape which places the initial and desired final states on a resonance trajectory (the purple curve in Fig. 1-1(c) is such a resonance trajectory).[4,5] The duration of the pulse is such that the magnetization state is in the desired final state and trapped in the energy well accommodating the reversed state over the inherent energy landscape.

Microwave-assisted magnetization switching is based on the absorption of microwave excitation by the magnetic resonance of a magnetic structure. The cone angle of the resonance grows and at some point it reaches the saddle point of the energy landscape, which surpassing it is an indicator of switching. The existence of the external magnetic field is required to modify the energy landscape in a way that the maximum cone angle of the resonance overlaps with the saddle point, and also the resonance in the switched energy well does not

have the same frequency as the excitation frequency at that cone angle, resulting in the magnetization staying at the switched energy well. By using microwave excitation, the dc magnetic field required for the reversal of a high magnetic anisotropy material or structure is reduced significantly. Microwave-assisted switching in single and multi-domain magnetic structures has been demonstrated experimentally.[6-13] The theory behind microwave-assisted switching has been assessed based on the instability of the resonance modes.[14-16] In addition, several numerical computations have been dedicated to study the effect of excitation and structural parameters in microwave-assisted switching, as well as the applicability of this method for future magnetic recording technologies.[15-20]

Spin-transfer torque oscillators (STO)[21-25] are the potential microwave irradiators to be implemented in the write heads of hard disk drives (further information for STOs is provided in Chapter 1.3). The frequency and power of the microwave oscillation in STOs is tunable by varying their driving dc currents and the bias fields. For the implementation of microwave-assisted switching, the excitation area should be decreased at the same rate by increasing the data storage density. Therefore, to achieve dots which store information as small as several nanometers, the write head should be able to irradiate microwaves focused down to the same area as the dot. Consequently, STOs with the dimensions of several nanometers are required, which is beyond the current fabrication capabilities, and also the power provided by such small STOs may not be sufficient for switching high magnetic anisotropy dots. Chapter 2 is dedicated to proposing a method for overcoming this obstacle in

magnetic recording technology, which can also be used for manipulation of magnonic crystals.

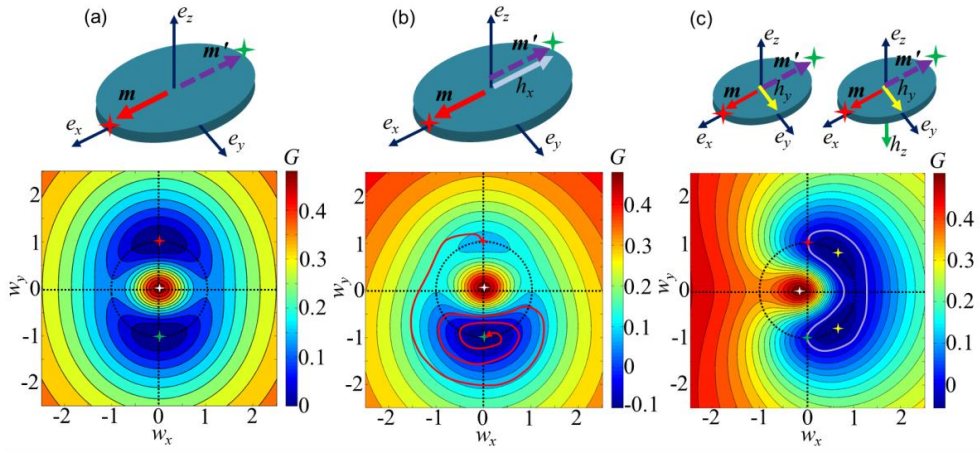

Figure 1-1. (a) The top panel is the schematic of a magnetic ellipse thin film, the respective Cartesian coordination, and the initial equilibrium magnetization direction. The bottom panel is the surface plot of free energy (G) landscape (G=0.5×($D_x m_x$+ $D_y m_y$+$D_z m_z$)-($h_x m_x$+ $h_y m_y$+$h_z m_z$), where $D_x(y,z)$, $m_x(y,z)$ and $h_x(y,z)$ are effective anisotropy coefficeient, magnetization and external field, respectively, in different coordinate axes) for a typical magnetic thin film ellipse with no external field and magnetized in the direction of its easy axis. The bottm panels are presented in the stereographic plane, where the coordinate transformation of $w_x = \frac{m_x}{1+m_z}$ and $w_y = \frac{m_y}{1+m_z}$ has been performed. (b) A typical energy landscape in the case of external field $h_x < 0$ (bottom panel), and the respective schematic (top panel). The red curve is a possible trajectory for 'damping' switching of the magnetization. (c) A typical energy landscape in the case of external field $h_y > 0$ (bottom panel), and the respective schematic of the fields needed for precessional switching (top panel). The purple curve is a possible trajectory for precessional switching of the magnetization. In (a-c), the red cross is the initial magnetization, the green cross is the desired switched magnetization, the white cross is the energy maxima, and the yellow crosses are the energy minima if they do not coincide with the initial and desired switched magnetization. In the schematics (top panels) of (a-c), ***m*** is the initial magnetization orientation and ***m'*** is the desired switched orientation. The colored crosses in schematics indicate the magnetization orientations corresponding to energy minimas in the energy landscapes.

Microwave excitation is not limited to the irradiation and can be conceived as modulation of currents which, in turn, can be used in magnetic

tunnel junctions (MTJ) or spin-orbit torque (SOT) devices for modification of switching (Chapter 3 utilizes microwave modulation of currents to address individual magnetization of nanodot matrices).

1.2 Current-induced spin manipulation

The essence of current-induced spin manipulation is exchange scattering of non-equilibrium spin that is non-collinear with respect to the local quantization axis of a magnetic system. The exchange scattering can be defined as a torque known as spin-transfer torque (STT). Such a torque can induce magnetization dynamics based on the space-time coordination of the non-equilibrium spin. The spin-transfer torque (STT) phenomenon has enabled magnetization auto-oscillations and reversal using spin-polarized currents in spin-valves, magnetic tunnel junctions (MTJ), and ferromagnetic/non-magnetic metal bi-layers or multi-layers[26-33].

Generally, there are two types of spin currents: one is the spin currents carried by charge currents, and the other is pure spin currents. The former is conceived in spin-valve or MTJ structures. Spin-valves are based on spatial separation of two magnetic metals (or half metals) by a non-magnetic metal, usually with a low atomic number (for low spin-orbit scattering). The charge current is spin polarized by the magnetic layers, and its spin polarization modifies the transmission and reflection of the charge current at the interfaces based on the relative coordination of the magnetization in the separated magnetic metals. The spin-polarization of the transmitted currents in the magnetic metals can induce STTs based on their polarization and the

magnetization coordination in the magnetic layers. The process of inducing non-collinear, non-equilibrium spins in MTJs is similar to the spin-valves, with the major distinction that the charge current is conceived by tunneling through a particular oxide such as Al_2O_3 or MgO. The tunneling magnetoresistance (TMR) can be 1-2 orders of magnitude larger than giant magnetoresistence (GMR) achieved in spin-valves. The switching in MTJs can be achieved with much lower currents than spin-valves.

Bulk and interface intrinsic and extrinsic spin-orbit interactions (SOI) have enabled the generation of pure spin currents, leading to spin-orbit spin-transfer torques in different structures such as multi-layers of ferromagnets and paramagnets, thin Rashba ferromagnets, impure ferromagnets and semi-conductors, structures with non-zero Berry curvature, etc.[34-49] Such spin currents and the torques exerted by them on the magnetization have been utilized in different configurations for switching or oscillation.[26,27,50-52] Intrinsic spin-Hall effect (SHE) (see Fig. 1-2(a-b)), skew scattering, side-jump scattering, and Rashba interaction are the main sources for the generation of pure spin currents. Diffusion of the generated spin current in the adjacent magnetic metal can induce a non-collinear, non-equilibrium spin accumulation with respect to the magnetization and causes STT, which, if large enough, can cause switching (this type of switching is termed spin-orbit torque (SOT) switching, to distinguish it from STT in spin-valves and MTJs).

The STT or SOT mechanisms used for switching or inducing oscillation in magnetic domains can be utilized for inducing dynamics in domain walls or generating domain walls (DW) such as skyrmion bubbles (see Fig. 1-3(a-b)).[53-

[58] The DW motion has been a subject of intensive study for different types of magnetic domains, as it can be utilized in the context of race-track memory.[59]

Another context of current-induced spin manipulation is by including the heat degree of freedom, which has given rise to the field of spin-caloritronics. Studies in this subject are usually divided into two categories.[60] One of them is the independent electron conduction thermal effect in metals, which is termed the spin-dependent Seebeck effect.[61] The other considers the collective effects from spin waves (in magnetic insulators such as Yttrium Iron garnet (YIG)) which are termed the spin Seebeck effect (e.g. magnonic spin Seebeck effect[62,63]). Heat induced spin-transfer torque, heat pumps and engines, and coherent excitation of spin waves are among the uses envisioned for devices utilizing correlation of electron, spin, and phonon dynamics.[64-66]

In addition to electric currents, voltage gating can be used as another method for the manipulation of spins. The electric field induced by the voltage gating can modify the magnetization dynamic parameters such as the gyromagnetic ratio in semiconductor quantum dots.[67,68] It can also be used to modify the chemical stoichiometry in the magnetic structures by inducing ionic motions, resulting in changes in SOI at the interfaces, changing the crystalline anisotropy of the magnetic material, or changing the relative moments of different sublattices in ferrimagnets and anti-ferromagnets. Figures 1-4(a-b) give an example of voltage tunability of interfacial magnetization.[69,70] Voltage gating can also be used to induce strain through the piezoelectric effect, causing strain-induced changes in magnetic crystalline anisotropy, which can be utilized to induce dynamics or even switch the magnetization.[71]

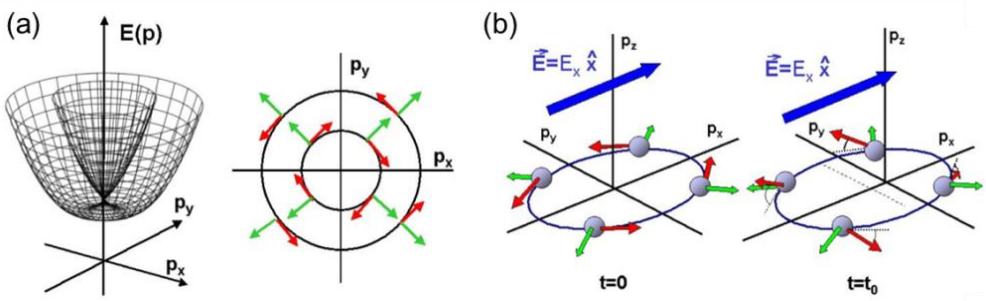

Figure 1-2. (a) Dispersion relation of eigenstates of the Rashba spin-orbit coupled system $H=\frac{p^2}{2m}-\frac{\lambda}{\hbar}\vec{\sigma}\cdot(\hat{z}\times\vec{p})$ where λ is the Rashba coupling constant (left panel), with exemplary momentum and respective spinor vectors in a particular energy cut. (b) Applying electric field in the x direction displaces the Fermi surface and due to the Rashba coupling and based on Bloch equation turns the spin up for $p_y > 0$ and down for $p_y < 0$, causing a pure spin current in the y direction, termed the intrinsic spin-Hall effect (SHE). Plots of (a-b) are adapted from ref. 43.

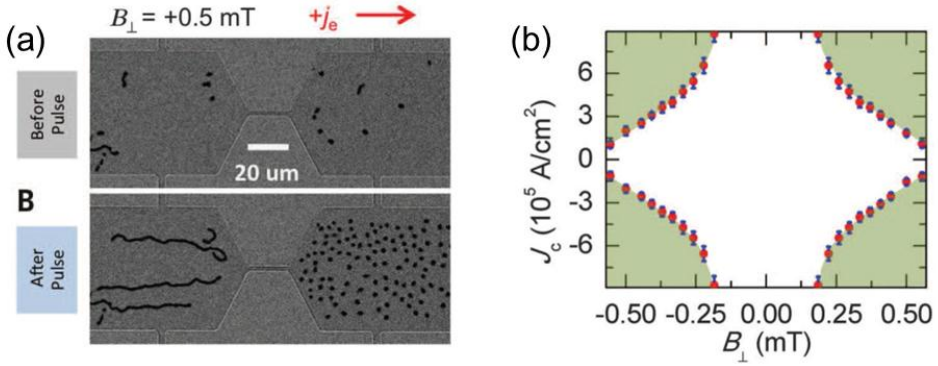

Figure 1-3. (a) When the current je is applied, the skyrmion bubbles are blown out of the nanowire from magnetic domains in one side of the structure into the other (here from left to right), based on the direction of the applied current and the perpendicular magnetic field. Skyrmions are topologically protected chiral magnetic domains that can be formed in magnetic structures with non-collinear magnetization raised by, for example, Dzyaloshinskii-Moriya interaction. (b) The phase diagram of skyrmion bubbles generation (shaded area indicates generation). Plots of (a-b) are adapted from ref. 53.

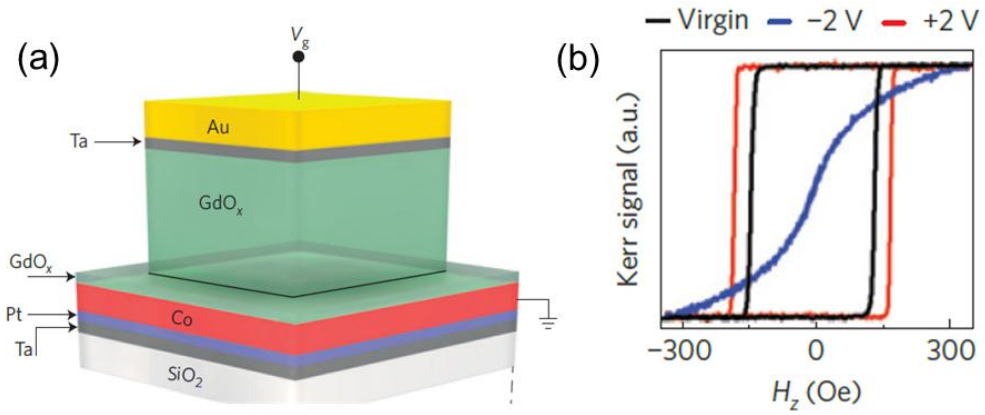

Figure 1-4. (a) Schematic of a device for ionic motion induced by gating to modify magnetization in the interface of Co and GdO_x. By tuning the gate voltage Vg, oxygen stoichiometry in the Co/GdO_x changes, leading to change in orbital hybridization in the interface which is responsible for the interface magnetization and anisotropy. (b) Change in the hysteresis loop with gating voltage. Plots of (a-b) are adapted from ref. 70.

1.3 Spin torque oscillators

Magnetic nano-oscillators have recently emerged from the spin-transfer torque (STT) phenomenon.[32,72-74] Based on the energy landscape, a particular amplitude and coordination of STT can lead to a precession which is stabilized by competition with Gilbert damping. Nano-contact or patterned spin-valves and magnetic tunnel junctions (MTJ) have been pursued for achieving spin torque oscillators (STO).[21,23,75,76] There have been some novel magnetic solitons like magnetic droplets and bullets that are being considered as STOs as well.[33,77]

A new type of oscillator based on the SHE has been introduced, in which the oscillation mode is a self-localized spin wave bullet,[24,51,78] and a recent experiment has demonstrated its injection locking (Fig. 1-5(a-b)).[79] The spin Hall oscillators (SHO) can also be realized in nano-magnetic elements as an auto oscillation mode.[50] Another method is to constrain the spin-wave spectrum

of the magnetic layer in a nanowire, so the SHE-induced oscillation remains coherent as it does not scatter with other possible spin-waves in the structure.[80]

Since the power and frequency bandwidth generated by a single nano-oscillator is not able to satisfy the requirements of its targeted applications such as a microwave emitter in hard disk drives or in communication devices, there have been many efforts undertaken in order to achieve a synchronization method of multiple oscillators.[75,81-86] In order to synchronize several STOs, a feedback system that can enforce the oscillations to lock and achieve the minimum free energy should exist. Kaka *et al.* demonstrated the first synchronization between two nano-STOs based on spin waves interactions (Fig. 1-6(a-b)),[75] in which the feedback system was mediated by spin waves. Injection locking is another approach in which an external alternating current is used to lock a group of STOs.[81,86-88] The injection locking has been an inspiration to pursue synchronization in MTJs or spin-valve STOs in series connection, where the stimulated current due to the oscillating magnetoresistance is utilized to form the feedback system and induce locking.[83,89] Four nano-contact vortex STOs have been experimentally synchronized, mediated by anti-vortices (Fig. 1-7(a-b)).[85] However, a relatively low frequency of vortex oscillators and high current required to induce vortex oscillations are the disadvantages of this method.

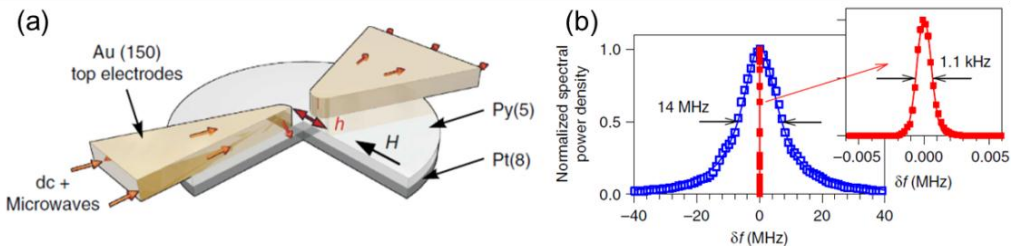

Figure 1-5. (a) Schematic of a spin-Hall oscillator. (b) Power spectral density (PSD) for the cases with (red curve) and without (blue curve) injection locking. Plots of (a-b) adapted from ref. 79.

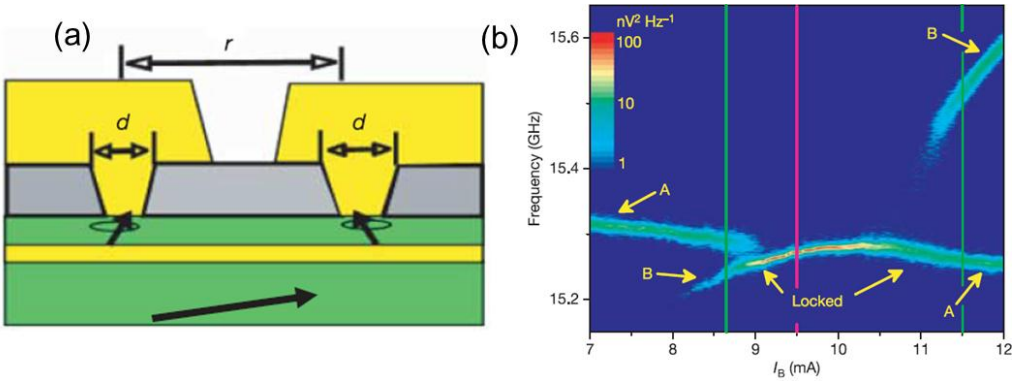

Figure 1-6. (a) Schematic of two neighboring nanocontact STOs which communicate through spin waves. (b) The synchronization of the oscillators in a particular current range. Plots of (a, b) adapted from ref. 75.

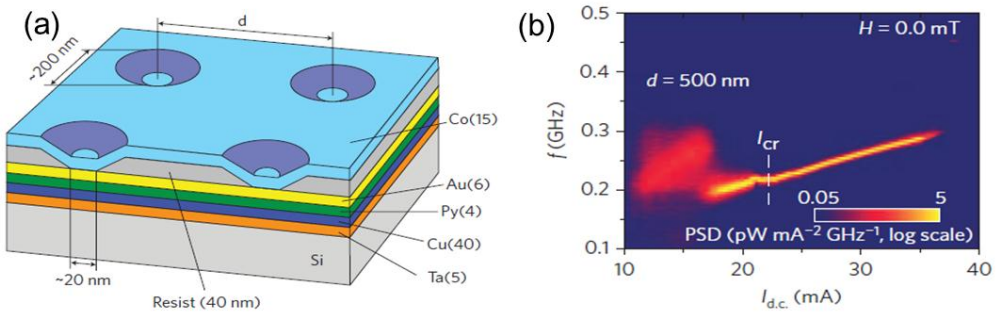

Figure 1-7. (a) Schematic of four nanocontact vortex oscillators. (b) The locking of the oscillators above a particular current. Plots of (a-b) adapted from ref. 85.

1.4 Optical manipulation of spin

Optical manipulation of spin has been intensively studied for different applications. Coherent coupling of light with spin dynamics can be explained through relativistic quantum electrodynamics, and the effect is pronounced as a reservoir of angular momentum in spin manipulation of structures such as antiferromagnetic NiO or solid-state defects.[90-93] However, the effect of light on the spin dynamics is applicable not only to coherent couplings, but also optical spin-transfer torque, modification of crystalline anisotropy, and demagnetization.[94-112] The origin of the demagnetization itself has been a subject of an ongoing debate in different structures.[97,98,100,103-107,109,113-117] The Elliot-Yafet mechanisms based on electron-phonon and electron-electron interactions, as well as magnonic dissipation and spin-dependent super-diffusive transport have been discussed to explain the ultra-fast demagnetization.

Incoherent all-optical manipulation of spin and magnetization reversal in ferrimagnets (Fig. 1-8(a-b)), anti-ferromagnets, and recently transition ferromagnets (Fig. 1-8(c-d)) has been demonstrated in several experiments.[109,118-123] A magnetic field induced by circularly polarized light due to the inverse optical Faraday effect, non-local transfer of angular momentum via spin currents, two-magnon scattering, demagnetization of different sites of the ferrimagnet (anti-ferromagnet), and exchange of the angular momentum between them due to different rates of magnetic moment change have been sought as the main contributors to all-optical switching (AOS) in such structures.[110,118,121,124-127] In addition, optical excitation has been proposed to excite particular modes of spin waves through the magnetoelastic effect.[128,129]

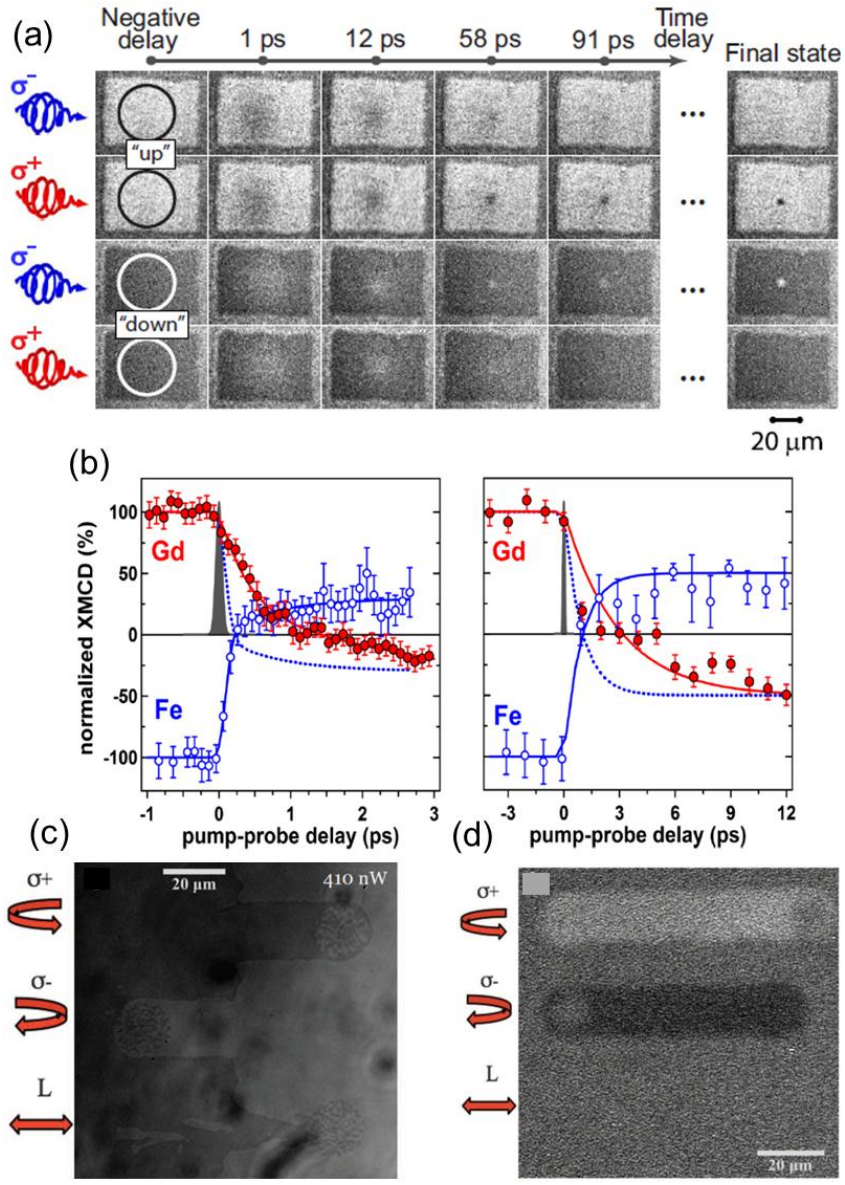

Figure 1-8. (a) Helicity dependent magnetization reversal in GdFeCo alloys using fs-laser pulses. Adapted from ref. 118. (b) Element-specific moment dynamics of Gd and Fe sites in GdFe alloys in fs-laser induced magnetization reversal. Adapted from ref. 130.[130] (c, d) Helicity dependent magnetization reversal in transition metal ferromagnets. Material in (c) is Co/Pt multilayer and material in (d) is FePtAgC granular media. (c, d) adapted from ref. 119.

The optical manipulation of spin is not only used for achieving magnetization reversal, but also provides a reliable method for the characterization of some parameters such as damping in magnetic structures, or in the Brillouin light scattering (BLS) experiments for characterizing the

dispersion relation of the magnetic systems, including the magnonic crystals.[131,132] Very recently, the ultrafast optical excitation has been used to induce THz emission from magnetic structures, which can be used to characterize different SOI mechanisms in magnetic/heavy metal heterostructures in addition to an alternative THz emitter.[133-136]

1.5 Spin waves

A very important type of wave that has been studied for decades is spin wave with a magnon as its quanta.[137] The feature that makes spin waves interesting for applications is their wave-vectors which are as small as a few nanometers and are in the frequencies of tens of GHz. As it is possible to engineer different dispersions in magnetic lattices, the magnonics has thereby attracted a lot of attention as a promising candidate with low energy consumption and high throughput computation, which may possibly go beyond photonic or even electron devices. There have been many theoretical and experimental demonstrations of different types of passive and active magnonic systems and crystals, such as transistors (Fig. 1-9(a-d)), interferometers, waveguides, and logic gates.[137-140] In addition, due to the high nonlinearity in magnetization dynamics, spin waves have become a base for studying different phenomena such as time reversal (Fig. 1-10(a-c)) and Bose condensation of magnons as Bosonic waves.[141,142] As mentioned in Chapter 1.3, spin waves can also be used as a feedback mechanism between STOs in order to synchronize them.[75]

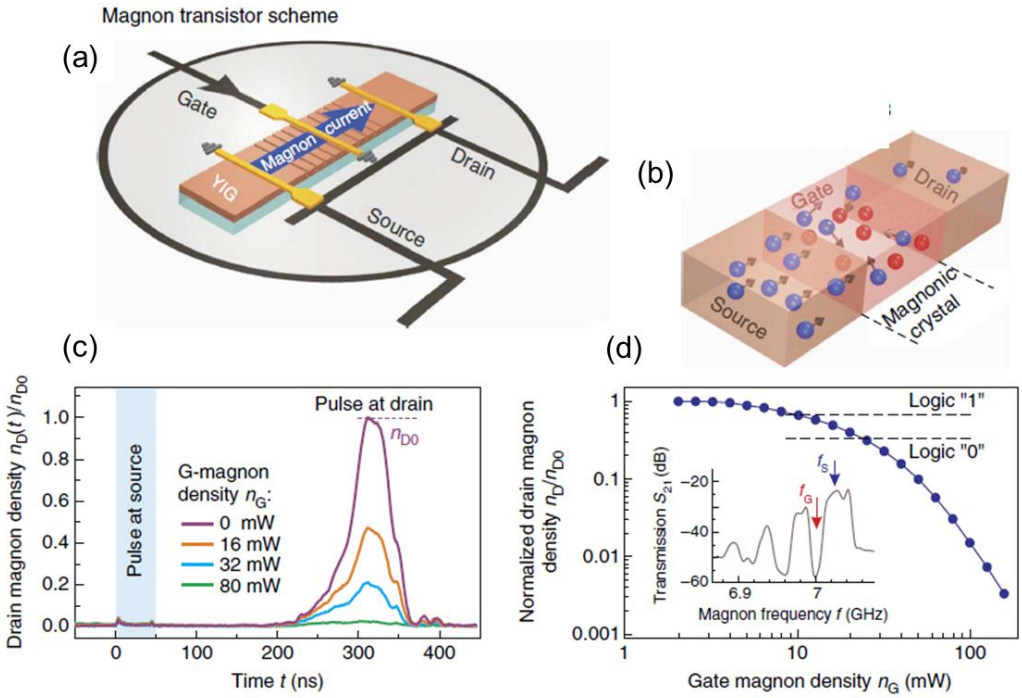

Figure 1-9. (a) Schematic of a magnon based transistor. (b) Schematic of scattering the magnons induced by source in the gate and not reaching the Drain. (c) Drain magnon density can be modulated by gate magnon density which is controlled by the gate excitation power. (d) Defining 0 and 1 of the logic based on drain magnon density which is a function of gate magnon density. Plots of (a-d) adapted from ref. 140.

The large arrays of magnetic dots (or nanowires) are the basis of magnonic crystals and the emerging bit patterned media for future recording technology.[143-145] Resonance behaviors of such densely packed magnetic structure arrays have been a subject of recent intensified research due to their applications in microwave technology or signal transfer.[146-153] Due to their switchable ground state from a ferromagnet to an antiferromagnet, magnetic dot lattices can be used as tunable magnonic crystals.[150,151] In addition, structural or magnetization non-uniformities in magnonic crystals lead to the appearance of defect modes, resulting in the modification of the spin-wave band-structure.[154,155] The nonlinearity of magnetization dynamics, the exchange and magnetostatic correlation in isolated dots, and the magnetostatic correlation

among the dots in the magnonic crystals provide a vast landscape of parameter space for dispersion relation control.

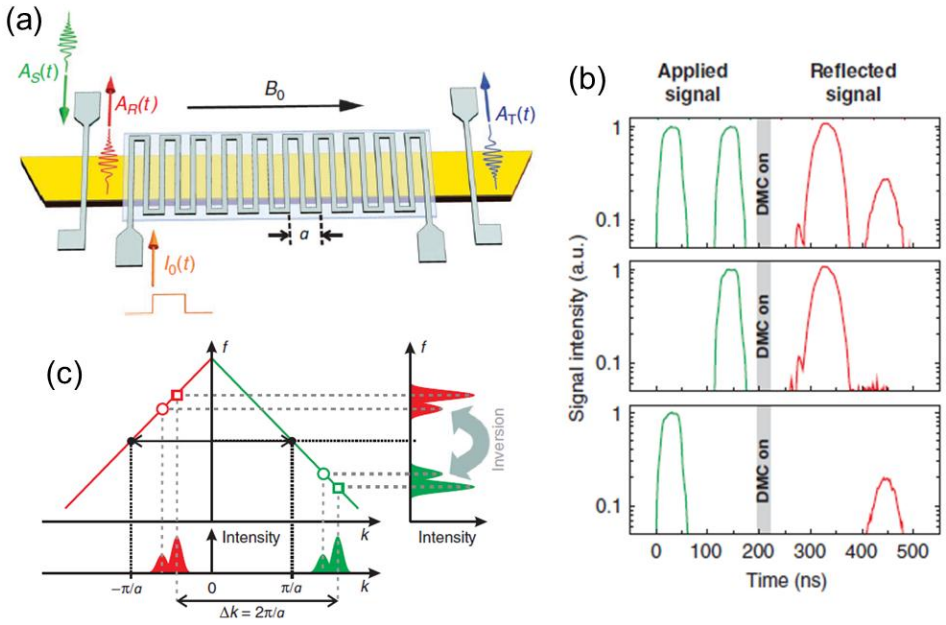

Figure 1-10. (a) Schematic of a magnonic crystal based device for linear time-reversal mechanism. (b) Schematic of the frequency inversion for the reflected spin waves in the magnonic crystal. (c) The applied and reflected signals when the magnonic crystal is on. The time reversal is evident. Plots of (a-c) adapted from ref. 141.

1.6 Quantum magnetization

In the mainstream quantum computation, quantum information is stored and processed in quantum states of a two-level or multi-level individual quantum dot or an ensemble of entangled quantum dots. There are several types of quantum bits (qubit) and the information to be stored in them; among those qubits are semiconductor quantum dots and superconducting Josephson junctions, and the bit quantum states in them are spin and charge, respectively.

There have been several approaches to control the states of individual qubits and qubit ensembles using electric dipole spin resonance, electric-gate tunneling control, optical control, g-tensor modulation (Fig. 1-11(a-c)) and combinations of them.[67,156-159] The spin (particle and orbital) states of excitons (charged or neutral) in semiconductor (e.g. GaInAs, InAs etc.) quantum dots are major candidates for quantum computing. There has been extensive research on this topic, among which anisotropies in the Lande g-factor, rich crossings and anti-crossings of ground and excitonic states by tuning electric and magnetic fields, exchange interactions of coupled qubits, effect of spin-orbit coupling, and hyperfine interaction have been investigated.[160-165] In addition, an entangled ensemble of quantum dots with a spin state forms a magnon which has been discussed in the context of quantum memory or gating mechanisms.[158,166,167]

In addition to using spins in QDs as quantum information, the hybrid quantum circuits using extended magnetic systems have become another forefront of quantum information science.[168] Recently, there has been demonstration of combining the studies on quantum-electro-dynamic coupling of magnons in the microwave cavities[169-171] and the studies on superconducting qubits, where a coherent coupling of the magnon mode of an extended magnetic system to the quantum state of a superconducting qubit has been achieved (Fig. 1-12(a-b)).[172-174]

Some structures such as triangular or kagome lattices can give rise to frustration for directions of the spin on the lattice sites, where the nearest neighbor or more extended exchange interactions do not allow a particular alignment to be achieved (see Fig. 1-13(a-b)).[175-178] In such structures, the quantum fluctuations keep the magnetization frustrated, and this frustration can

persist even at zero temperature. This phase is named quantum spin liquid (QSL) and is topological. QSLs can have fractional excitations which can be utilized for quantum computation.[179] It should be noted that such frustration is not limited to QSLs and it has been a subject of study for classical spins where it is named spin ice, and has been used to demonstrate magnetic monopoles.[177,180]

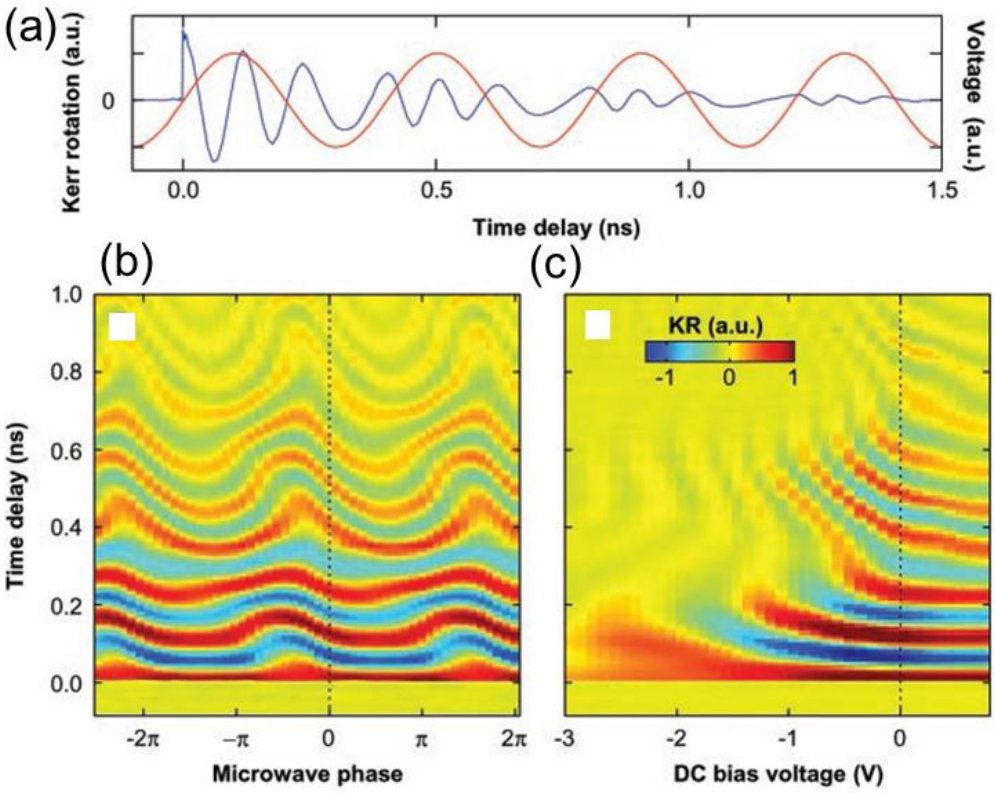

Figure 1-11. (a) The microwave excitation (red curve) and the time resolved Kerr rotation (TRKR) signal from the spin dynamics of a qubit (blue curve). (b) TRKR signal for different microwave phases when gate voltage is zero. (c) TRKR for the dotted line of (b) as a function of gate voltage. The modulation is an indicator of dynamics control by Lande g-tensor modulation. Plots of (a-c) adapted from ref. 67.

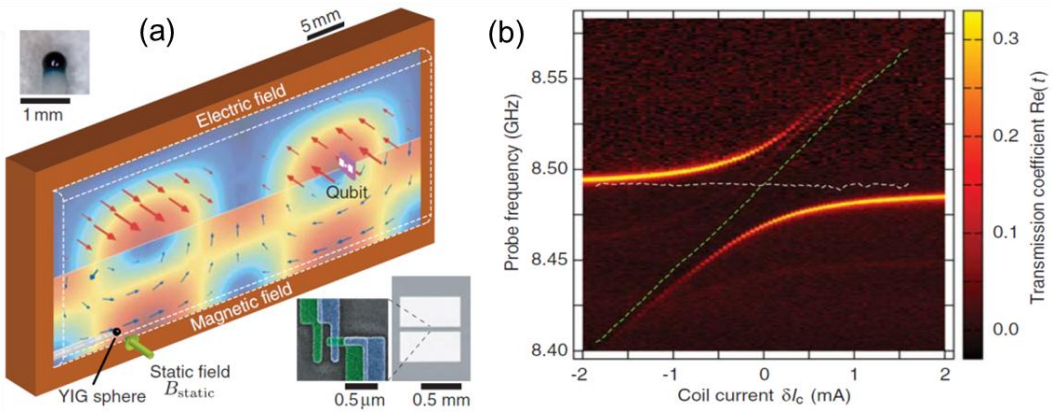

Figure 1-12. (a) Schematic of a superconducting Josephson junction qubit and a YIG sphere placed in a microwave cavity. (b) The anticrossing of the Kittel mode of the YIG sphere with a cavity mode. Plots of (a, b) adapted from ref. 174.

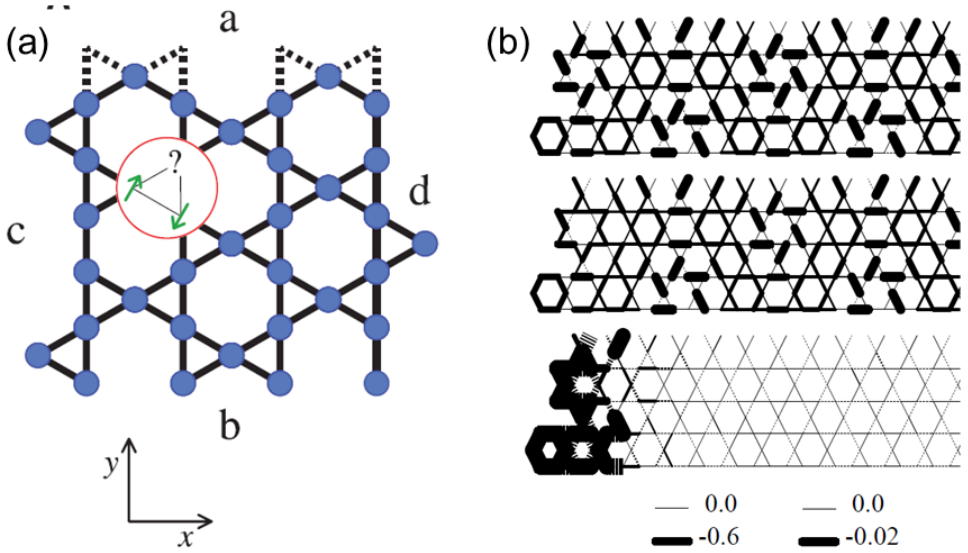

Figure 1-13. (a) Schematic of a kagome spin lattice, interacting by Heisenberg exchange. (b) Density matrix renormalization group (DMRG) numerical study of (A) shows that the preferred ground state is quantum spin liquid (QSL). Initially setting up a valence bond state (top panel), after DMRG sweeps with accepting more states results in the QSL in the bulk of the bottom panel (line types and thicknesses are indicators of bond spin-spin correlation). Plots of (a, b) adapted from ref. 176.

1.7 Summary and outlook of this thesis

As discussed above, the spin degree of freedom in different material structures can be used in several contexts for retaining, processing and communicating information, which form the core of condensed matter physics applications. Microwave, dc and pulsed magnetic fields, optical excitation, current, and gate voltage are direct and/or indirect strings of manipulation of the spin degree of freedom. The demand for higher data retention capacity, faster computation and reliable communication, while reducing energy consumption, has been growing for decades. When an existing method reaches its limits for getting better, scientists develop new methods to address similar needs but with more growing capabilities in order to satisfy the demands over a longer term.

In this thesis, some obstacles are addressed in the data retention mechanisms in magnetism and some methods are studied that can eventually be utilized for manipulation of spins in different contexts. Each of Chapters 2-6 contains a proposal for a novel mechanism, followed by theoretical and/or numerical proof of concept and analysis for the effects of important system parameters. It is worth noting, that in Chapters 4-6 and a major part of Chapter 2, the used numerical platforms were developed by myself, while the numerical results in Chapter 3 and a part of Chapter 2 are derived from a commercial solver.

In Chapter 2, a problem that is faced by write/read heads in hard disk drives (HDD) is addressed. As the storage capacity of the magnetic media will be enhanced by implementing bit-patterned media with very high magnetic crystalline anisotropy, the older HDD heads should be modified to implement

either heat-assisted or microwave-assisted magnetization reversal approaches. The challenge of addressing a magnetic dot with the size of a few nanometers has intrigued the proposal on utilizing the collective modes inherent to the magnetic nanodot matrices due to magnetostatic correlations. Chapter 2 describes how microwave excitation with a particular frequency and duration over a matrix of dots can be used to address the magnetic state of an individual dot. The method enables the use of current technologies of write/read heads for much higher data storage capacities. The same proposal can be utilized to control magnonic crystals by introducing particular defect patterns in order to achieve a particular dispersion relation.

Magnetic random access memories (MRAM) utilize STT or SOT switching, and are major candidates for future computational and/or data retention applications for their low energy consumption, fast response and high reliability. In current technologies, each magnetic bit should be accessed individually and has its own CMOS circuitry, including a few transistors. However, for ultra-high capacities, nanodots with the dimension of a few nanometers should be accessed. Chapter 3 describes a method to utilize the magnetostatic correlation among the nanodots in centrosymmetric matrices for accessing individual bits by common current excitation. This method paves the way to utilize current MRAM circuitry technology for much higher storage capacities.

In both Chapters 2 and 3, the magnetostatic correlation in the matrix of nanodots has been utilized to tackle the technological obstacle for accessing individual magnetic dots of a few nanometers in size. In both methods there is a need for microwave modulation, either as irradiation or as current modulation.

Specifically, the method proposed in Chapter 2 requires the microwave emitter to have tunable frequency in a long frequency range (from few hundreds of MHz to few tens of GHz) and to be of a few tens of nanometers in size, which is beyond the capability of microwave antennas. However, such characteristics can be achieved by using STOs (or SHOs) as microwave oscillators. To have sufficient high power and low bandwidth for microwave generation, there is a need to have a reliable way to synchronize an adequate number of STOs. Chapter 4 describes a method to synchronize STOs by using the capabilities provided by spin pumping, spin-Hall effect (SHE) and inverse spin-Hall effect (ISHE). This method enables many STOs to be synchronized in a configuration which is simpler for fabrication and implementation in applications.

All optical manipulation of the magnetization has become a major potential alternative for switching the magnetization in data storage devices. In Chapter 5, AOS in nanodots of magnetic transition metal/heavy metal bilayers is discussed. Through spin-dependent optically-excited (fs-laser excitation) diffusive transport in the presence of SOI mechanisms, specific conditions can lead to reversal of the magnetization in perpendicular anisotropy magnetic films. Such magnetization switching does not require any magnetic field, does not depend on polarization of the excitation laser, and can be achieved with a configuration of perpendicularly magnetized nanodots, the main candidate for data storage.

Chapter 6 focuses on the first step in a new dimension of magnetism – transformation magnonics. As transformation optics opens up new possibilities in photonics, transformation magnonics can introduce new approaches in magnonics. As customary for other types of waves, the first effort to establish a

transformation approach is to cloak a part of space to a propagating wave. In Chapter 6, the magnetic parameter tensors are derived which are needed to design a shell to cloak a cylindrical nonmagnetic core to a propagating spin wave. This chapter discusses how the required parameters can be achieved in magnetic systems such as magnetic oxides and ensemble of quantum dots. The transformation technique introduced in Chapter 6 can be used in future for concentrating spin waves, as it has been done for concentrating currents in Graphene and topological insulators (TI),[181,182] and light in photonic designs.[183,184] Concentrating spin-waves in spatial points can be utilized as another method for focused excitations, which in turn can be used as an alternative for inducing magnetization reversal in adjacent bits, with non-local excitation in larger dimensions than the targeted data bit.

Chapter 2: Magnetization reversal by excitation of collective modes

2.1 Introduction

The large arrays of magnetic dots are the basis of magnonic crystals and the emerging bit patterned media for future recording technology.[143-145] Resonance behaviors of such densely packed magnetic structure arrays have been a subject of recent intensified research due to their applications in microwave technology or signal transfer.[146-152] Due to their switchable ground state between a ferromagnet to antiferromagnet, magnetic dot lattices can be used as tunable magnonic crystals.[150,151] In addition, structural or magnetization non-uniformities in magnonic crystals lead to the appearance of defect modes, resulting in the modification of the spin-wave band-structure.[154,155] Magnonic crystals based on vortex arrays have been studied,[185-189] and it has been demonstrated experimentally that the state of a vortex matrix, where the diameter of each dot is 2 μm, is selectively formed under different frequencies of microwave excitation to achieve the lowest collective energy.[189]

Microwave-assisted magnetization switching is based on the absorption of microwave excitation by the magnetic resonance of a magnetic structure. The absorbed energy reduces the dc magnetic field required for reversal of a high magnetic anisotropy material or structure. Microwave-assisted switching in single and multi-domain magnetic structures has been demonstrated experimentally.[6-13] The theory behind microwave-assisted switching has been

assessed based on the instability of the resonance modes.[14-16] In addition, several numerical computations have been dedicated to study the effect of excitation and structural parameters in microwave-assisted switching, as well as the applicability of this method for future magnetic recording technology.[15-20] Spin-transfer torque oscillators (STO)[21-25] are the potential microwave irradiators to be implemented in the write heads. The frequency and power of microwave oscillation in STOs is tunable by varying their driving dc currents and the bias fields. For the implementation of microwave-assisted switching, the excitation area should be decreased at the same rate by increasing the data storage density. Therefore, for achieving data storage in dots as small as several nanometers, the write head should be able to irradiate a microwave field focused down to the same area as the dot. Consequently, STOs with the dimensions of several nanometers are required, which is beyond the current fabrication capabilities.

In order to fully utilize the functionalities of high density magnetic nanodots for magnonic crystals and future recording applications, a method for the selective reversal of a single nanodot in a matrix of dots is desired. For this purpose, a selective magnetization switching method with microwave excitation is proposed, which is based on dispersion in the power absorption of the collective magnetic resonance modes. Numerical simulations performed by object oriented micromagnetic framework (OOMMF) are used to support the idea. In addition, a theoretical model of the system is developed to have better insight on the physical interpretation of the phenomenon. The applicability of such a method for applications is also assessed.

2.2 Proposed method

Microwave excitation of a magnetic structure leads to magnetization dynamics which is a non-linear process. If absorption of the microwave power is more than Gilbert or spin wave damping, the magnetization cone angle grows from its initial stable condition while precessing. In a certain condition, the magnetization overcomes the energy barrier and falls into the other energy well. The magnetization dynamic process occurs by coupling the stored microwave power in the main precessional mode to the possible spin wave modes of the structure. A recent microwave assisted switching proposal is to excite a single dot with microwave in the presence of a dc field by considering the effect of the magnetizations of neighboring dots as sources of the stray field.[190] A magnetic dot array, which is interacting magneto-statically, exerts a dispersion relation based on the lattice, array, and the dot dimensions.[147,150] Therefore, absorption of microwave excitation with different frequencies leads to different spin wave modes of the dot array structure. This feature provides an opportunity to investigate the microwave-assisted switching process by exciting a matrix of magnetic dots (Fig. 2-1(a)). If a dc field is applied to a region of a dot array containing a N×N matrix of dots, there is a step change in the Zeeman energy of that region relative to the surrounding area. The N×N dot matrix has localized collective modes originated from the magneto-static interactions. Each of the 2^N possible oscillation modes in such matrix has a specific resonance frequency and absorption characteristic. An anomaly in the power absorption spectrum among the different oscillation modes causes nonuniformity in the oscillation amplitude among the dots. Therefore, it is expected that by exciting the dot

matrix by microwave fields with different frequencies, different oscillation amplitude patterns emerge, consequently resulting in reversal of the magnetization of dots into different patterns.

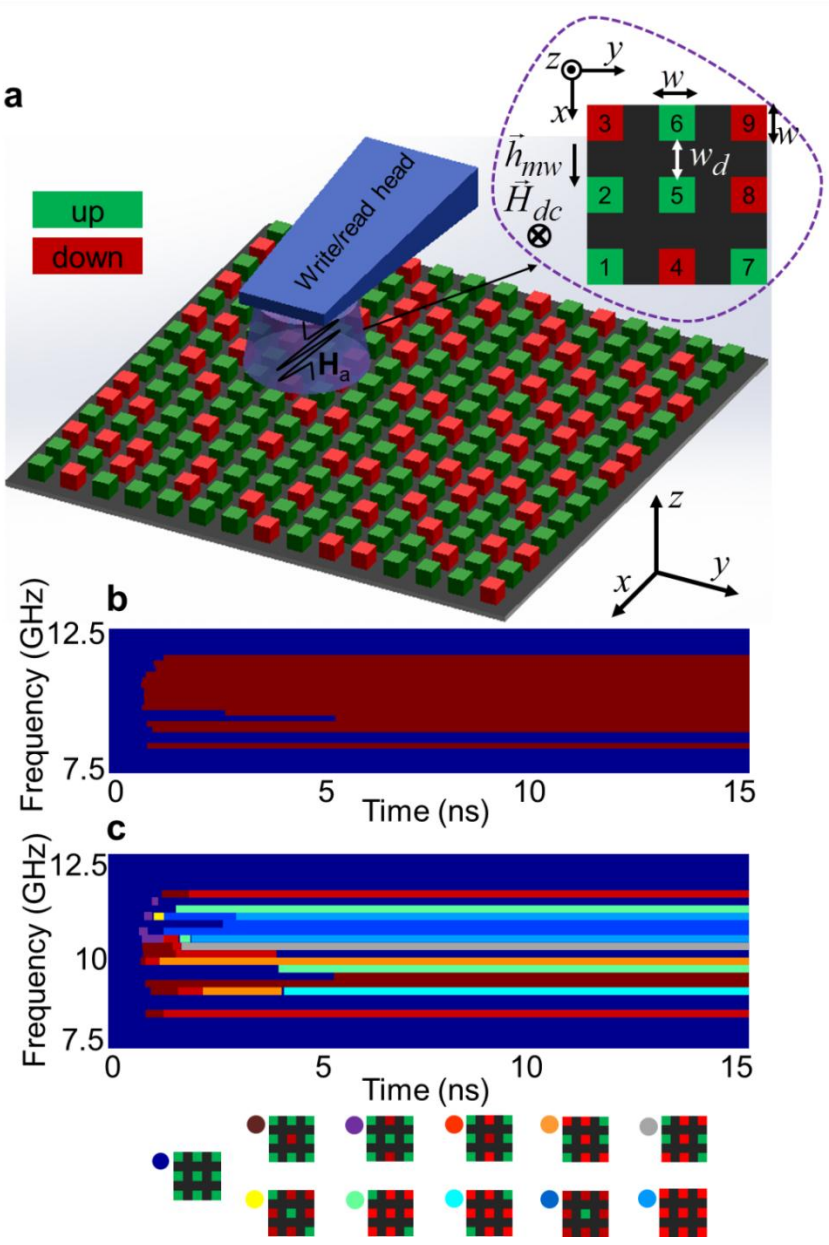

Figure 2-1. (a) The schematic of a dot matrix, the configuration of fields, and the excitation area. The dot number is defined for a 3×3 matrix. (b) Some of the realized reversal pattern for a 3×3 matrix of dots with respect to the excitation time and frequency, where H_{dc} = 14.5 kOe and h_{mw} = 400 Oe. (c) Each color stands for a magnetization pattern defined in the bottom of the graph.

2.3 Numerical analysis

In the following discussion, the results of the numerical simulations using OOMMF are presented. Figure 2-1(b) demonstrates the reversal occurrence of different patterns with respect to the microwave excitation frequency and duration for a 3×3 matrix of 10 nm×10 nm×10 nm dots. The inter-distance (w_d) between the dots in the x and y directions is 10 nm. The magnetic dots have uniaxial crystalline anisotropy in the z direction, and the anisotropy constant K_u is assumed to be 10^6 J/m^3 (in the order of $L1_0$-FePt which is a main candidate for perpendicularly magnetized media. This order of magnitude for K_u is adequate to guarantee room temperature thermal stability for the dot sizes used here).[191] The saturation magnetization M_s, the Gilbert damping constant α, and the gyromagnetic ratio γ, are set to 10^6 A/m, 0.005, and 2.2×10^5 m/(A·s), respectively. The dc field is $\vec{H}_{dc} = -H_{dc}\hat{z}$, where H_{dc} is 14.5 kOe (a field value that no reversal pattern is possible without microwave assist while the required microwave field amplitude is relatively small, 400 Oe). The microwave field is $\vec{h}_{mw}(t) = h_{mw} sin(\omega t)\hat{x}$, with h_{mw} equal to 400 Oe and $\omega = 2\pi f$. The initial magnetization direction for all the dots is assumed to be aligned to the z direction. The frequency f of the microwave field has been swept from 250 MHz to 12.5 GHz with a step of 250 MHz. For each of the f values, the magnetization switching pattern has been tracked up to 15 ns of excitation duration. Therefore the external magnetic field temporal profile contains a dc magnetic field $\vec{H}_{dc}$ applied in $0 < t < 15$ ns, superimposed by a microwave field $\vec{h}_{mw}(t)$ applied in $0 < t < T_{mw}$, where T_{mw} is swept from 0 to 15

ns. Overall, 26 different switching patterns are achieved with different excitation frequencies and durations with the above field values. All the emerging switching states are indicated in red color in Fig. 2-1(b). To make it clearer, the frequencies and durations required for achieving only 10 out of 26 possible switching patterns have been depicted and color-coded in Fig. 2-1(c).

Different initial states of the magnetization in dots result in different mode dispersions. Therefore, different switching patterns and sequences are expected for different initial states, depending on the excitation frequencies and durations. Figure 2-2(a) shows the switching behavior when two corners of the matrix are initially magnetized in the –*z* direction (marked in red). 18 different switching patterns are achieved for this initial state and four representative patterns have been depicted in Fig. 2-2(a).

In order to have better insight in the relation between the absorption of each dot in different frequencies and the corresponding switching state, squares of the magnetization (M_z^2) in the *z* direction of all the 9 dots have been plotted against the microwave excitation frequencies in Fig. 2-2(b) at 400 ps, which is well before the switching of any dot. It should be noted that 1- M_z^2 is proportional to the oscillation power; therefore, the higher (lower) M_z^2 is, the lower (higher) oscillation power and consequently oscillation amplitude is. In Figs. 2-2(b) and 2-2(d), the red color (high M_z^2 value) indicates there is no oscillation, while the blue color (low M_z^2 value) represents high oscillation amplitudes. As shown in Fig. 2-2(b), the oscillation amplitude is maximum (corresponding to the lowest M_z^2 value) in the central dot (dot number 5). It is observed in Fig. 2-2(a) that for the frequencies indicated by black arrows in Fig. 2-2(b), the switching of only the central dot occurs (marked in light blue). As an

example of the sequential emergence of different switching states, the reversal pattern sequence and the temporal evolution of M_z^2 at f = 10.75 GHz are depicted in Figs. 2-2(c) and (d), respectively. It can be seen in Fig. 2-2(b) that at f = 10.75 GHz, dot 5 has the maximum oscillation amplitude (low M_z^2 value), dots 3 and 7 have an intermediate oscillation amplitude, and the oscillation for dots 2 and 8 is the lowest. As shown in Figs. 2-2(c-d), the sequence of switching at this frequency occurs in this order (dot 5 → 3,7 → 2,8). It is worth noting that at this frequency, dots 4 and 6 equilibrate in a non-growing resonance mode (Fig. 2-2(d)). Figure 2-2(e) shows the pattern of the oscillation power (P_o = 1-M_z^2/M_s^2) for a relatively lower microwave field, h_{mw} = 50 Oe. The characteristics of oscillation patterns with frequency are similar to that in Fig. 2-2(b). The similarity confirms that the reversal patterns are initiated from the excited collective modes. An overall shift to higher frequencies of the patterns is due to a lower oscillation angle, and thus a higher anisotropy field. Figure 2-2(f) shows the phases of the oscillations in the dots with respect to the central dot (dot 5), at a particular time (t = 3 ns). A spatial variation of the phase (φ_o) confirms the existence of multiple collective modes at different frequencies.

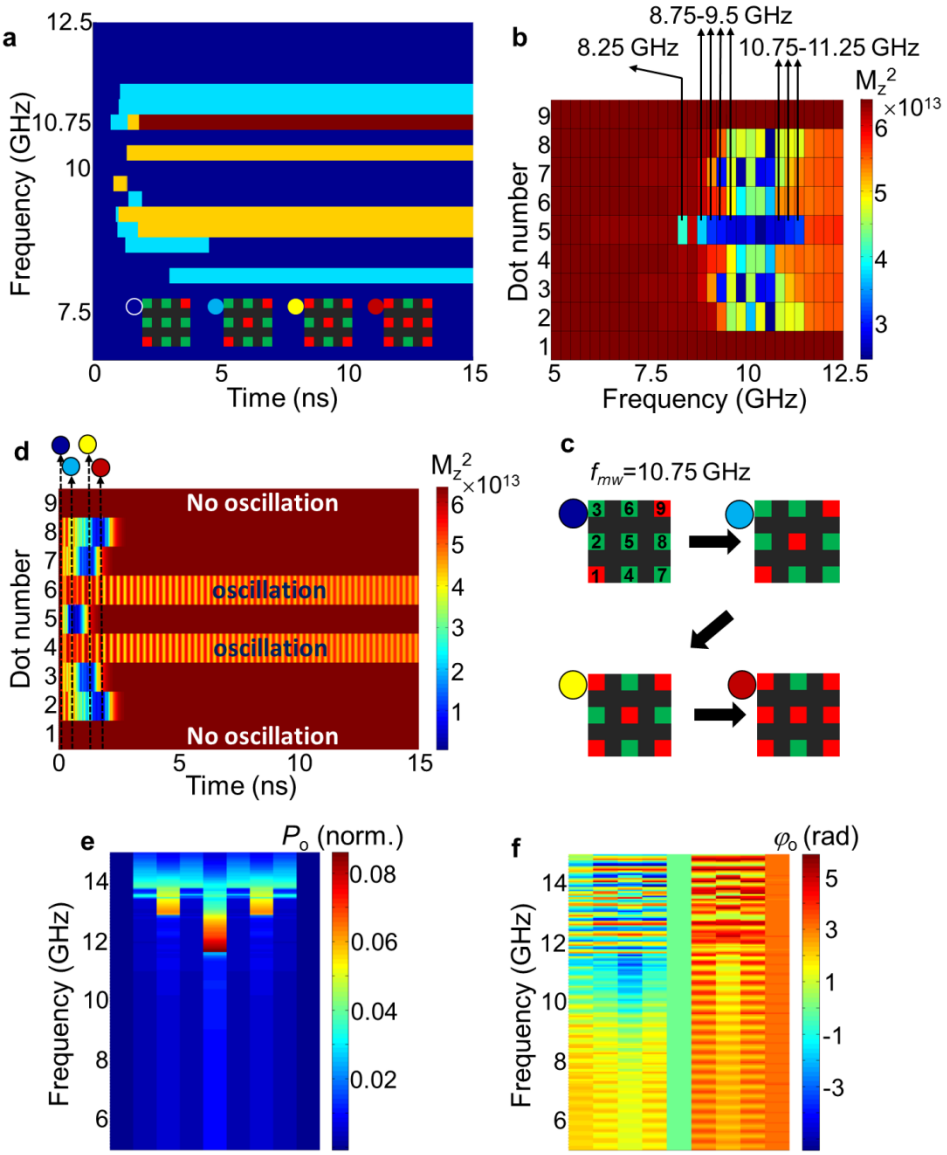

Figure 2-2. (a) Excitation time and frequency dependence for some of the realized reversal patterns, with two opposite corners initially magnetized to the $-z$ direction (marked in red). The magnetic configuration of each dot is defined in the graph. (b) M_z^2 of all the 9 dots versus frequency. Frequencies in which dot 5 has low values of M_z^2 are marked with the black arrows. (c) The reversal sequence for f = 10.75 GHz. (d) M_z^2 for all the dots at f = 10.75 GHz with respect to time. Colored circles stand for the patterns shown in (a) and (c). (e) The normalized oscillation power (P_o) at different frequencies and dots for h_{mw} = 50 Oe. (f) The oscillation phase of the dots with respect to that of dot 5 at t = 3 ns for h_{mw} = 50 Oe.

The amplitude of dc (H_{dc}) and microwave (h_{mw}) fields affect the switching behavior. The value of H_{dc} determines the frequency spectrum of the possible collective modes of the oscillations, whereas h_{mw} affects the change of the magnetization oscillation of each mode. The total effect is the summation of changes of all the possible modes. Figure 2-3(a) shows the total number of possible switching patterns (N_s) with various H_{dc} from the initial state of all dots tilted 12° from the *z* direction. For H_{dc} greater than a threshold value, N_s is close to 50. Figure 2-3(b) shows frequencies required for only reversing the central dot (dot 5) out of the matrix for different dc fields. A redshift with increasing H_{dc} up to 16 kOe is observed. This decrease in frequency is in conjunction with the relation of a single mode frequency and H_{dc}. For values of H_{dc} > 16 kOe, the competition among modes results in new values of frequency required for the reversal of only the central dot. N_s versus h_{mw} in Fig. 2-3(c) shows a peak at h_{mw} = 0.4 kOe, whereas the frequencies required for reversal of only the central dot do not show any strong features in Fig. 2-3(d), as the effect of h_{mw} on the collective reversal process is highly nonlinear.

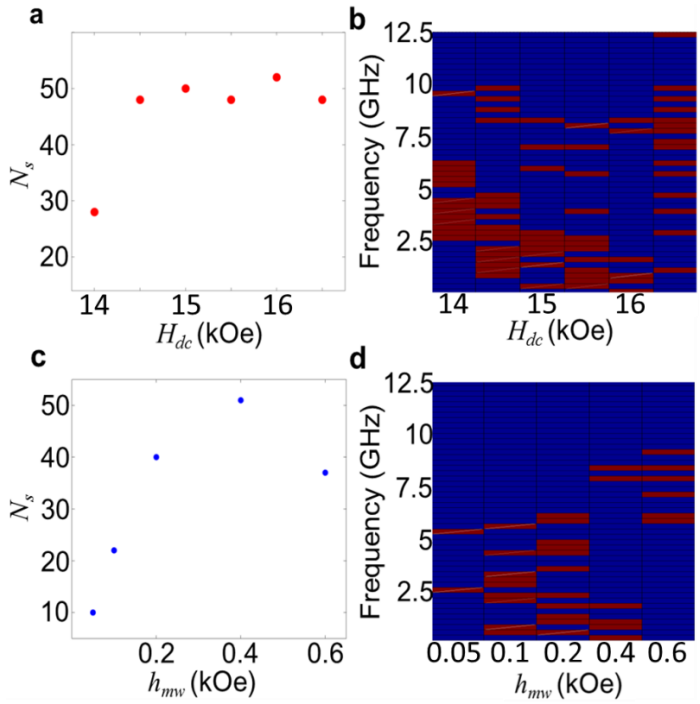

Figure 2-3. (a) The number of possible reversal patterns for different values of H_{dc}. (b) Frequencies of microwave excitations for achieving the reversal of only the central dot (dot 5) for various H_{dc}. (c) The number of possible reversal patterns for different values of h_{mw}. (d) Frequencies for achieving the reversal of only the central dot for various h_{mw}.

Despite the ability to achieve different switching patterns from a particular initial state, it is not possible to change the magnetization from an arbitrary initial pattern to any final pattern in one step of switching. As the maximum absorption is in the central dot, the focus is on the ability of reversing only dot 5 from different initial states of the matrix. The total number of initial states for a 3×3 matrix is 2^9, in which each dot can be aligned to the $-z$ or $+z$ direction. Since $\vec{h}_{mw}$ oscillates in the x direction, there are two mirror symmetry axes of (100) and (010). In consequence, there exists only 168 independent initial states. Excluding the initial patterns with dot 5 being down (−z direction), 84 states remain. Since there is no difference in applying the microwave field in

the x or y direction, only 51 initial states should be considered. Figure 2-4(a) shows the microwave excitation frequencies and durations in which the reversal of only dot 5 occurs. It is observed that for *all* the independent initial states, the reversal of sole dot 5 is possible. Although the focus is on the reversal of only the central dot, achieving different reversal patterns from different initial states is possible. Figure 2-4(b) shows the ratio of the realized reversal patterns (N_s) out of the possible patterns (N_p) depending on the initial states. It can be seen that for a limited number of initial states, we can achieve N_s/ N_p equal to unity. As expected, the initial states with strong symmetry result in small values of N_s/ N_p.

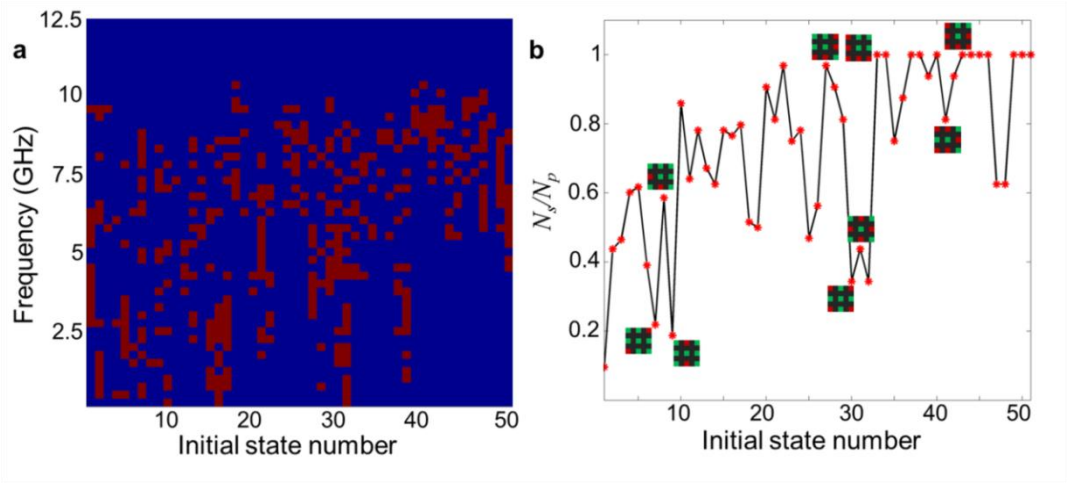

Figure 2-4. (a) The frequencies that the reversal of the central dot (dot 5) is possible for the 51 possible independent initial states. (b) The N_s/N_p for the 51 possible independent initial states. Some initial states are depicted beside their corresponding points. The applied fields are H_{dc} = 14 kOe and h_{mw} = 400 Oe.

The ability of reversal of only the center dot is not limited to 3×3 matrices of dots. Figure 2-5 shows some of the possible reversal patterns for a 7×7 matrix of dots from the initial state of all the dots being up. Among the

depicted reversal patterns, the frequencies in which the reversal of only the center dot occurs are depicted in dark red.

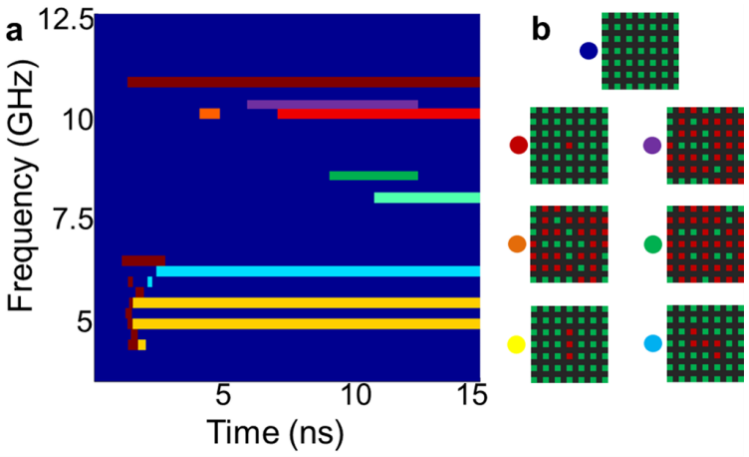

Figure 2-5. (a) Excitation time and frequency dependence for some of the realized reversal patterns for a 7×7 matrix of dots. The initial states are all the dots being magnetized to the z direction. (b) The states corresponding to each color are depicted. The applied fields are H_{dc} = 14.5 kOe and h_{mw} = 450 Oe.

2.4 Theoretical model

It is assumed that the N×N dot matrix under excitation is embedded in a very large array of dots. Each dot has the planar dimension of $w \times w$ and the thickness of h. The distance between dots in the x and y direction is w_d. The modeling approach presented here can be expanded to accommodate cylindrical or any other shape for the dots. A uniaxial crystalline anisotropy to the z-direction with the anisotropy constant of K_u is assumed. The magnetization of the dots is defined as

$$\left[\vec{M}\right]_{N\times N} = \left[\vec{M}_0\right]_{N\times N} + \left[\vec{m}(t)\right]_{N\times N}, \tag{2-1}$$

where $\left[\vec{M}_0\right]_{N\times N}$ is the matrix of initial magnetization states, and $\left[\vec{m}(t)\right]_{N\times N}$ is the matrix of dynamic magnetization as a function of time, *t*. For the chosen material, the initial magnetization matrix is

$$\left[\vec{M}_0\right]_{N\times N} = M_s\left[S\right]_{N\times N}\hat{z}, \tag{2-2}$$

where $\left[S\right]_{N\times N}$ is 1 or -1. The oscillation of each mode can be described by their complex time varying amplitudes $\vec{C}_i(t)$ as

$$\left[\vec{K}_i\right]_{N\times N} = \vec{C}_i(t)\left[K_i\right]_{N\times N}, \tag{2-3}$$

where $\left[K_i\right]_{N\times N}$ is a binary permutation of the N×N matrix elements (dots), and *i* is from 1 to N_m. Depending on the initial state, N_m can be different from 1 to 2^N. Therefore, the total magnetization dynamic matrix is $\left[\vec{m}(t)\right]_{N\times N} = \sum_{i=1}^{N_m}\left[\vec{C}_i(t)\left[K_i\right]_{N\times N} + c.c.\right]$, where c. c. denotes the complex conjugate.

For analyzing the dynamics of each mode, the Landau-Lifshitz-Gilbert (LLG) equation is used

$$\frac{d\vec{C}_i(t)}{dt} = \gamma\left(\vec{H}_{eff,i}\times\vec{C}_i(t)\right) - \frac{\alpha\gamma}{M_s}\left(\left(\vec{H}_{eff,i}\times\vec{C}_i(t)\right)\times\vec{C}_i(t)\right), \tag{2-4}$$

where $\vec{H}_{eff,i}$ is the effective field for each mode and can be written as

$$\vec{H}_{eff,i} = \vec{H}_{dc,eff} + \vec{h}_{mw} + \vec{H}_{d,i} + \vec{H}_A. \tag{2-5}$$

$\vec{H}_{dc,eff} = \vec{H}_{dc} + \vec{H}_{OB}$, $\vec{H}_{OB}$ is the magneto-static field from the dots outside the *N*×*N* matrix, $\vec{H}_A = \frac{2K_u}{\mu_0 M_s{}^2}\left(\vec{C}_i(t)\cdot\hat{z}\right)\hat{z}$ is the crystalline anisotropy

field, and $\vec{H}_{d,i}$ is the demagnetizing field for the mode *i*, which can be written as

$$\vec{H}_{d,i} = -\sum_{p,q}\sum_{m,n} \hat{N}\left(\vec{r}_{pq} - \vec{r}_{mn}\right)\cdot \vec{M}_{0,pq}\ , \tag{2-6}$$

where $\hat{N}\left(\vec{r}_{pq} - \vec{r}_{mn}\right)$ is the demagnetizing tensor, $\vec{r}_{pq}\,(\vec{r}_{mn})$ is the center of the dot in the row *p* (m) and the column *q* (n). The first summation runs over *m* and *n* from 1 to *N*, while *p* and *q* run over only the elements that are included in the mode *i*; in other words for each $m,n \in 1,2,...,N$ such that $K_{i,mn} = 1$. To calculate the demagnetizing tensor, we can use[192]

$$\hat{N}\left(\vec{r}\right) = D\left(\vec{r}\right) \otimes \Lambda\left(\vec{r}\right), \tag{2-7}$$

where $D\left(\vec{r}\right)$ is the shape function of the dot, and $\Lambda\left(\vec{r}\right)$ is the demagnetizing tensor for a dipole $D\left(\vec{r}\right) = \delta\left(\vec{r}\right)$ which can be written as

$$\Lambda\left(\vec{r}\right) = \frac{1}{4\pi r^5}\begin{bmatrix} r^2 - 3x^2 & -3xy & -3xz \\ -3xy & r^2 - 3y^2 & -3yz \\ -3xz & -3yz & r^2 - 3z^2 \end{bmatrix}. \tag{2-8}$$

The resonance frequency of each mode can be derived from Eq. (2-4) by neglecting the Gilbert damping and assuming h_{mw} = 0. By assuming $\vec{C}_i\left(t\right) = \vec{c}_i\left(t\right)e^{j\omega_i t}$, we can write

$$\omega_i = \gamma\left(\left(\left(N_{z,i} - N_{y,i}\right)M_s - \left|\vec{H}_A\right| + H_{dc}\right)\left(\left(N_{z,i} - N_{x,i}\right)M_s - \left|\vec{H}_A\right| + H_{dc}\right)\right)^{1/2}$$

, (2-9)

where $N_{x,i}$ ($N_{y,i}$ and $N_{z,i}$) is the first (second and third) element of $\sum_{p,q}\sum_{m,n} \hat{N}\left(\vec{r}_{pq} - \vec{r}_{mn}\right)\cdot\left[1 \quad 1 \quad 1\right]/\sqrt{3}$ for the mode *i*.

Exciting the matrix of dots with microwave results in an absorption of power by possible modes, in which the resonance frequency (ω_i) is different for the various modes. Assuming $\vec{h}_{mw} = h_{mw} e^{-j\omega_{mw} t} \hat{x}$, Eq. (2-4) results in the steady susceptibility tensor $\hat{\chi}(\omega)$,

$$\hat{\chi}(\omega) = \gamma M_s \begin{bmatrix} j(\omega_i - \omega_{mw}) & \gamma\left(\left(N_z - N_y\right)M_s - \left|\vec{H}_A\right| + H_{dc}\right) - \alpha j(\omega_i - \omega_{mw}) \\ \gamma\left(\left(N_x - N_z\right)M_s + \left|\vec{H}_A\right| - H_{dc}\right) + \alpha j(\omega_i - \omega_{mw}) & j(\omega_i - \omega_{mw}) \end{bmatrix}^{-1},$$

(2-10)

Therefore, we can write the stationary values of $\vec{c}_i$ as $\begin{bmatrix} c_{i,x} \\ c_{i,y} \end{bmatrix} = \hat{\chi}(\omega) \begin{bmatrix} h_{mw,y} \\ h_{mw,x} \end{bmatrix}$. Finally, the total stationary value of dynamic as $\left[\vec{c}_T\right]_{N\times N\times 2} = \sum_{i=1}^{N_m} \vec{c}_i \left[K_i\right]_{N\times N}$ is defined. Even though $\left[\left|\vec{c}_T\right|\right]_{N\times N}$ does not infer any information about the growth of the magnetization dynamics, it is a good measure which indicates the relative oscillation amplitude among the dots of the matrix, where the possible reversal is expected to be initiated from the dots with the largest absorption (Fig. 2-2).

As discussed before, the independent initial states of the magnetization ($\left[\vec{M}_0\right]_{N\times N}$) that should be considered are fewer than the total possible states of 2^N, due to the symmetries induced by $\vec{H}_{dc}$ (infinite mirror planes in the *xy* plane) and $\vec{h}_{mw}$ (mirror axes along (1 0 0) and (0 1 0)). In addition, if $\vec{h}_{mw}$ is linearly polarized along the *x* or y axis, or circularly polarized, some states can be assumed as degenerate and only one of them is analyzed. As mentioned before, for the case of *N* = 3, there are 51 independent initial states where the

central dot is magnetized to the z direction. Using the above analytical method, $\left[|\vec{c}_T|\right]_{3\times3}$ is calculated for all the independent initial states ($\left[\vec{M}_0\right]_{3\times3}$), and extract the frequencies in which the central dot has the highest oscillation amplitude ($|\vec{c}_T|_{2,2} \geq |\vec{c}_T|_{m,n}\ \forall m,n \in 1,2,3$). Figure 2-6(a) shows that there are several frequencies for most of the independent $\left[\vec{M}_0\right]_{3\times3}$ with a combination of $\left|\vec{H}_{dc,eff}\right|$, in which the absorption of the central dot is maximum. If the central dot has the highest absorption amplitude for a particular frequency, it indicates the possibility of the sole reversal of the central dot with the growth of the collective modes. However, dynamic consideration of the collective modes can modify the reversal process as discussed below. The microwave excitation is coupled to the collective oscillation modes and results in their growth and consequently, reversal of the magnetization of the dots. To derive the temporal behavior of each of the collective modes,[151] the circularly polarized basis is used for each of the modes where $\vec{C}_i(t) = \vec{m}_i c_i^{'}(t)$ and $\vec{m}_i = (-i,1,0)$ can be written. Since the coordination basis is unique for each of the modes, scattering between the modes is prohibited. Due to the assumption of small oscillations, H_A becomes constant and can be included in H_{dc} . After some algebraic simplification and keeping only the linear terms in $c_i^{'}(t)$, we can write

$$\frac{dc_i^{'}}{dt} = -i\Omega_i c_i^{'} - iR_i c_i^{'*} - \Gamma_i c_i^{'} + \xi_i(t) \tag{2-11}$$

where

$$\Omega_i = \gamma\mu_0 H_{dc} - \gamma\mu_0 H_{d,i}^z - \gamma\mu_0 \left(\frac{H_{d,i}^x + H_{d,i}^y}{2} \right)$$

$$R_i = -\gamma\mu_0 (1 + i\alpha) \left(\frac{H_{d,i}^y - H_{d,i}^x}{2} \right) \tag{2-12}$$

$\Gamma_i = \alpha\Omega_i$.

The term, $\xi_i(t)$ containing the coupling of the microwave excitation to the oscillation mode *i* can be written as

$$\xi_i(t) = i\gamma\mu_0 M_s \left(\vec{m}_i \cdot \vec{h}_{mw} \right). \tag{2-13}$$

In the circularly polarized basis for the mode *i*, the linearly polarized $\vec{h}_{mw}$ along the *x* direction is equal to $\left(h_{mw} e^{j(\omega_{mw} - \omega_i)t}, 0, 0 \right)$. By writing the same equation as Eq. (2-11) for c_i^* and some algebraic simplifications, the second order non-homogenous differential equation for c_i is

$$\frac{d^2 c_i'}{dt^2} - 2\Gamma_i \frac{dc_i'}{dt} + \lambda_i c_i' = f_i(t) \tag{2-14}$$

where $\lambda = \Omega_i^2 + |R_i|^2 + \Gamma_i^2$, and $f_i(t) = -i\Omega_i \xi_i + \Gamma_i \xi_i - iR_i \xi_i^* + \frac{d\xi_i}{dt}$. The solution to this differential equation is

$$c_i'(t) = \frac{\mu_0 M_s h_{mw}}{\upsilon_2 - \upsilon_1} \left[e^{\upsilon_1 t} \left(\frac{D}{j(\omega_{mw} - \omega_i) - \upsilon_1} - \frac{\gamma}{-j(\omega_{mw} - \omega_i) - \upsilon_1} \right) + e^{\upsilon_2 t} \left(\frac{-D}{j(\omega_{mw} - \omega_i) - \upsilon_2} + \frac{\gamma}{-j(\omega_{mw} - \omega_i) - \upsilon_2} \right) \right] \tag{2-15}$$

where $\upsilon_1 = \frac{1}{2}\left(2\Gamma_i + \sqrt{4\Gamma_i^2 - 4\lambda_i} \right)$, $\upsilon_2 = \frac{1}{2}\left(2\Gamma_i - \sqrt{4\Gamma_i^2 - 4\lambda_i} \right)$, and $D = \gamma\left(i\Omega_i - \Gamma_i + iR_i \right)$.

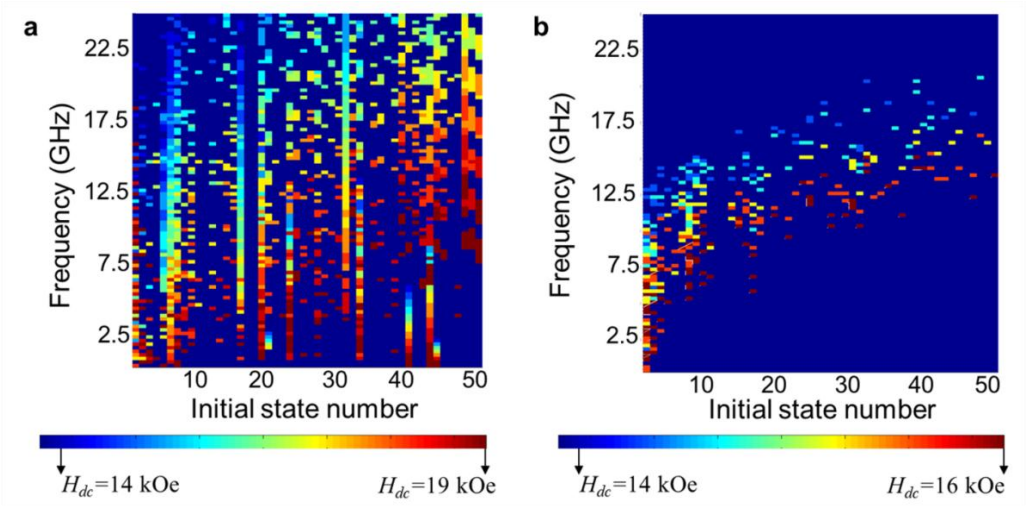

Figure 2-6. (a) The frequencies in which the stationary oscillation amplitude of the center dot (dot 5) is larger than the other dots for the 51 possible independent initial states. The graph includes results for H_{dc} from 14–19 kOe with a step of 0.5 kOe. (b) The frequencies in which only the center dot (dot 5) reverses in less than 30 ns for the 51 possible independent initial states. The graph includes results for H_{dc} from 14–16 kOe with a step of 0.5 kOe. In (a) and (b), the colors other than background dark blue, refer to H_{dc} values.

The total oscillation amplitude of each of the dots at each moment is the summation of all the oscillation modes containing that dot, $\left[c_T^{'}(t)\right]_{N\times N}=\sum_{i=1}^{N_m}c_i^{'}(t)\left[K_i\right]_{N\times N}$. The reversal for the dot at the row *m* and the column *n*, at the time moment of τ can be deterministic if $\left|Re\left[c_{T,mn}^{'}(\tau)\right]\right|\geq 1$. Figure 2-6(b) demonstrates the analytical results for the possible frequencies for the reversal of only the central dot for all the initial states and different values of H_{dc}, in the cases that the reversal occurs less than 30 ns, where h_{mw} = 400 Oe and N = 3. Figure 2-6(b) can be thought of as the counterpart of Fig. 2-4(a). The discrepancies between the analytical results and the numerical simulation results are due to the fact that for the sense of simplicity, $H_{d,i}^{x}$, $H_{d,i}^{y}$ and $H_{d,i}^{z}$ are

assumed to be constant during the dynamics, while in reality these components change with the growth of the amplitude of the oscillation modes.

2.5 Discussion

As mentioned earlier, the Zeeman energy due to the localized dc and microwave fields in the excitation area forms an energy well that rules out the possibility of reversal in the outer dots. Due to zero H_{dc} in the surrounding dots, their resonance frequencies of outer dots are very different from those of the dots inside the excited area; therefore, energy transmission from the inside to outside dots is negligible. However, the effect of surrounding dots outside the excitation area on the reversal process of the targeted dot cannot be ignored, since they act as sources of stray fields. A non-uniform stray field from the outer dots causes change in the reversal spectrum. The stray field generated by the surrounding dots in the targeted dots matrix has a spatial pattern which depends on the magnetization status of the surrounding dots. We can write this stray field in the targeted matrix as $\left[H_s\right]_{N\times N} = \sum_{i=1}^{N_m} a_i \left[K_i\right]_{N\times N}$, where N_m is the number of possible modes for a particular initial state of an N×N matrix. Therefore by extracting a_i for a given $\left[H_s\right]_{N\times N}$, and knowing the effect of the value of a_i on the reversal spectrum, H_{dc}, the excitation microwave frequency (ω_{mw}), and the microwave amplitude (h_{mw}) can be adjusted to achieve the targeted reversal.

Another issue is the robustness against the initial magnetization direction and dispersion in the anisotropy field. As the microwave field is

assumed to be applied in the *x* direction, the transfer of energy from microwaves to the dynamic modes depends on the azimuthal angle (φ_{init}) of the initial magnetization of the dots, and it can alter the excitation frequencies and the time required for the reversal of the central dot, as shown in Fig. 2-7(a), with a fixed polar angle (θ_{init}) of 2° from the +z direction. Despite wide variations of φ_{init}, the change of switching frequencies and the required excitation time is moderate. Figure 2-7(b) shows the effect of ±11° variations around φ_{init} = 45° for two different cases of θ_{init} = 4.5° and 5.5°. The excitation frequency and time required for the reversal of the central dot are relatively robust for slight variation of the initial magnetization direction around a predefined value (φ_{init} = 45°). In practice, there could be a mechanism to set such an initial condition by applying a local or global dc field or by tilting the anisotropy direction during the material growth or annealing, preceding the microwave excitation.

Thermal agitation can perturb the anisotropy field. Figure 2-7(c) shows the effect of different levels of perturbation in the crystalline anisotropy constant, $K_u = 10^6$ J/m^3. The effect is negligible at several frequencies for ΔK_u up to the order of 10^4 J/m^3. A spatial distribution of the anisotropy field considering both a symmetric and an asymmetric case in the matrix was also studied. Figure 2-7(d) shows that even up to 10% of dispersion in K_u, there are several common frequencies to be utilized for switching. Thermal noise can be described as a Gaussian random variable in both time and space with a strength of $\sigma^2 = 2\alpha kT / \gamma M_s V$, where k is the Boltzmann constant, T is the temperature, and V is the volume of the magnetic element.[5] At T = 300 K and for the assumed material parameters, σ / μ_0 = 10.9 Oe, which is negligible in

comparison to the values of h_{mw}, H_{dc} and H_A. The robustness shown in Fig. 2-7(b-d) indicates that the reversal is initiated through stable precessional modes, therefore the above thermal noise is negligible.

The proposed method of selective reversal needs to be carried out by sensing the initial magnetization state of all the dots in the N×N matrix. The sensing can be done collectively. In addition, the total stray field from the outer dots needs to be measured by additional sensors, for example, using a 3×3 sensor matrix. Based on the initial pattern of the inner dots and the stray field from the outer dots, the proper microwave excitation (frequency, duration, and amplitude) as well as a dc field should be applied. The characteristics of proper microwave excitation should be preset for all the possible independent initial states and the stray field patterns from the outer dots, as what is done for a 3×3 isolated matrix in Fig. 2-4(a). After a reversal of the central dot in the N×N matrix, the write/read head should move as such an excitation area is shifted by $w + w_d$ (Fig. 2-1(a)). Afterwards, the reversal of the central dot of the new N×N matrix can be carried out. Alternatively, microwave striplines can be utilized for introducing defects in a magnonic crystal consisting of a perpendicularly magnetized dot array. Each of the striplines can cover a matrix of dots. As the ground state of the array is known, the reversal of the central dot of each matrix can be carried out by applying a microwave current with a suitable frequency, duration, and amplitude to the striplines with a sufficient dc magnetic field.

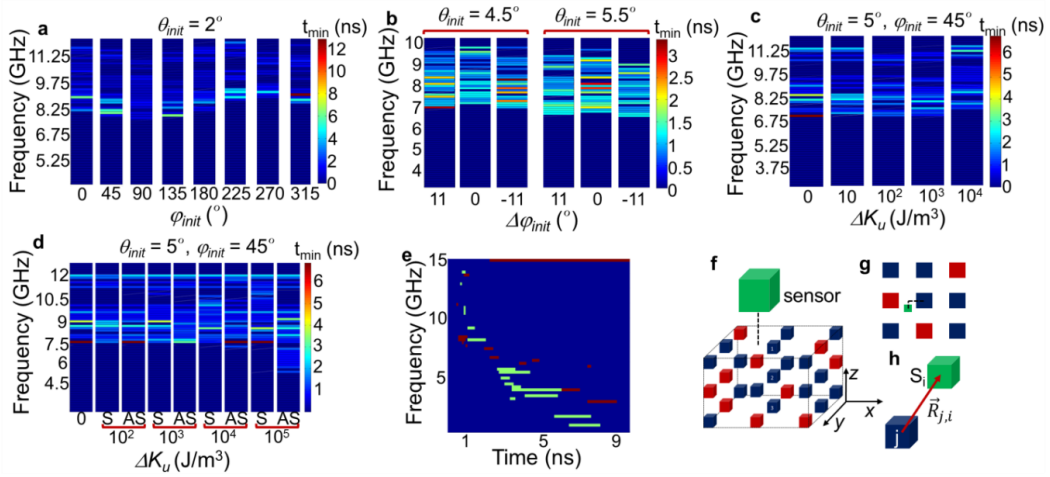

Figure 2-7. (a) The frequencies that the reversal of the central dot (dot 5) is possible for different azimuthal angles (φ_{init}) of the initial magnetization, while the polar angle (θ_{init}) was fixed at 2°. tmin is the minimum excitation time required to achieve the reversal of the central dot. The darkest blue is the background. (b) Frequencies that the reversal of the central dot is possible for φ_{init} = 45, 45±11° at θ_{init} = 4.5 or 5.5°. (c) The frequencies that the reversal of the central dot is possible for different levels of perturbation in the anisotropy constant with φ_{init} = 45° and θ_{init} = 5°. (d) The frequencies that the reversal of the central dot is possible for different levels of dispersion in the anisotropy constant, for both a symmetric (S) and an asymmetric (AS) case with φ_{init} = 45° and θ_{init} = 5°. In the case of S, the anisotropy value of dots 1, 3, 7, and 9 is modified as $K_u+\Delta K_u$. For the AS cases, the anisotropy values of dots 1, 2, 5, and 7 are modified as $K_u+\Delta K_u$, $K_u+0.5\Delta K_u$, $K_u-0.5\Delta K_u$, and $K_u-\Delta K_u$, respectively. (e) The excitation frequencies and times that the reversal of the central dot of the bottom (top) layer is possible for the initial state of all the dots being up are shown with green (red). $K_{u,1}$ = 0.6×10^6 J/m^3 and $h_{mw,1}$ = 270 Oe ($K_{u,2}$ = 1×10^6 J/m^3 and $h_{mw,2}$ = 300 Oe) are the anisotropy and microwave field for the bottom (top) layer of a 3×3×2 matrix of dots, respectively. (f) Schematic of the relative position of a sensor in a 3D matrix of dots. (g) An asymmetric sensing point from the top view (green square is the sensor position). (h) A relative position of the dot j and a sensing point S_i.

The proposed method of the selective reversal of the central dot in a two-dimensional N×N matrix can be expanded to the multilevel[193,194] matrices (N×N×P) for three-dimensional recording. If each of the layers of the dots

magnetostatically interacts with the other layers, an additional dimension of collective modes is added. As we are interested in the selective reversal of the central dot of each of the layers, introducing asymmetry in the excitation or magnetic characteristics among the layers is required. Figure 2-7(e) shows the frequencies for selective reversal of the central dot in either the top (red color) or bottom (green color) layer of a 3×3×2 matrix, where the initial state of the dots is up. The collective sensing for such three-dimensional matrices can be realized using the fact that, for each of the possible states of a 3D matrix, the combination of the stray field in the x and y directions for an asymmetric point relative to the matrix is non-degenerate (Fig. 2-7(f,g)). The measured stray field can be compared with an existing table to relate the sensed values to the possible states of the matrix. It is also possible to reconstruct the magnetization states without the comparing table. The magnetic dot *j* generates the stray field of $\vec{H}_{j,i} = \frac{1}{4\pi}\left[\frac{3\vec{R}_{j,i}\left(\vec{M}_j \cdot \vec{R}_{j,i}\right)}{\left|\vec{R}_{j,i}\right|^5} - \frac{\vec{M}_j}{\left|\vec{R}_{j,i}\right|^3}\right]$, at the sensing point of S_i (Fig. 2-7(h)). Assuming $\vec{M}_j = M_s m_{z,j}\hat{z}$, $\vec{H}_{j,i}$ in the *x* direction is $H_{x,j,i} = m_{z,j}A_{j,i}$, where $A_{j,i} = \frac{M_s}{4\pi}\left[\frac{3R_{x,j,i}R_{z,j,i}}{\left|\vec{R}_{j,i}\right|^5}\right]$. Therefore, the total stray field generated from all the dots of the matrix in the *x* direction at S_i is $H_{T,x,i} = \sum_{j=1}^{N\times N\times N'} A_{j,i}m_{z,j}$. Consequently, by sensing N×N×P non-degenerate points in the space, and knowing the position of the dots and the sensing points, we can calculate the magnetization of the dots using

$$\begin{bmatrix} m_{z,1} \\ \vdots \\ m_{z,N^2\times N'} \end{bmatrix} = \begin{bmatrix} A_{1,1} & \cdots & A_{N^2\times N',1} \\ \vdots & \ddots & \vdots \\ A_{1,N^2\times N'} & \cdots & A_{N^2\times N',N^2\times N'} \end{bmatrix} \begin{bmatrix} H_{T,x,1} \\ \vdots \\ H_{T,x,N^2\times N'} \end{bmatrix}. \quad (2\text{-}16)$$

2.6 Summary

A method for the magnetization reversal of a single nanodot by excitation in a matrix of dots was proposed. This method utilizes microwave-assisted magnetization reversal, considering the inherent collective modes of the magneto-statically interacting dots. The possibility of reversal of only one dot in a matrix of dots from any independent initial magnetization state with out-of-plane crystalline anisotropy was demonstrated numerically. In addition, the theory behind the proposed selective reversal was discussed in more detail. The proposed method can be utilized in microwave-assisted switching for storage densities as high as 10 Tb/in^2, with write heads suitable for densities of 1.2 Tb/in^2, as well as in defect mode magnonic crystals in order to tune their band-structures.

Chapter 3: Reversal selectivity in centro-symmetric nanodot matrices by common current excitation

3.1 Introduction

The collective behaviors of magnetic systems have been a subject of study for decades. Quantum mechanical studies of spin-state phases and solitons in exchange-coupled spin chains,[195-198], and classical or semi-classical studies of magnonic crystals[199-203] are examples of such a research topic. However, utilizing the reciprocal interactions among the magnetic domains for novel magnetization reversal processes has just recently attracted attention. Toggling core reversal of adjacent vortex structures by common excitation with a microwave field,[204] patterned state formation in a matrix of vortex domains under different microwave frequencies,[205] and magnetization reversal of a single dot in a matrix of perpendicularly magnetized dots using excitation of collective modes[206] are the recent demonstrations of selectivity in magnetization reversal using collective behaviors. The spin-transfer torque (STT) phenomenon has enabled inducing magnetization auto-oscillations and reversal using spin-polarized currents in spin-valves, magnetic tunnel junctions, and ferromagnetic/non-magnetic metal bi-layers or multi-layers.[26-33] Although there have been demonstrations of multi-bit data storage in a single in-plane magnetized cell using STT[207] and multi-level structures,[208] the challenges of

future high density random access memory with closely-packed high-coercivity magnetic nanodots have to be addressed.

In this chapter, the possibility of individually reversing the magnetization of magnetic dots in a 2×2 matrix using common current excitation is investigated. In such a magnetic dot matrix, where all of the parameters and initial conditions are the same, spatiotemporal interaction and interference are required to separate the individual dynamics in the phase space. It is demonstrated that through controlled modulation of the spin-polarized current,[209-211] the inherent magneto-static interaction in the matrix sites provides the possibility of such spatiotemporal interference, resulting in a temporally-spaced magnetization reversal of different sites of the matrix.

3.2 Reversal mechanism of individual selectivity

3.2.1 The system and its governing equations

Figures 3-1(a) and 1(b) show the schematic configuration of the magnetic dots in a 2×2 matrix, the magnetization directions ($\vec{M}_i$, where i = 1, 2, 3, or 4), trajectories and oscillatory parts ($\vec{m}_i$), and respective phases (φ_i). The current density (J_T) polarized in the z direction, the in-plane dc magnetic field ($\vec{h}_{dc}$), and its angle (φ_h) with respect to the x direction are depicted in Fig. 3-1(a) and 3-1(b). A uniaxial crystalline anisotropy in the z direction with an anisotropy constant of K_u is assumed. The dc magnetic field $\vec{h}_{dc}$ causes a polar tilt ($\theta_{\|}$) in the easy axis of the magnetization. The study focuses on the initial magnetization of all the dots having the same polar ($\theta_i(0) = \theta_0$) and azimuthal

angle ($\varphi_i(0) = \varphi_0$). The purpose of this study is to separate the phases of dynamics among the dots in order to separate their reversal processes. Considering the individual dots and their initial magnetizations, this aim seems impossible, as all of them share the same driving force and initial point in the phase space. However, by categorizing the dots into two dyadic pairs of 1-4 and 2-3, we find that in the $\hat{e}_1 - \hat{e}_2$ coordination, ($\hat{e}_1$ ($\hat{e}_2$) is parallel (perpendicular) to the center-center connection line of each dyadic pair in Fig. 3-1(c)), and the initial phases of these two dyadic pairs are separated by $\pi/2$. An example of phase separation of the dyadic pairs in the $\hat{e}_1 - \hat{e}_2$ coordination is depicted in Fig. 3-1(c), where $\varphi_i = \pi / 4$ (i = 1 to 4) in the *xyz* coordinates. From the $\pi/2$ phase difference in the $\hat{e}_1 - \hat{e}_2$ coordinates, the first stage of the separation in the dynamics should be through inducing disparity in the dyadic pairs excitation properties, as shown below.

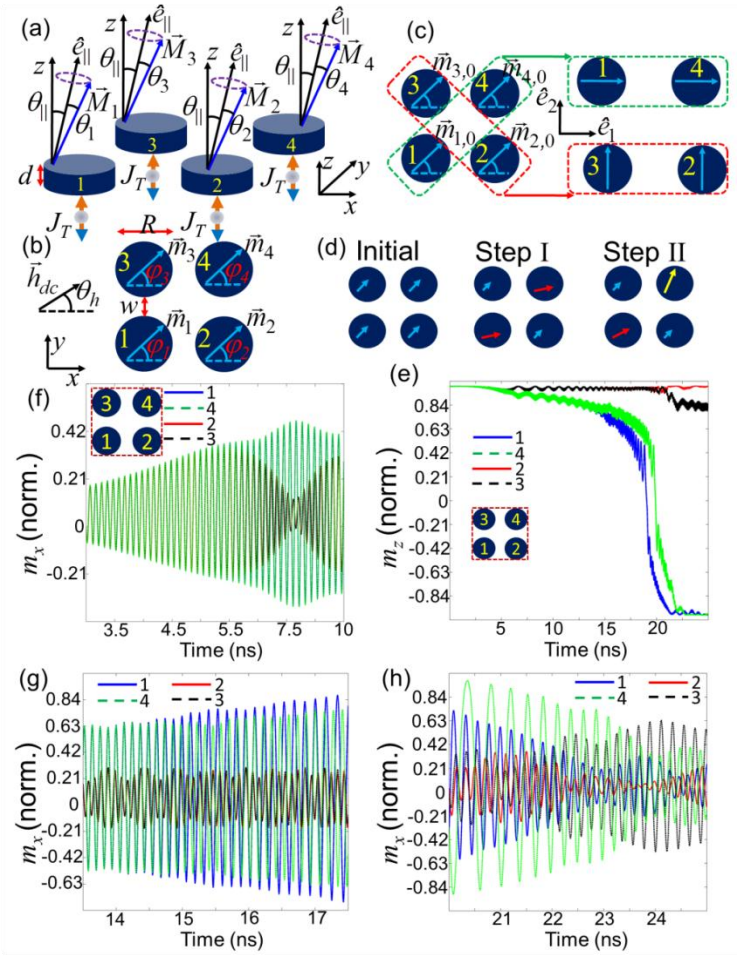

Figure 3-1. (a,b) The schematic diagram of the system, the magnetization directions, the polarized current J_T, and the dc magnetic field. (c) An example of the phase difference of the dyadic pairs in the $\hat{e}_1\hat{e}_2\hat{e}_{||}$ coordinate system. (d) The schematic diagram of the reversal process steps. (e) The temporal evolution of m_z for all the four dots, while $\vec{h}_{dc} = 200\,\hat{x}$ Oe, $J_{dc,1} = 7.5\times10^9$ A/m^2, $J_{dc,2} = 6\times10^9$ A/m^2, $\omega_{ac} = 2\pi\times10^{10}$ rad/s, $J_{ac} = 3.75\times10^{10}$ A/m^2, $T_{ac} = 6$ ns, $\varphi_{ac} = \pi/4$. (f) The temporal evolution of m_x from 3 to 7.5 ns (where step I happens). (g) m_x from 13.5 to 17.5 ns (where step II happens). (h) m_x from 20 to 25 ns (where all the phases are separated).

In the system described above, the controlling signal is the polarized current density J_T of the form

$$\begin{cases} J_T = J_{ac}\cos\left(\omega_{ac}t + \varphi_{ac}\right) + J_{dc,1} & (0 < t \le T_{ac}) \\ J_T = J_{dc,2} & (t > T_{ac}) \end{cases} \tag{3-1}$$

where J_{ac} is the amplitude of the microwave modulation of the current density with an angular frequency of ω_{ac} and the initial phase of φ_{ac}, applied for the duration of T_{ac}. $J_{dc,1}$ ($J_{dc,2}$) is the dc current density at $0 < t \le T_{ac}$ ($t > T_{ac}$). We can describe the magnetization oscillation of the dyadic pairs in the rotating frame as $\vec{C}_{1-4(2-3)} = \left(c_{1-4(2-3)}(t) + c.c.\right)\left(\hat{e}_1 - i\hat{e}_2\right)$, where $c_{1-4(2-3)}(t)$ is a complex time-varying coefficient and *c.c.* is its complex conjugate. By simplifying the Landau-Lifshitz-Gilbert (LLG) equation in the $\hat{e}_1\hat{e}_2\hat{e}_{||}$ coordinate system ($\hat{e}_{||}$ is parallel to the easy axis direction in Fig. 3-1(a)), including the Slonczewski spin-transfer term [32], we get [212,213]

$$\frac{dc_k}{dt} = -\mathrm{A}_{G_k}(p_k)c_k + \mathrm{A}_{STT_k}(p_k)c_k - j\omega_k(p_k)c_k + f_{J,ac} + f_{h,s} + f_{h,e} \qquad (3\text{-}2)$$

where k refers to either the 1-4 or 2-3 dyadic pair, p_k is the oscillation power, $\mathrm{A}_{G_k}(p_k)$ is the damping term due to the Gilbert damping, $\mathrm{A}_{STT_k}(p_k)$ is the damping or anti-damping term due to STT, and $\omega_k(p_k)$ is the oscillation frequency. $f_{J,ac}$, $f_{h,s}$, and $f_{h,e}$ are the forcing terms due to the ac current, self-dipolar microwave field of the dyadic pair, and the microwave dipolar field from the other dyadic pair, respectively. Assuming small oscillation power p,

$$\omega_k = \gamma\left(H_{A_{dc}} + H_{d_k}^{||}\right), \quad \mathrm{A}_{G_k} = \alpha\omega_k, \quad \mathrm{A}_{STT_k} = \sigma J_{dc,q}\omega_k,$$

$$f_{J,ac} = \frac{\sigma}{2\sqrt{2}}\tan\left(\theta_{||}\right)J_{ac}e^{-j(\omega_{ac}t-\varphi_{ac})}, \quad f_{h,s} = \sqrt{\frac{p_k}{2}}\gamma N_{op_{kk}}\sin\left(\theta_{||}\right)\cos\left(\theta_{||}\right)e^{-j\left(\omega_k t+\varphi_k(t)\right)},$$

$$f_{h,e} = \sqrt{\frac{p_{k'}}{2}}\gamma N_{op_{k'k}}\sin\left(\theta_{||}\right)\cos\left(\theta_{||}\right)e^{-j\left(\omega_{k'}t+\varphi_{k'}(t)\right)}, \qquad (3\text{-}3)$$

where $H_{A_{dc}} = \left(\left(\frac{2K_u}{\mu_0 {M_s}^2} \right)^2 + \left| \vec{h}_{dc} \right|^2 \right)^{1/2}$ contains both the contributions from the crystalline anisotropy field ($\frac{2K_u}{\mu_0 {M_s}^2} \hat{z}$) and the in-plane dc field ($\vec{h}_{dc}$), and points along the tilted easy axis ($\theta_{||}$ from the z direction). $H_{d_k}^{||} = \left(-M_{||_k} N_{op_{kk}} - M_{||_{k'}} N_{op_{k'k}} \right)$ is the dipolar field caused by the self-interaction in each dyadic pair ($-M_{||_k} N_{op_{kk}}$) and the mutual interaction of the dyadic pairs ($-M_{||_{k'}} N_{op_{k'k}}$). $M_{||_{k(k')}}$ is the magnetization of $k(k')$ in the direction of $\hat{e}_{||}$. $N_{op_{kk}} \approx \frac{V}{4\pi {\rho_{kk}}^3}$ and $N_{op_{k'k}} \approx \frac{2V}{4\pi {\rho_{k'k}}^3}$ are the demagnetizing coefficients of self and mutual dipolar interactions, respectively, where $\rho_{kk} = \sqrt{2}(R+w)$, $\rho_{k'k} = (R+w)$, R is the diameter of the dots, w is the center to center spacing between the dots, and V is the volume of the dots. γ is the gyromagnetic ratio, α is the Gilbert damping ($\sigma = \frac{\gamma \hbar \varepsilon}{\mu_0 e d M_s}$), $\hbar$ is the reduced Plank constant, ε is the efficiency of the STT, e is the electron charge, d is the thickness of the magnetic dots, and M_s is the saturation magnetization. k and k' refer to either the dyadic pair 1-4 or 2-3, while $k \neq k'$. q refers to the first or second part of the current signal which is defined in Eq. (3-1). $\varphi_{k(k')}(t)$ is the dynamic part of the phase of the $k(k')$ dyadic pair.

3.2.2 Dephasing of the dyadic pairs dynamics

By assuming $c_k = \sqrt{p_k} e^{-j(\omega_k t + \varphi_k(t))}$ we can separate Eq. (3-2) into two dependent differential equations for the oscillation power and the phase as

$$\frac{dp_k}{dt} = 2p_k\left(A_{STT_k} - A_{G_k}\right) + \frac{\sigma\sqrt{p_k}}{\sqrt{2}}\tan\left(\theta_{||}\right)J_{ac}\cos\left(\psi_{ac_k}\right) + \left(\sqrt{2}p_k\gamma N_{op_{kk}} + \sqrt{2p_k p_{k'}}\gamma N_{op_{k'k}}\cos\left(\psi_{k'k}\right)\right)\sin\left(\theta_{||}\right)\cos\left(\theta_{||}\right)$$

$$\frac{d\varphi_k}{dt} = \frac{\sigma}{2\sqrt{2p_k}}\tan\left(\theta_{||}\right)J_{ac}\sin\left(\psi_{ac_k}\right) + \left(\frac{\sqrt{p_{k'}}}{\sqrt{2p_k}}\gamma N_{op_{k'k}}\sin\left(\psi_{k'k}\right)\right)\sin\left(\theta_{||}\right)\cos\left(\theta_{||}\right),$$

(3-4)

where $\psi_{ac_k} = (\omega_k - \omega_{ac})t + \varphi_{ac} + \varphi_k(t)$ and $\psi_{k'k} = (\omega_k - \omega_{k'})t + \varphi_k(t) - \varphi_{k'}(t)$. Since the possibility of separation of the phases in the dyadic pairs is investigated, it is assumed that $\varphi_{k'}(t)$ is fixed and equal to $-\pi/2$, while $\varphi_k(0) - \varphi_{k'}(0) = \pi/2$. Initially, ω_k, A_{G_k}, and A_{STT_k} are the same for both of the dyadic pairs, and both of them have the same oscillation power ($p_k = p_{k'}$). Assuming $\omega_{ac} = \omega_{k(k')}$, we have $\psi_{ac_k} = \varphi_{ac} + \varphi_k(t)$ and $\psi_{k'k} = \varphi_k(t) + \pi/2$. From the phase equation in Eq. (3-4), it is inferred that the respective phase of the dyadic pair k, $\varphi_k(t)$ can be controlled by changing φ_{ac}. The term containing $\sin\left(\psi_{ac_k}\right)$ determines the controllability of the phase dynamics of each dyadic pair with varying φ_{ac}, while the term containing $\sin(\psi_{k'k})$ causes the separation of the phase dynamics of the two dyadic pairs. We can also notice that if the tilt ($\theta_{||}$) is zero, there will be no difference between the dyadic pairs in the dynamics, therefore the separation of their phases will not be possible. It is worth noting that the tilt is induced due to the in-plane dc field. The in-plane dipolar field terms are not included in Eq. (3-4), because the dots in each of the dyadic pairs are assumed to have the same phases of oscillation, resulting in the canceling out of the effects of in-plane dipolar interactions. As the phase φ_k becomes non-zero, the power equation in Eq. (3-4) indicates that the power growth rate of p_k becomes different from that of $p_{k'}$. As an example, if we

choose φ_{ac} such that at $t = t_0$, $\sin(\psi_{ac_k}) > 0$ and $\cos(\psi_{ac_k}) < \sin(\psi_{ac_k})$, after a short time, δt, the change in the phases $\delta\varphi_{k(k')}$ will follow $\delta\varphi_k > \delta\varphi_{k'} > 0$ if $\frac{\sigma}{2\sqrt{2p_k}}\tan(\theta_{\|})J_{ac} > \frac{\sqrt{p_{k'}}}{\sqrt{2p_k}}\gamma N_{op_{k'k}}\sin(\theta_{\|})\cos(\theta_{\|})$. Consequently, $\cos(\psi_{ac_k} + \delta\varphi_k) < \cos(\psi_{ac_{k'}} + \delta\varphi_{k'})$, $\cos(\psi_{k'k} + \delta\varphi_k - \delta\varphi_{k'}) < 0$ and $\cos(\psi_{kk'} + \delta\varphi_{k'} - \delta\varphi_k) > 0$, which results in the growth of the oscillation power $p_{k'}$ and suppression of p_k in the δt time step.

Figure 3-1(d) shows the schematic of the reversal process, and Figs. 3-1(e-h) show an example of the reversal process that has been solved numerically using the object oriented micromagnetic framework (OOMMF). It is assumed that M_s = 10^6 A/m, K_u = 5×10^5 J/m^3, $\alpha = 0.005$ (based on the material parameters reported from CoFeB-MgO perpendicular magnetic tunnel junctions[29]), exchange constant A = 10^{-11} J/m, $\gamma/2\pi = 3.5\times10^4$ Hz·(m/A), R = 10 nm, w = 15 nm, d = 2 nm, $\vec{h}_{dc} = 200\,\hat{x}$ Oe, $J_{dc,1} = 7.5\times10^9$ A/m^2, $J_{dc,2} = 6\times10^9$ A/m^2, $J_{ac} = 3.75\times10^{10}$ A/m^2, T_{ac} = 6 ns, ε = 1, $\varphi_{ac} = \pi/4$, $\omega_{ac} = 2\pi\times10^{10}$ rad/s, 5° initial tilt of the magnetization with respect to the z direction, $\varphi_i = \pi/4$ (i = 1 to 4), and a simulation cell size of 2.5 nm×2.5 nm×1 nm. Figure 3-1(e) shows the dynamics of the normalized magnetization (m_z) in the z direction for all the four dots in 25 ns. In this particular case, only the 1-4 dyadic pair goes through the reversal during this time. There is also a disparity in the reversal time between the two dots of the 1-4 dyadic pair, as discussed later. So far, the origin of the dyadic pair separation in dynamics has been discussed. For this example, the dyadic pair separation can be clearly observed in Fig. 3-1(f) which shows

the dynamics of the normalized magnetization in the x direction, m_x (also refer to the schematic of the initial state and the step I in Fig. 3-1(d)). It is worth emphasizing that in the time-range ($3 < t < 7.5$ ns) shown in Fig. 3-1(f), the blue (dot 1) and the green (dot 4) curves are exactly the same (dyadic pair 1-4), and the red (dot 2) and the black (dot 3) curves coincide completely with each other as well (dyadic pair 2-3).

3.2.3 Dephasing of the individual elements dynamics

Assuming that the dyadic pair k grows faster, therefore $M_{||_k}$ decreases more than $M_{||_{k'}}$. Since $N_{op_{k'k}} = 4\sqrt{2}N_{op_{kk}}$, the consequence is $H_{d_k}^{||} < H_{d_{k'}}^{||}$. It indicates that the frequency of the oscillation of the dyadic pair k will be lower than k', $\omega_{k'} > \omega_k$ (see Eq. (3-3)). Consequently, the forcing term of $f_{h,e}$ on k will have a higher frequency ($\omega_{k'}$) than the auto-oscillation of k (ω_k). $f_{h,e}$ can manifest its effect in two ways: one is due to the nonlinearity of the auto-oscillation which results in frequency pulling in both k and k',[212] and the other is by inducing a higher frequency in the auto-oscillation through phase separation of the elements of the dyadic pair k. The functionality of the dyadic pair k frequency on the respective phases ($\varphi_{k,r}$) of its two elements has the form of

$$\omega_k = \gamma\left(H_{A_{dc}} + H_{d_k}^{||} - M_{IP_k} N_{IP-||_{kk}} \sin\left(\varphi_{k,r}\right)\right). \tag{3-5}$$

The last part of Eq. (3-5) represents the self-dipolar field in the direction of $\hat{e}_{||}$ due to the in-plane (in the xy plane) part of the magnetization (M_{IP_k}),

where $N_{IP-\|kk}$ is the corresponding phenomenological self-demagnetizing coefficient. $N_{IP-\|kk}$ depends on the multipolar interactions due to finite shapes and comparable distance of the elements, and also depends on $\theta_{\|}$ and the trajectory of the oscillations. As the oscillation in the dyadic pair k grows closer to be in-plane (an increase in M_{IP_k} and a decrease in $M_{\|_k}$), the contribution of $-M_{IP_k} N_{IP-\|kk} \sin(\varphi_{k,r})$ becomes more important. It should be noted that the effect of this dipolar field is different from the self-dipolar microwave field $f_{h,s}$, and is of a static nature. The static dipolar field induced by the in-plane part of the magnetization from the other dyadic pair (k') has been neglected, since it is assumed that the oscillation power of k is much larger than that of k'. Equation (3-5) shows that ω_k will increase or decrease by deviation of $\varphi_{k,r}$ from zero, which can be aligned with the effect of the forcing term $f_{h,e}$. Any disparity in the phase will result in a difference in the power growth rate in accordance with the previous discussion on phase separation of dyadic pairs (see Eq. (3-2) and Eq. (3-4)). Figure 3-1(g) shows the phase separation of the elements 1 and 4 corresponding to the step II in Fig. 3-1(d) for 13.5 < t < 17.5 ns. As the phases are separated in 1-4 dyadic pair elements, the other 2-3 dyadic pair will also tend to separate their phases due to in-plane interaction. Such a separation of all the element phases can be seen in Fig. 3-1(h) for 20 < t < 25 ns.

3.3 Effect of the excitation parameters on selectivity

The phase (φ_{ac}), duration (T_{ac}), and amplitude (J_{ac}) of the ac current as well as the dc current ($J_{dc,1(2)}$) of the J_T signal can be utilized as control variables for sequencing the elements reversal. Figure 3-2(a) shows the reversal sequence with respect to the variation of φ_{ac} with a step of $\pi/25$ for $T_{ac} = 6$ ns. The blue colors in the graphs correspond to the states with reversal of an individual dot, which typically happens right after the initial configuration (marked by red). The orange and yellow colors correspond to a reversal of three or four dots. The schematic of the initial state (red) as well as the states of reversal of a dyadic pair (cyan) have been depicted in Fig. 3-2(a). In the schematic of dot configurations, the black dot indicates that the dot is reversed, and the green dot is for a non-reversed one. Figure 3-2(a) clearly represents the possibility of individual reversal of dots or dyadic pairs by varying φ_{ac} . Figure 3-2(b) shows the individual site reversals that are possible for each phase considered in Fig. 3-2(a). Figure 3-2(c) shows the temporal emerging of the reversal states for different values of φ_{ac} $(0 - 2\pi)$ and T_{ac} $(3 - 10$ ns). For all of the studied values of T_{ac}, we can selectively switch either a dyadic pair 1-4 or 2-3 by varying φ_{ac} . However, with increasing T_{ac} the reversal process is faster. As the phase separation of the elements of a particular dyadic pair requires sufficient time for dipolar interactions, the possibility for sequencing the reversal of individual elements decreases by increasing T_{ac} .

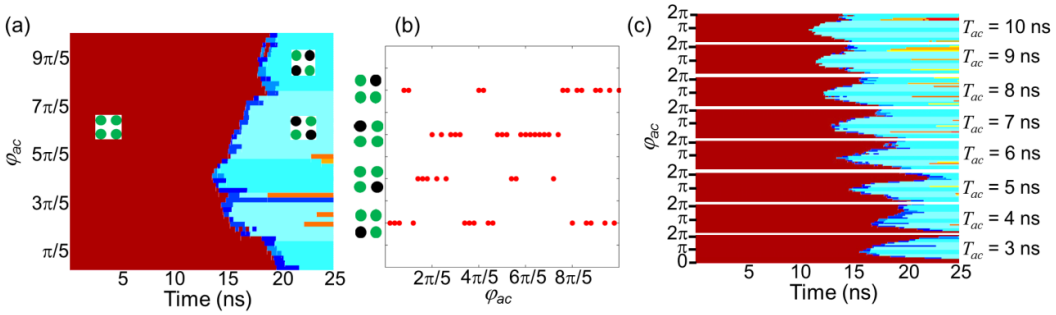

Figure 3-2. (a) The reversal states at different times for a variation of φ_{ac} from 0 to 2π with a step of π/25 and T_{ac} = 6 ns. (b) The individual site reversal for each phase corresponding to the four blue colors in (a). (c) The reversal states at different times for a variation of φ_{ac} from 0 to 2π with a step of π/10, at different values of T_{ac}. $J_{dc,1}$ = 7.5×10^9 A/m^2, $J_{dc,2}$ = 6×10^9 A/m^2, and J_{ac} = 4.5×10^{10} A/m^2 are used. The blue colors in the graphs correspond to the states with reversal of an individual dot. The two cyan colors correspond to the dyadic reversal states. The orange or yellow colors correspond to the reversal of three or four dots. The schematic of the initial state as well as the states of reversal of a dyadic pair have been depicted in (a). In the schematic dot configuration, the black color indicates the dot is reversed, and green color is for the non-reversed dot.

Variation of the amplitude of the dc currents ($J_{dc,1(2)}$) in J_T modifies A_{STT} in Eq. (3-2) and Eq. (3-4), affecting the interaction time among the dyadic pairs as well as the individual elements. For relatively high values of $J_{dc,1}$ and $J_{dc,2}$, the interaction time required for separation of reversal processes of the individual dots is not enough, resulting in no individual selectivity as shown in Fig. 3-3(a). For relatively low values of $J_{dc,1}$ or $J_{dc,2}$ either the reversal process becomes impossible (if $A_{STT} < A_G$) or it happens in longer time scales (refer to Fig. 3-3(a)). The effect of the amplitude of the ac current (J_{ac}) is depicted in Fig. 3-3(b). It can be seen that the dyadic pair reversal as a function of φ_{ac} is more sensitive to J_{ac} than T_{ac} or $J_{dc,1(2)}$, comparing Fig. 3-3(b) with

Fig. 3-2(c) and Fig. 3-3(a). The reason is due to the direct dependence of the dyadic pair phase-differential-equation ($d\varphi_k / dt$) on J_{ac} in Eq. (3-4).

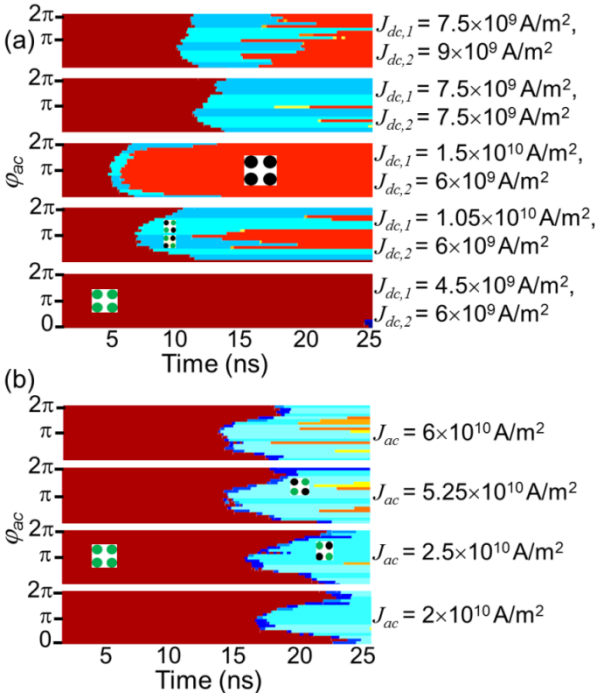

Figure 3-3. (a) The reversal states at different times for a variation of φ_{ac} from 0 to 2π with a step of π/10, at different values of $J_{dc,1}$ and $J_{dc,2}$. T_{ac} = 6 ns and J_{ac} = 4.5×10^{10} A/m^2 are used. (b) The reversal states at different times, for a variation of φ_{ac} from 0 to 2π with a step of π/10, at different values of J_{ac}. T_{ac} = 6 ns, $J_{dc,1}$ = 7.5×10^9 A/m^2, and $J_{dc,2}$ = 6×10^9 A/m^2 are used. The blue colors in the graphs correspond to the states with reversal of an individual dot. The two cyan colors correspond to the dyadic reversal states. The other orange or yellow colors correspond to other reversal of three or four dots.

3.4 Discussion

For applications and experimental demonstrations, there will be discrepancies from the ideal system that is assumed. The shape differences among the dots will affect the values of demagnetization coefficients $N_{op_{kk(k'k)}}$ and $N_{IP-||_{kk}}$, and consequently some of the coefficients in Eq. (3-4) and Eq. (3-5)

will be modified. As an example, the crystalline anisotropy has been dispersed among the dots, while the other parameters and excitation variables were kept the same as the case studied in Fig. 3-2(a). The results in Fig. 3-4(a) show that the reversal spectrum represents both the individual and dyadic selectivities. However, despite the high similarity of the dyadic selectivity in Fig. 3-2(a) and Fig. 3-4(a), the individual dot reversal states do not coincide completely among the two graphs. The reason is that the dyadic selectivity occurs in a more linear fashion than the individual selectivity which strongly depends on the initial conditions, and the stage where the individual elements begin to dephase. A relatively large change of symmetry in the shape or crystalline anisotropy (for the case considered here, large change means more than few thousands of J/m^3) among the nanodots are expected to result in the system being less selective in switching, similar to what happens to the synchronization mechanism of STT oscillators for relatively large shape differences among the nanomagnets.[214]

It is worth noting that the more fine resolution in varying φ_{ac} makes more reversal states accessible selectively, as can be inferred by comparing Fig. 3-2(a) [a step of $\pi/25$] to Fig. 3-2(c) [a step of $\pi/10$] with T_{ac} = 6 ns. It is initially assumed that the initial phase of the magnetization of all the dots is the same as $\varphi_i = \pi / 4$ for i = 1 to 4 (i.e. the initial phases of dyadic pairs are $\varphi_{1-4} = 0$ and $\varphi_{2-3} = \pi / 2$) and also that the in-plane dc field $\vec{h}_{dc}$ is applied along the x direction (φ_h = 0°, refer to Fig. 3-1(b)). The effects of varying φ_h and the initial φ_i on the reversal spectrum are conceptually the same (refer to Eq. (3-4) and the subsequent discussion on the reversal process). The phase and power differential equations in Eq. (3-4) are modified with a different initial φ_i or φ_h

through the terms containing ψ_{ac_k} and $\psi_{k'k}$. Figure 3-4(b) shows an example where φ_h = 5° (relatively a small change in φ_h, equivalent to a small change in φ_i), while the other parameters and excitation variables are kept the same as the case in Fig. 3-2(a). All the dyadic and individual selectivities are still achieved, and the reversal spectrum is highly similar to the cases of Fig. 3-2(a) and Fig. 3-4(a).

Fig. 3-4(c) shows an example where initial $\varphi_i = \pi / 12$ for i = 1 to 4 (relatively a large change in the initial φ_i, equivalent to a large change in φ_h), while the other parameters and excitation variables are kept the same as the case in Fig. 3-2(a). All the dyadic and individual selectivities are still achieved in the reversal spectrum in Fig. 3-4(c), although the detailed characteristics of dyadic selectivity are modified. Figure 3-4(d) shows the individual selectivity at each phase for the graphs of Fig. 3-4(a), Fig. 3-4(b), Fig. 3-2(a) (for a reference), and Fig. 3-4(c). As expected, there are several common phases for achieving the same individual selectivity in the reversal spectra presented in Fig. 3-2(a), Fig. 3-4(a), and Fig. 3-4(b).

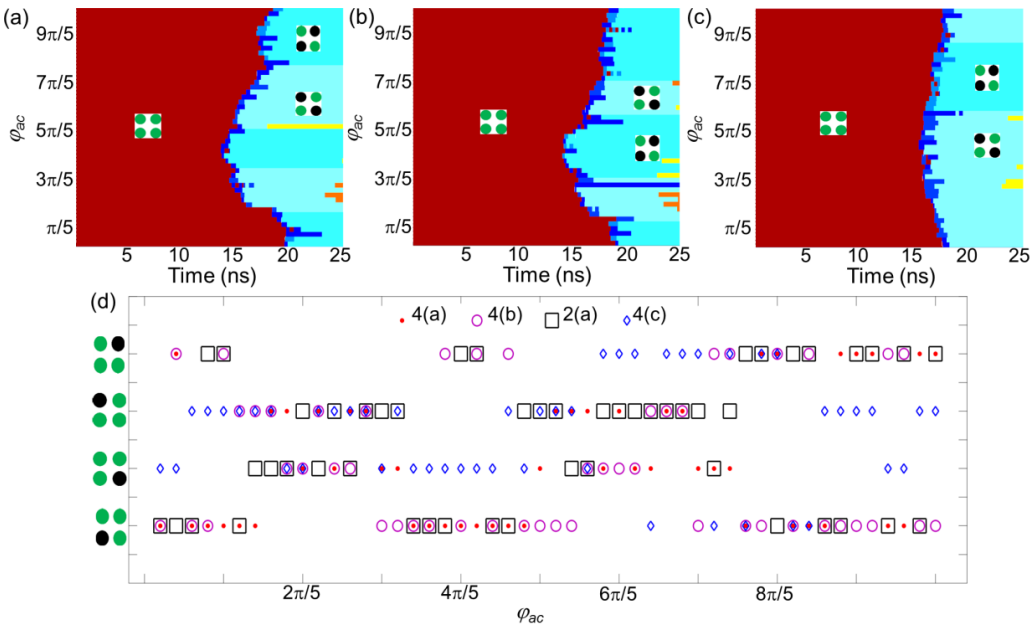

Figure 3-4. The reversal states at different times for a variation of φ_{ac} from 0 to 2π with a step of π/25 and T_{ac} = 6 ns, $J_{dc,1}$ = 7.5×10^9 A/m^2, $J_{dc,2}$ = 6×10^9 A/m^2, and J_{ac} = 4.5×10^{10} A/m^2. (a) K_u is dispersed among the dots as K_{u0}+500, K_{u0}-250, K_{u0}-500, and K_{u0}+250 in J/m^3 for dots 1– 4, respectively. The blue colors in the graphs correspond to the states with reversal of an individual dot. The two cyan colors correspond to the dyadic reversal states. The orange or yellow colors correspond to the reversal of three or four dots. (b) The dc in-plane magnetic field $\vec{h}_{dc}$ is applied 5° away from the x direction (φ_h = 5°, refer to Fig. 3-1(b)). (c) The initial in-plane part of the magnetization has an azimuthal angle of $\varphi_i = \pi/12$ with respect to the x direction, for i = 1 to 4. (d) The individual site reversal (corresponding to the four blue colors) for each phase in the graphs of Fig. 3-4(a), Fig. 3-4(b), Fig. 3-2(a) (for reference), and Fig. 3-4(c).

As discussed above, the effect of easy axis tilt ($\theta_{||}$) with respect to the z direction is essential for the separation of the phases of the dyadic pairs, and subsequently the phases of individual elements in each dyadic pair. We induce such a tilt by applying an in-plane dc field $\vec{h}_{dc}$. However, instead of applying $\vec{h}_{dc}$, a non-zero $\theta_{||}$ can be achieved by a tilted crystalline anisotropy. The proposed reversal method can be expanded to larger centrosymmetric matrices

with an even number of dots N, such that the center of symmetry is not a magnetic dot itself. Examples of such symmetric structures are hexagonal and octagonal matrices of dots. The number of dyadic pairs will be $N/2$ and the initial phases of the dyadic pairs in the $\hat{e}_1\hat{e}_2\hat{e}_{||}$ coordinate system will be distributed evenly with the spacing of $2\pi / N$. Therefore, sequencing the dyadic pairs in reversal will be possible by varying φ_{ac}, and the above discussions of reversal of individual elements apply as well. Moreover, for larger matrices, a higher order than dyadic pair groupings is possible, which enable the use of different frequencies of microwave current modulation in order to excite different groupings (modes), followed by the same processes of dephasing as described for the dyadic pairs. Therefore, different reversal sequences and patterns can be achieved by varying both the frequency and the phase of the microwave current modulation. A schematic example of the dyadic pair and dyadic quad-dot groupings for a hexagonal matrix is shown in Fig. 3-5. The same concept can also be expanded to three-dimensional centrosymmetric matrices, where the dyadic pair or higher order grouping of the out-of-plane magnetization component correlates the dynamics among the layers of the matrix.

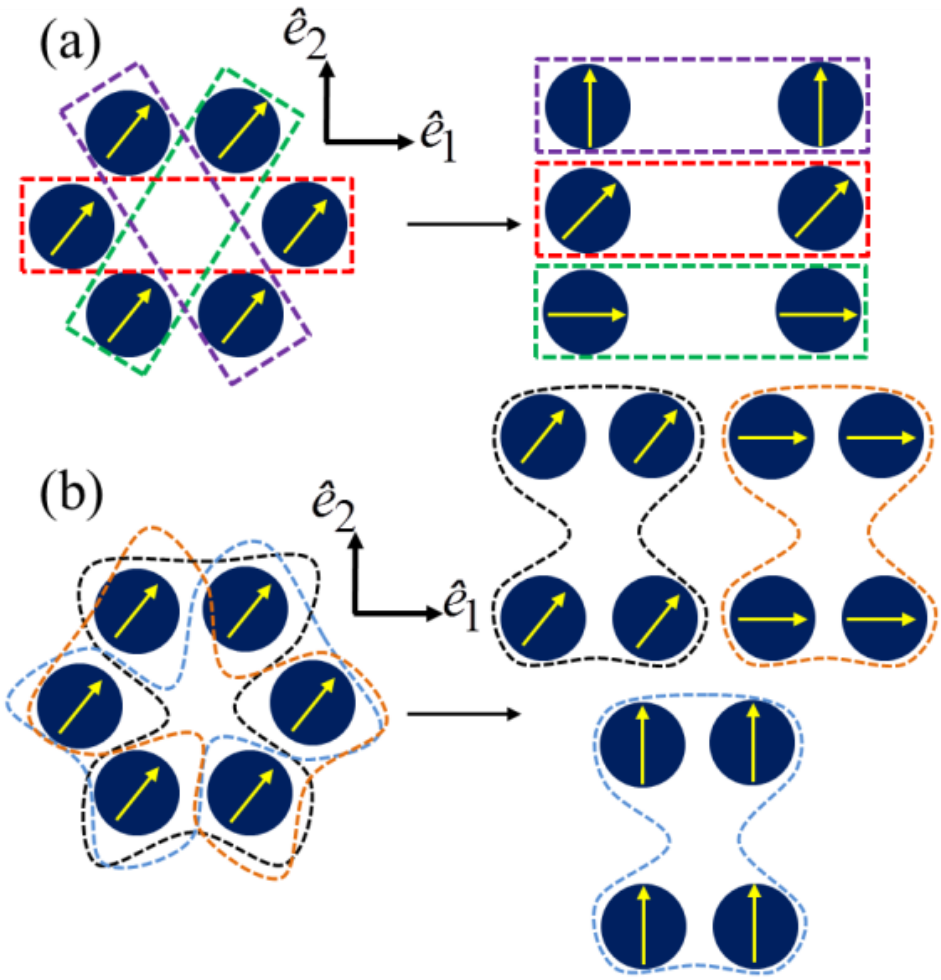

Figure 3-5. Schematic of two different groupings for a hexagonal matrix of dots and respective initial phase separation among them. (a) The dyadic pair grouping, and (b) the dyadic quad-dot grouping.

The reversal mechanism from the initial magnetization state of all the dots pointing up, which is the most symmetric state, and consequently the most difficult one for individual selectivity has been discussed and demonstrated. For different initial states, the above discussions can be utilized by modifying the interaction terms. For example, for the case with one of the dots pointing down, a similar discussion of dyadic pair separation applies, where one of the dyadic pairs becomes a sole element. An issue about the proposed reversal method is

the long time required for selective reversal of individual dots from the initial state of all the dots pointing up (see for example Fig. 3-1(e) and Fig. 3-2(a)). However, for applications, the average switching time required for reversal can be moderate considering each cell consists of four or more bits, and it is possible to switch multiple bits at once. It should be noted that the reversal can be fast for some of the cases, such as dyadic pair reversal from the initial state of all the dots being up as shown in Fig. 3-3(a).

3.4 Summary

A method for magnetization reversal of individual sites of centrosymmetric matrices of perpendicularly magnetized dots by common excitation with a spin-polarized current has been proposed. The spin-polarized current signal consists of a dc-biased ac part followed by a pure dc one. By controlling the magnetostatic interaction among the dots through adjusting amplitudes of the currents, as well as the phase and duration of the ac current, the selectivity in reversal is realized. A theoretical model to explain different steps of the reversal process and investigate the effect of different variables using numerical simulations has been developed. This method can be utilized to tackle microelectronic fabrication challenges for realizing high density perpendicularly magnetized nanodot structures of magnetic random access memory applications with a common access line for multi-bit cells.

Chapter 4: Synchronization of spin-transfer torque oscillators by spin pumping, inverse spin Hall, and spin Hall effects

4.1 Introduction

Recently, the spin-transfer torque (STT) phenomenon has been utilized to develop magnetic nano-oscillators.[32,72-74] Nano-contact or patterned spin-valves and magnetic tunnel junctions (MTJ) have been pursued for achieving spin torque oscillators (STO).[21,23,75,76] Since the power generated by a single nano-oscillator is not able to satisfy the requirements of its targeted applications (communication systems, read/write heads in HDD, microwave current modulation for MTJ MRAMs etc.), there have been many efforts undertaken in order to achieve a synchronization method of multiple oscillators.[75,81-86] In order to synchronize several STOs, a feedback system that can enforce the oscillations to lock to achieve the minimum free energy should exist. Kaka *et al.* demonstrated the first synchronization between two nano-STOs based on spin waves interactions,[75] in which the feedback system was mediated by spin waves. Injection locking is another approach in which an external alternating current is used to lock a group of STOs.[81,86-88] The injection locking has provided inspiration to pursue synchronization in MTJs or spin-valve STOs in series connection, where the stimulated current due to the oscillating magnetoresistance is utilized to form the feedback system and induce locking.[83,89] Difficulties in fabricating spin-valves or MTJ STOs in series

connection have been an obstacle to demonstrate the performance of this synchronization method. A maximum of four nano-contact STOs have been experimentally synchronized so far mediated by anti-vortices.[85] However, a relatively low frequency of vortex oscillators and high current required to induce vortex oscillations are disadvantages of this method.

The spin Hall effect (SHE) has enabled the generation of pure spin currents from charge currents in a high spin orbit coupled material.[215] A charge current is induced in a normal metal due to the inverse spin Hall effect (ISHE), when a spin current is injected into the normal metal.[216-218] The conversion efficiency (spin Hall angle) between a charge current and spin current in the SHE and ISHE processes depends on the strength of spin-orbit scattering in the normal metal. Spin transfer ferromagnetic resonance (ST-FMR), spin pumping, and time-resolved magneto-optical Kerr effect (TR-MOKE) experiments have been pursued in order to quantify the spin Hall angle of different heavy metals such as Pt and Ta.[217,219-223] Pure spin currents generated by the SHE have been implemented to switch a magnetic layer.[26,27,224,225] Moreover, a new type of oscillator based on SHE has been introduced, in which the oscillation mode is a self-localized spin wave bullet,[24,51,78] and a recent experiment has demonstrated its injection locking.[79] The spin Hall oscillators (SHO) can also be realized in nano-magnetic elements as an auto oscillation mode.[50]

A method to synchronize multiple STOs without requiring an external ac excitation is still a subject of study. In this chapter, a synchronization method based on spin pumping, SHE, and ISHE is proposed. The device consists of nano-magnets in junction with a normal metal with high spin-orbit coupling. An accumulative feedback loop for the modulated part of the current is

implemented. Numerical simulations have been carried out to study the effect of the modulated charge current due to spin pumping and ISHE, on the magnetization oscillation of nano-magnets. It is found that under certain circumstances, synchronization of the oscillation of multiple nano-magnets is possible.

4.2 Proposed method

The proposed oscillator system consists of N elliptic ferromagnetic single domain elements in junction with a high spin-orbit scattering non-magnetic (NM) metal shown in Fig. 4-1(a). Magnetic elements (F_i to F_{i+1}) are assumed to be magnetically isolated. The NM strip is as wide as the long axis of the magnetic elements. If a charge current ($\vec{J}_{in}$) is applied to the device, it gives rise to a transverse pure spin current due to SHE (see Fig. 4-1(d)). The generated spin current induces magnetization oscillations in the magnetic elements. Figures 4-1(b) and 4-1(c) demonstrate the configuration of the initial magnetization in the i^{th} magnetic element ($\vec{M}_{0_i}$) and the spin polarization direction ($\hat{s}$) of the pure spin current generated by SHE. The magnetization precession in each magnetic element pumps spins into the NM metal. Subsequently, the pumped pure spin current is converted back to a charge current due to ISHE (see Fig. 4-1(e)). Therefore, the initial charge current is modulated with the ISHE-generated charge current. The modulated charge current again generates a pure spin current due to SHE. Therefore, feedback is formed from each magnet to all others through a sequence of the spin pumping, ISHE, and SHE. By using the conventional feedback loop,[83,84,89,226] the

modulated spin current is not strong enough to cause any locking of the oscillations due to the small spin-Hall angle (θ_{SH}). To increase the locking strength, there is a need for amplification or accumulation of the modulated part of the charge current. Figure 4-1(f) demonstrates such a feedback loop implemented in the oscillator system. The components of the feedback are two bias tees that mix or decouple the dc and ac currents, a line which has a specific time delay τ, an amplifier with a gain G and maximum output current density of J_M , and a switch which is activated at a certain time (τ_{switch}) after the magnetization oscillation is initiated by the dc current. It is worth noting that similar feedback loops were utilized for generation of spin wave solitons.[227,228]

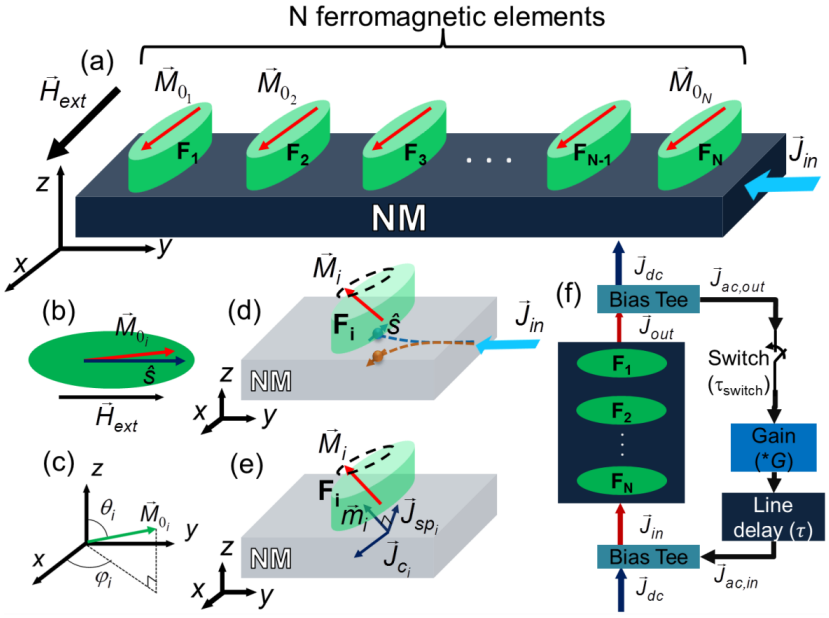

Figure 4-1. (a) The schematic diagram of the oscillator system. (b) The configuration of the initial magnetization, spin current polarization, and the external field for the i^{th} element. (c) The polar (θ_i) and azimuthal (φ_i) angles of the initial magnetization of the i^{th} element. (d) The schematic representation of SHE. (e) The schematic diagram of the spin pumping and ISHE. $\vec{m}_i$, $\vec{J}_{c_i}$, and $\vec{J}_{sp_i}$ form a right-handed coordinate. (f) The schematic of the complete oscillator system including the ac feedback line.

4.3 Theoretical model

The Landau-Lifshitz-Gilbert (LLG) equation including the Slonczewski spin-transfer term,[32] which governs the magnetization dynamics of each magnetic element, is

$$\frac{d\vec{m}_i}{dt} = -\gamma \vec{m}_i \times \vec{H}_{eff_i} + \alpha \vec{m}_i \times \frac{d\vec{m}_i}{dt} + \frac{\gamma \hbar \varepsilon}{\mu_0 e d M_s} J_{s_i} (\vec{m}_i \times \hat{s} \times \vec{m}_i) \qquad (4\text{-}1)$$

where $\vec{m}_i$ is the normalized magnetization vector ($\vec{M}_i / M_s$) of the i^{th} element, γ is the gyromagnetic ratio, $\vec{H}_{eff_i}$ is the effective field, α is the Gilbert damping constant, $\hbar$ is the reduced plank constant, ε is the efficiency of the spin transfer, μ_0 is the permeability of vacuum, e is the electron charge, d is the thickness of the magnetic element, M_s is the saturation magnetization, and J_{s_i} is the spin current injected into the i^{th} magnetic element and is polarized in the direction of $\hat{s}$. The effective field for the i^{th} element, $\vec{H}_{eff_i}$ can be written as $\vec{H}_{eff_i} = \vec{H}_{d_i} + \vec{H}_{ext} + \vec{H}_{an_i}$, where $\vec{H}_{d_i}$ is the demagnetizing field equal to $-M_s (\vec{m}_i \cdot \hat{z}) \hat{z}$, $\vec{H}_{ext}$ is the external field in the *x* direction, and $\vec{H}_{an_i}$ is the shape anisotropy field defined as $H_{an_i} (\vec{m}_i \cdot \hat{x}) \hat{x}$.

The spin current ($\vec{J}_{sp_i}$) which is pumped into the NM metal from magnetization dynamics of the i^{th} magnetic element can be defined as $\vec{J}_{sp_i} = \frac{\hbar}{8\pi} Re(2 g_{\uparrow\downarrow}) \left[\vec{m}_i \times \frac{d\vec{m}_i}{dt} \right]$, where $g_{\uparrow\downarrow}$ is the spin mixing conductance in the interface of the ferromagnetic material and the NM metal. The charge current generated in the NM metal from $\vec{J}_{sp_i}$ due to ISHE is defined as

$\vec{J}_{c_i} = -\frac{e}{\hbar}\theta_{SH}\left[\vec{J}_{sp_i} \times \vec{m}_i\right]$. The input current to the oscillator system, $\vec{J}_{in}$ at time t, can be defined as $\vec{J}_{in}(t) = -J_{dc}\,\hat{y} + \sum_{i=1}^{N}\sum_{n=1,2,...}\left(\vec{J}_{c_i}(t - n\tau)\cdot\hat{y}\right)\times G^n(1-L_{line})^n$, where J_{dc} is the amplitude of the dc charge current, and L_{line} is the line loss. Similarly, the output current of the oscillator system is $J_{out}(t) = \vec{J}_{in}(t) + \sum_{i=1}^{N}\vec{J}_{c_i}(t)\cdot\hat{y}$. The amplifier sets a limit for its maximum output current as J_M. Therefore, if the ac part of $\vec{J}_{out}$ satisfies $\left|\vec{J}_{ac,out}\right| > J_M$, $\vec{J}_{in}(\mathrm{t}) = -J_{dc}\hat{y} + J_M \times \frac{\vec{J}_{\mathrm{ac,out}}(\mathrm{t})}{\left|\vec{J}_{\mathrm{ac,out}}(\mathrm{t})\right|}$. The spin current ($J_{s_i}$) which is injected in each element and its polarization ($\hat{s}$) are derived considering the SHE of the charge current J_{out} as $J_{s_i}\hat{s} = \theta_{SH}\left[\vec{J}_{out}(t)\times\hat{z}\right]$.

A magnetic material with a saturation magnetization (M_s) of 7×10^5 A/m, Gilbert damping (α) of 0.007 (for permalloy[219], Most of the experiments for the spin-Hall oscillators have been based on Py as it has a relatively low saturation magnetization and damping, therefore it can be driven into oscillation with relatively small current densities in the pure spin current structures.), and gyromagnetic ratio $\gamma/2\pi$ of 3.5×10^4 Hz·(m/A) are assumed. The spin Hall angle (θ_{SH}) of the NM metal is assumed to be 0.07 (for Pt).[219] The spin mixing conductance ($g_{\uparrow\downarrow}$) is assumed to be $2.1\times10^{19}/\mathrm{m}^2$ as previously reported for the Py/Pt interface.[217] The thickness (d) of the magnetic layer is chosen as 5 nm. The initial magnetization of the magnetic elements are assumed to be $\theta_i = 75°$

and $\varphi_i = 5°$. To calculate the magnetization dynamics of each magnetic element Eq. (4-1) is solved using the Runge-Kutta numerical method.[229]

4.4 Numerical results and discussion

Figure 4-2 demonstrates an example of synchronization in frequency and phase using the proposed method. For this example, the number of the magnetic elements (N) is 10, τ is 5 ps, τ_{switch} is 10 ns, G is 1/(1-L_{line}), L_{line} is 0.1, the external magnetic field H_{ext} is 500 Oe, and the dc current J_{dc} is $(4\times10^{10})/\theta_{SH}$ A/m^2. The efficiency of the spin-transfer (ε) is assumed to be unity. To introduce different oscillation frequencies among the elements, shape anisotropy H_{an_i} is defined as $H_{an_i} = h_{an} + \left[h_{dev} \times (i-1)\right] / (N-1)$, where h_{an} and h_{dev} are the minimum value and the maximum deviation of shape anisotropy fields, respectively. For the case in Fig. 4-2, h_{an} is 50 Oe and h_{dev} is 15 Oe. Figure 4-2(a) shows the temporal variation of $\vec{m}_T$ and $\vec{m}_{T_{sync}}$ that are summations of the magnetization of all the elements ($\sum_{i=1}^{N} \vec{m}_i$), without (black curve) and with (red curve) applying ISHE-SHE interaction among the elements and the described feedback, respectively. The line-like collective trajectory of the red curve is the signature of synchronization. In addition, synchronization is clearly shown in Fig. 4-2(b) which depicts the fast Fourier transforms (FFT), $\left|\left(\sum_{\hat{e}_i=\hat{x},\hat{y},\hat{z}} FFT\left(\vec{m}_T \cdot \hat{e}_i\right)\right)\right|$ and $\left|\left(\sum_{\hat{e}_i=\hat{x},\hat{y},\hat{z}} FFT\left(\vec{m}_{T_{sync}} \cdot \hat{e}_i\right)\right)\right|$. A significant reduction of the linewidth (with the factor of ~1/N where N = 10) and increase in the

spectral density peak (with the factor of ~N) are achieved due to synchronization. Note that the power spectral density (PSD) peak scales with ~N^2 and its linewidth scales with ~$1/N^2$. Figure 4-2(c) shows the change in the ac part of J_{out} ($J_{ac,out}$ in Fig. 4-1(f)) for the synchronized case. Stabilizing of $J_{ac,out}$ is the consequence of the frequency and phase locking of the elements after 15 ns.

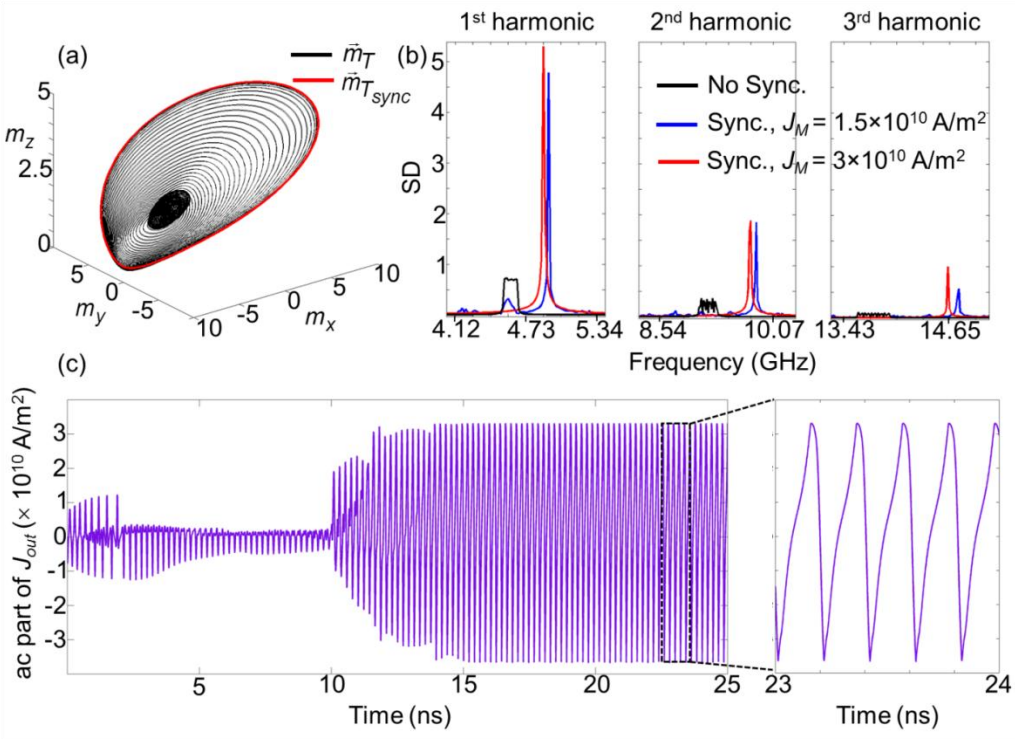

Figure 4-2. (a) The temporal variation of $\vec{m}_T$ (black curve) and $\vec{m}_{T_{sync}}$ (red curve). $m_{x,(y,z)}$ is the x,(y,z) component of $\vec{m}_T$ or $\vec{m}_{T_{sync}}$. (b) The spectral density (SD) of FFT of $\vec{m}_T$ and $\vec{m}_{T_{sync}}$. (c) The time variation of the ac part of J_{out}. H_{ext} = 500 Oe, h_{an} = 50 Oe, h_{dev} = 15 Oe, N = 10, J_{dc} = $(4\times10^{10})/\theta_{SH}$ A/m^2, and τ = 5 ps are used. J_M = 3×10^{10} A/m^2 for the red curves in (a) and (b) and the curve in (c), while J_M = 1.5×10^{10} A/m^2 for the blue curve in (b).

The switching delay of the ac feedback line, τ_{switch}, can affect the synchronization, since it determines the stage of the oscillation, in which the magnets begin to interact.[230] In all the modeling results, the feedback system after 10 ns (τ_{switch} = 10 ns) is included, which is well after all the oscillators have achieved their individual equilibrium precession. For in-plane magnetized films and in-plane polarized spin currents, in-plane (IP) and out-of-plane (OOP) precessions can be achieved.[231] Since the locking bandwidth for IP precession is very low in comparison with the OOP precession,[83,84] the analysis is confined to the OOP oscillation. For the fields used in Fig. 4-2, our calculations show that the OOP mode emerges for $J_{dc} > (3.9\times10^{10})/\theta_{SH}$ A/m^2. For a write/read head at the magnetic spacing of 5 nm from the magnetic media, for the media to be irradiated by a microwave field of 500 Oe, at least two of the nano-oscillators presented here should be locked and used in combination. Although the cases demonstrated in Chapter 2 are based on microwave field values of few hundred Oe, to reduce the dc field required, higher microwave amplitudes are needed, therefore locking of more oscillators is necessary for such applications in future. The ac current amplitude required for achieving the selectivity proposed in Chapter 3 is in the order of 10^{10} A/m^2. Such an ac current amplitude can be achieved only after synchronization of around 10 nano-oscillators of the kind considered here (see Fig. 4-2(c)).

The effect of the time delay (τ) of the feedback line has been an important attribute of the injection locking, as the magnetic oscillators are locked to their own oscillation with a time delay.[83,84] The injection of an ac current into an STO enforces its oscillation to have a phase difference of ~ $\pi/2$ with respect to the

injection.[87] Therefore, in the conventional feedback loop,[83,84,89,226] it is expected to achieve locking when τ is in the range of a quarter of the oscillation period of the magnets. For the case of the accumulative feedback loop (see Fig. 4-1(f)), the relation between the feedback signal phase and τ is different. As an example, I assume an oscillatory function containing three harmonics with typical amplitude ratios, $\mathrm{A(t)} = \sin(\omega t) + 0.3\sin(2\omega t) + 0.1\sin(3\omega t)$, with $\omega = 2\pi f$ where f = 6 GHz. Figure 4-3(c) shows the variation of the difference of the phase (φ_{diff}) between the feedback signal $B(\mathrm{t}) = \sum_{n=1}^{1000} A(\mathrm{t} - n\tau)$ and the original signal A(t) with respect to the variation of τ (red curve). The φ_{diff} for the accumulative delay is close to $\pi/2$ for values of τ = ~ 0, q/f (q = 1, 2, …), whereas for a single feedback (blue curve, $B(\mathrm{t}) = A(\mathrm{t} - \tau)$) φ_{diff} is close to $\pi/2$ for values of τ = ~ [q/f+1/(4f)] (q=0, 1, …). Figures 4-3(a) and (b) demonstrate the synchronization behavior with a variation of τ, where N = 3, J_{dc} = $(5\times10^{10})/\theta_{SH}$ A/m^2, and h_{dev} = 10 Oe. It can be seen that the synchronization is realized for 1 < τ < 12 ps ($\tau \approx 0$) and 156 < τ < 168 ps ($\tau \approx 1/f$), where $1/f \approx 159$ ps, in line with the above simple analytical model.

In Fig. 4-3(d), the nonlinearity coefficient $\nu = \dfrac{d\omega/dp}{d\Gamma_+/dp - d\Gamma_-/dp}$ for the dc currents corresponding to the OOP oscillation is calculated, where p is the oscillation power, Γ_+ is the damping torque, and Γ_- is the anti-damping torque.[232] For the currents leading to OOP precession, $|\nu|$ is high, therefore, the internal phase shift is $\varphi_{\mathrm{int}} = -\tan^{-1}(\nu) \approx \pi/2$. The shift in the frequency for

the locked cases in Fig. 4-3(a) can be described by utilizing the simple non-linear oscillator model, which results in $\omega_{sync} = \omega_0 + \Omega \sin\left(\varphi_{diff} - \varphi_{\text{int}}\right)$, where ω_{sync} is the synchronized frequency, ω_0 is the free running frequency of the oscillator, and Ω is the feedback strength.[89,232]

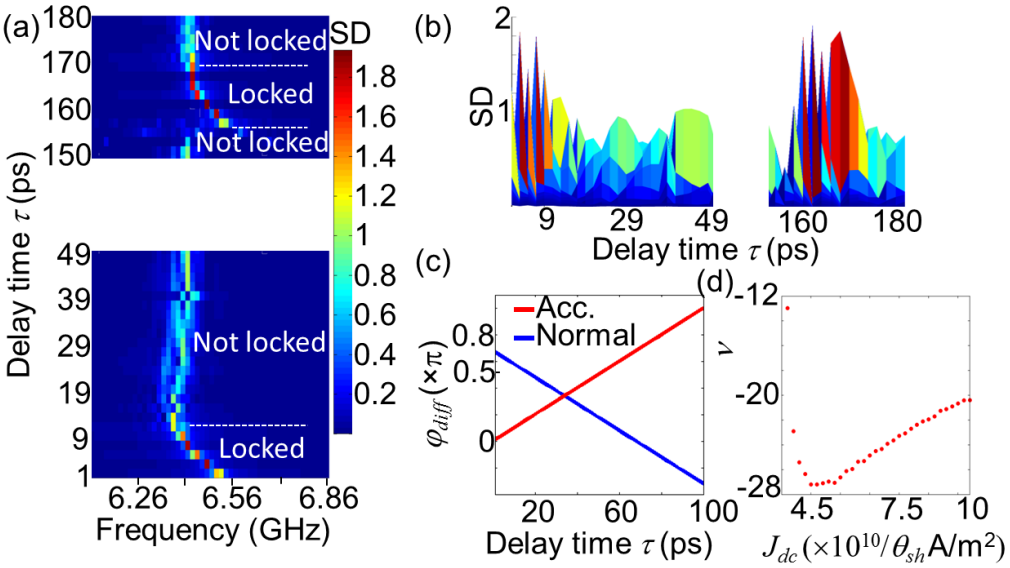

Figure 4-3. (a) Effect of τ variation on synchronization for H_{ext} = 500 Oe, h_{an} = 50 Oe, h_{dev} = 10 Oe, J_{dc} = $(5\times10^{10})/\theta_{SH}$ A/m^2, N = 3, and J_M = 1×10^{10} A/m^2. (b) Spectral density (SD) versus τ. (c) φ_{diff} versus τ for the normal feedback (blue curve) and the accumulative (Acc.) feedback (red curve). (d) Nonlinearity coefficient ν versus J_{dc}.

Relatively small values of J_M (maximum current density in the feedback line) may clip the input signal to the feedback loop ($J_{ac,out}$), and consequently there will be additional frequency components in the output of the feedback ($J_{ac,in}$). Therefore, sidebands of the main harmonics will appear in the oscillations. For example, additional frequency components appear in Fig. 4-2(b) in the case of J_M =1.5×10^{10} A/m^2 (blue curve) due to a relatively small

value of J_M. As N is higher, a larger J_M is required for the synchronization to be realized.

In order to study the relation of the dc current (J_{dc}) and the locking bandwidth (*BW*), h_{dev} is varied from 4 to 40 Oe for different currents leading to OOP precession with N = 3 and τ = 5 ps. Figure 4-4(a) shows the first harmonic of $\left|\left(\sum_{\hat{e}_i=\hat{x},\hat{y},\hat{z}} FFT\left(\left(\sum_{i=1}^{N}\vec{m}_i\right)\cdot\hat{e}_i\right)\right)\right|$ for various h_{dev} and J_{dc} combinations. It has been described in theoretical studies that for small oscillation powers, the maximum locking bandwidth is $\Omega\sqrt{1+\nu^2}$.[232] From the values of ν presented in Fig. 4-3(d), and relating it to the locking BW variation with respect to the current, a peak in the locking BW at $J_{dc} \approx 4.5\times10^{10}/\theta_{SH}$ A/m^2 is expected. However, from a complex behavior of locking BW in Fig. 4-4(a), it can be inferred that the feedback strength Ω has a fluctuating variation with respect to J_{dc}. The fluctuation is due to the variation of the mean oscillation angle and the oscillation trajectory with respect to the dc current, which, through spin pumping, ISHE, the accumulative feedback line, and SHE, cause fluctuation in the feedback strength.

Figure 4-4(b) shows the locking behavior with a higher $\theta_{SH} = 0.3$ reported for β-W[233] at $J_{dc} = 5\times10^{10}/\theta_{SH}$ A/m^2, assuming the same intermixing conductance ($g_{\uparrow\downarrow}$) as the Pt/Py bilayer for the β-W/Py bilayer. By comparing Fig. 4-4(b) with the corresponding J_{dc} case in Fig, 4-4(a), it is found that the locking BW as well as the locked frequency are increased due to a higher

amplitude of the feedback signal which is proportional to $\theta_{SH}{}^2$. Note that as the feedback signal increases, a higher J_M is required.

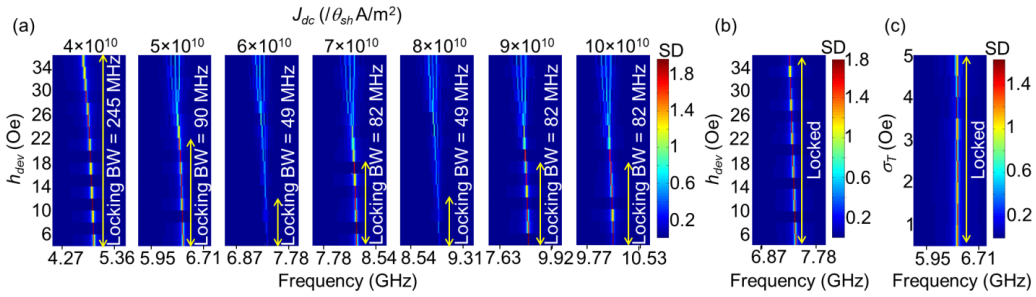

Figure 4-4. (a) Effect of the dc current (J_{dc}) on the maximum possible h_{dev} for synchronization (locking bandwidth (BW)). H_{ext} = 500 Oe, h_{an} = 50 Oe, N = 3, τ = 5 ps, and J_M = 1×10^{10} A/m^2 are used. (b) Locking dependence on h_{dev} for $\theta_{SH} = 0.3$ with J_{dc} = 5×10^{10}/θ_{SH} A/m^2 and J_M = 3×10^{10} A/m^2. (c) Locking possibility for different σ_T with $\theta_{SH} = 0.07$, J_{dc} = 5×10^{10}/θ_{SH} A/m^2, and J_M = 1×10^{10} A/m^2. SD is the normalized spectral density of the FFT of $\vec{m}_{T_{sync}}$.

A finite temperature will induce a random field with Gaussian distribution in both time and space with a strength of $\sigma^2 = 2\alpha kT / \gamma M_s V$, where k is the Boltzmann constant, T is the temperature, and V is the volume of the magnetic element.[5] Figure 4-4(c) shows the locking behavior by considering such a random field for different values of $\sigma_T = \sigma / \mu_0$. For elements with exemplary dimensions of 100 nm × 40 nm × 5 nm at T = 300 K, σ_T = 3.08 Oe. The Joule heating will increase the temperature T, resulting in a higher thermal noise; however, Fig. 4-4(c) shows that locking can be achieved for high thermal noise values (σ_T = 5 Oe corresponds to T = 786 K for the exemplary dimensions).

The fabrication of the proposed system requires the patterning of a narrow strip of a NM metal such as Pt or Ta, and ferromagnetic nano-magnets

such as NiFe or CoFeB. For an effective modulation of the current in NM and subsequent effective synchronization, the width of the magnetic elements should be the same as the width of the strip, and the thickness of the NM should be less than its spin diffusion length. This fabrication process is much simpler than that of MTJ-based STOs in series connection which has not been demonstrated experimentally. Moreover, the proposed method can be realized in a three-terminal configuration[50] by substituting the nano-magnets with nano-patterned MTJs with their free layers adjacent to the NM metal. In addition, the feedback loop implemented in this work can be utilized for the synchronization of spin-valve based STOs which generate a low charge current modulation.

4.5 Summary

In summary, a method to synchronize multiple nano-magnets in the frequency and phase using the spin pumping, inverse spin Hall, and spin Hall effects has been proposed. By adding an ac feedback line which imposes a certain delay time and gain, synchronization is realized for a wide range of applied dc currents. The synchronization is achieved for the feedback delay times close to 0 or integer multiples of the oscillation period. It offers a high power phase locked oscillation system with a narrow linewidth and its frequency can be controlled over a wide range. Our results would intrigue future experimental studies for the demonstration of the proposed system.

Chapter 5: All-optical magnetization reversal based on optically induced spin-dependent diffusive transport in the presence of spin-orbit interaction

5.1 Introduction

Optical manipulation of spins has been intensively studied for different applications. Coherent coupling of light with spin dynamics can be explained through relativistic quantum electrodynamics, and the effect is pronounced as a reservoir of angular momentum in spin manipulation of structures such as antiferromagnetic NiO or solid-state defects.[90-93] However, the effect of light on the spin dynamics is applicable not only to coherent couplings, but also optical spin-transfer torque, modification of crystalline anisotropy, and demagnetization.[94-112] The origin of the demagnetization itself has been subject to an ongoing debate in different structures.[97,98,100,103-107,109,113-117] The Elliot-Yafet mechanisms based on electron-phonon and electron-electron interactions, as well as magnonic dissipation and spin-dependent super-diffusive transport have been discussed to explain the ultra-fast demagnetization.

Incoherent all-optical manipulation of spin and magnetization reversal in ferrimagnets, anti-ferromagnets, and recently transition ferromagnets has been demonstrated in several experiments.[109,118-123] A magnetic field induced by circularly polarized light due to the inverse optical Faraday effect, non-local transfer of angular momentum via spin currents, two-magnon scattering,

demagnetization of different sites of the ferrimagnet (anti-ferromagnet), and exchange of the angular momentum between them due to different rates of magnetic moment change have been sought as the main contributors to all-optical switching (AOS) in such structures.[110,118,121,124-127]

Bulk and interface intrinsic and extrinsic spin-orbit interactions (SOI) have enabled the generation of pure spin currents to lead to spin-transfer torques in different structures such as multi-layers of ferromagnets and paramagnets, thin Rashba ferromagnets, impure ferromagnets and semi-conductors, structures with non-zero Berry curvature, etc.[34-49] Such spin currents and the torque exerted by them on the magnetization have been utilized in different configurations for switching or oscillation.[26,27,50-52] The intriguing observation of AOS in transition metal ferromagnets within specific structures containing paramagnets[119] has triggered a debate for the role of SOI in dynamics under short-pulse optical excitations.

In this chapter, the effect of different spin-orbit interactions under the influence of short-pulse optical excitation is discussed to investigate the possibility of magnetization reversal of an out-of-plane magnetized structure. In Chapter 5.2, the effect of different SOI mechanisms in the interested system is qualitatively studied. In Chapter 5.3, a numerical method to track the dynamics and distribution of the non-equilibrium diffusive transport of spin-polarized electrons is presented. Compared to previous works that used a similar numerical method to explain the demagnetization, our approach includes exchange mechanisms and SOI. SOI causes the generation of spin currents with transverse (with respect to the magnetization) spin polarization, resulting in non-collinear spin distribution at each event (space-time point), which makes the

inclusion of exchange interactions necessary. In Chapter 5.4, the numerical method is used to demonstrate how transient currents, spin-Hall effect, and skew scattering in combination with the super-diffusive transport can lead to magnetization reversal.

5.2 Spin-orbit interaction mechanisms under fs-laser excitation

The intrinsic role of SOI in demagnetization has been previously included in the models of Elliott-Yafet mechanisms considering the mixing of the spin states, and also in relativistic quantum thermodynamic for extracting the coherent response.[90,91,102,105,117] However, as the fs-laser excitation induces transient currents, the existence of different SOI mechanisms leads to transient spin currents and inversely generated charge currents.[94,96,97,103,106,107,111] The focus here is on structures with out-of-plane (OOP) magnetization, and the shining laser to be propagating in the OOP direction. Such a structure is a major candidate for ultrafast high-density magnetic storage. Figure 5-1(a) shows the schematic of a ferromagnet (FM)/non-magnet (NM) bilayer, and the laser spatial absorption pattern. The absorption of fs-laser excites the electrons below the Fermi level. The conduction of such electrons occurs with different velocities from that of the electrons in the Fermi level and might be spin-dependent.[234-236] In addition, the inhomogeneity of the light absorption induces the inhomogeneous carrier density in the conduction band that leads to diffusive charge currents (if the material is FM, the currents are spin-dependent). Since

the material is assumed to be magnetized in the *z* direction, the excited electrons initially carry spins parallel to the *z* direction.

In the absence of SOI mechanisms and magnetization chirality in the optically excited area and its neighboring region, the spin of the carriers remains parallel to the quantization axis, i.e. the *z* direction. It should be noted that the lack of transverse spin (spin polarization in the *xy* plane) means that even in the presence of high demagnetization and a magnetic field induced by an inverse optical Faraday effect due to ellipticity of light polarization, there will be no deterministic magnetization reversal (random magnetic domains with reversed magnetization may form).

I define the spatially varying tensor of $\left[\Gamma^{C\to S}\right]_{s\sigma' c\sigma}\left(r,\varphi,z\right)$, which relates the charge currents to spin currents with certain spin polarizations ($\left(r,\varphi,z\right)$ indicating the cylindrical coordination). I also define $\left[\Gamma^{S\to C}\right]_{c\sigma s\sigma'}\left(r,\varphi,z\right)$ which indicates the charge currents induced by spin currents. The subscripts *c*, *s*, and σ (σ') refer to the directions of the charge current, spin current and spin polarizations, respectively. I qualitatively discuss below the effect of different SOI mechanisms, and one would fill up the $\Gamma^{C\to S}$ and $\Gamma^{S\to C}$ tensors accordingly. The system symmetries (circular shape of the light spot and the perpendicular magnetization) imply that the net spin or charge accumulation in the $\hat{\varphi}$ direction will be zero. Therefore, the contribution of any SOI that leads to a spin current or charge current in the $\hat{\varphi}$ direction can be ignored, and the respective component in $\Gamma^{C\to S}$ or $\Gamma^{S\to C}$ can be set to zero.

The transient charge currents, parallel to the *z* direction with a *z*-polarized spin current in the *z* direction, do not induce any charge current ($\vec{S}\left(=S_z\hat{z}\right)\times\vec{J}^C\left(=J_z^C\hat{z}\right)=0$) due to inverse SOI mechanisms, such as the inverse spin-Hall effect (ISHE) or inverse Rashba interaction at the interface of the FM/NM[237], where $\vec{S}$ is the spin polarization vector and $\vec{J}^C$ is the charge current vector. In addition, the Rashba interaction ($J_z^C\hat{z}\times\vec{n}\left(=\hat{z}\right)=0$, where $\vec{n}$ is the normal to the interface) and the impurities (skew scattering in this case gives $S_z\hat{z}\times J_z^C\hat{z}=0$) do not scatter this charge current, and do not give rise to any net spin current. The only possible effect of $J_z^C\hat{z}$ with the spin polarization of $S_z\hat{z}$ is an in-plane spin-current (in the radial direction) that is induced due to the spin-Hall effect (SHE) in the bulk of the NM, where the polarization of this spin current will be in-plane and parallel to $\hat{\varphi}$, giving rise to an accumulation of in-plane spins (transverse spins) as shown in Fig. 5-1(b).

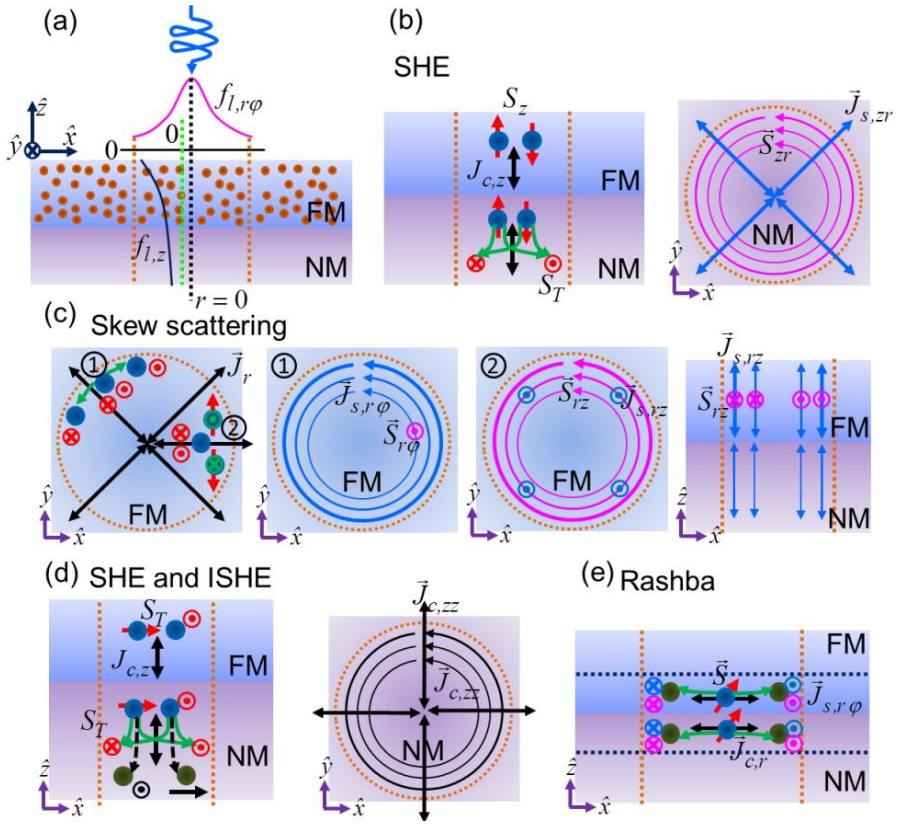

Figure 5-1. (a) The schematic of a FM/ NM bilayer and the laser spatial absorption pattern. The points in the FM are the impurities. (b) Top and side views of the in-plane spin-current (in the radial direction) with spin polarization along $\hat{\varphi}$, induced due to SHE in NM from $J_{c,z}\hat{z}$ with spin polarization of $S_z\hat{z}$. (c) Spin currents due to skew scattering of $J_{c,r}\hat{r}$ with spin polarization of $S_z\hat{z}$. Panels marked by numbers 1 and 2 refer to the two possible spin currents. The most right panel shows the side view of the spin current shown in panel 2. (d) ISHE-induced charge currents due to $J_{c,z}$ with transverse spin polarizations of S_r or S_z. (e) Spin current parallel to $\hat{\varphi}$ induced by $J_{c,r}$ due to the Rashba interaction at the FM/NM interface. The green (dashed black) arrows indicate direct (inverse) scattering. The black, red, blue, and pink arrows indicate charge current, spin polarization before scattering, spin current, and spin polarization after scattering, respectively. Dark blue (dark green) balls are non-scattered (scattered) electrons.

The in-plane transient charge currents flow in the radial direction $\vec{J}^C = J_r^C\hat{r}$, initially spin-polarized completely in the z direction $\vec{S} = S_z\hat{z}$ (see

Fig. 5-1(c)). If there are heavy metal impurities within the FM, the skew scattering will give rise to two different local spin currents. One of the spin currents will follow circular trajectories while being polarized in the *z* direction. The net spin-accumulation due to this spin-current will be zero because of the circular trajectory (see Fig. 5-1(c)). The other spin-current flows parallel to the *z* direction, while polarized in-plane and in the $\hat{\varphi}$ direction (see Fig. 5-1(c)). Due to this spin current, there will be a net transverse spin-accumulation towards the top surface and the interface between the FM and NM.

As discussed above, both the radial and OOP charge currents will acquire a transverse spin which are affected differently by SOI mechanisms. As can be seen in Fig. 5-1(d), the J_z^S ($\vec{J}^S$ is the spin current) with S_r or S_φ will give rise to ISHE-induced charge currents parallel to $\hat{\varphi}$ and $\hat{r}$, respectively. J_z^C with S_r or S_φ will induce a charge current parallel to $\hat{r}$ due to SHE in the NM. In addition, J_r^C with S_r or S_φ will go through the skew scattering in the FM and give rise to two different spin currents. One spin current will have the same in-plane spin-polarization and flow in the *z* direction. The other current will be polarized in the *z* direction, while flowing in circular trajectories inducing zero net spin-accumulation.

The Rashba interaction in the interface induces direct or inverse scatterings of the in-plane charge and spin currents. As can be seen in Fig. 5-1(e), J_r^C is scattered due to Rashba interaction and gives rise to a spin current parallel to $\hat{\varphi}$ with spin-polarization in the $\pm\hat{\varphi}$ direction. J_r^S with S_r induces a charge current parallel to $\hat{\varphi}$ due to the inverse Rashba interaction. Similarly,

J_{φ}^{S} with S_{φ} induces a charge current parallel to $\hat{r}$. As mentioned above, the assumptions on the symmetry of the system indicate that the net spin and charge accumulations in the $\hat{\varphi}$ direction are zero. Therefore, the net contribution of Rashba interaction at the interface is zero. However, depending on the shape of the light spot (e.g. elliptical, rectangular, etc.) and the magnetization direction (e.g. unidirectional in-plane), the Rashba contribution can be non-zero.

In summary, transverse spin accumulation in a FM/NM bilayer with a perpendicularly magnetized FM under optical excitation is possible, and its spatiotemporal profile is in mutual correlation with the transient charge currents through the skew-scattering, interface Rashba, and bulk SHE mechanisms. In addition, the demagnetization is affected, but negligibly (see Chapter 5.4), by the SOI mechanisms as the transient charge currents are modified by being scattered into spin currents with transverse spin polarization that go through different scattering types and rates.

5.3 Theoretical model

In order to demonstrate the possibility of optically-induced magnetization reversal, the study of spin dynamics in the system under consideration is divided into two consecutive approaches. First, the non-equilibrium spatiotemporal spin density distribution is calculated through a transport model. The output of this approach is the spatiotemporal profile of moment m_s (the spin polarization of the electrons below the Fermi energy E_f), as well as the density distribution of different spin components of the thermalized electrons at and above the Fermi

level, $\vec{S}_{neq}$. Second, the dynamics of the magnetization $\vec{m}$ is calculated by using the Landau–Lifshitz–Gilbert (LLG) equation. The torque exerted by $\vec{S}_{neq}$ on $\vec{m}$, denoted by T_m, is included in the LLG equation, and is non-zero if $\vec{m}$ and $\vec{S}_{neq}$ are non-collinear.

In order to determine the spatiotemporal distribution of $\vec{S}_{neq}$ and m_s, the transient spin-dependent transport of the electrons thermalized by the optical excitation in the presence of the SOI mechanisms is modeled. The carrier source terms, including the ones that are optically excited (Λ_{opt}) and the scattered part of the transported carriers (Λ_{sc}) (all the scatterings excluding SOI; SOI scatterings will be added separately in the diffusion equation) for all the possible energies and spin transport channels, are defined as,

$$\Lambda_{\alpha}\left(E,r,\varphi,z,t\right)=\Lambda_{opt,\alpha}\left(E,r,\varphi,z,t\right)+\Lambda_{sc,\alpha}\left(E,r,\varphi,z,t\right), \tag{5-1}$$

where α is the spin channel which can be r, φ, $z_{\uparrow}$, and $z_{\downarrow}$ (the spin-channel parallel to the quantization axis z is divided into up and down channels for convenience), whereas E is the indicator of the channel energy. In the rest of the formulations, $\left(E,r,\varphi,z,t\right)$ is dropped for simplicity, and if needed only the important parameters are mentioned.

In Eq. (5-1), $\Lambda_{opt,\alpha}=\Lambda_{qax,\alpha}+\Lambda_{acc,\alpha}\delta\left(E-\left(E_f+E_{ph}\right)\right)$, where $\Lambda_{qax,\alpha}=\Lambda_{las}\left(t\right)\Upsilon\left(\alpha,r,z\right)\left(\delta_{\alpha,z_{\uparrow}}+\delta_{\alpha,z_{\downarrow}}\right)$ indicates the electrons optically excited from the states below the Fermi level with a spin polarization parallel to the quantization axis. $\Lambda_{acc,\alpha}\left(E_f+E_{ph}\right)=\Lambda_{acc,\alpha}\left(E_f\right)\Lambda_{las}\left(t\right)\Upsilon\left(\alpha,r,z\right)$

indicates the electrons optically excited from the Fermi level (therefore the excited electrons in this term are at $E_f + E_{ph}$) which can have a non-collinear spin polarization with respect to the quantization axis due to the existence of the SOI mechanism. $\Lambda_{las}(t)$ is only a function of time which represents the power of the laser and is assumed to be Gaussian, whereas $\Upsilon(\alpha,r,z)$ represents the spatial functionality of the laser absorption. $\Upsilon(\alpha = z_{\uparrow},z) = n_{d,\uparrow}\, e^{-z/\lambda}\, f(r)$, $\Upsilon(\alpha = z_{\downarrow},z) = n_{d,\downarrow}\, e^{-z/\lambda}\, f(r)$, and $\Upsilon(\alpha = x(y),r,z) = f(r)e^{-z/\lambda}$, where $n_{d,\uparrow(\downarrow)}$ is the percentage of the up (down) spin excited above the Fermi level (E_f),[238] $f(r)$ is the radial laser absorption function, and λ is the absorption length. $\Lambda_{sc,\alpha}(E,r,\varphi,z,t) = \sum_{\alpha'}\sum_{E'} P(\alpha,\alpha',E,E',r,\varphi,z,t)\, n_{\alpha'}(E',r,\varphi,z,t)\,\Delta E$.

$P(\alpha,\alpha',E,E',r,\varphi,z,t)$ indicates the scattering rate from a state with an energy E', and spin channel α' into a state with an energy E and spin channel α. $n_{\alpha}(E,r,\varphi,z,t)$ and $\tau_{tot}(E,r,\varphi,z,t)$ are the carrier density and the total scattering rate of the spin channel α and energy E, respectively, at a specific time and space. It is worth noting that $1/\tau_{tot}(E',r,\varphi,z,t) = \sum_{\alpha}\sum_{E} P(\alpha,\alpha',E,E',r,\varphi,z,t)$.

The flux of carriers as a function of time and space, can be written as

$$\vec{\Phi}_{\alpha}(E,r,\varphi,z,t) = \int_0^{+\infty} dr' \int_0^{2\pi} d\varphi' \int_{-\infty}^{+\infty} dz' \int_{-\infty}^{t} \Lambda_{\alpha}(E,r',\varphi',z',t')\,\vec{\Xi}_{\alpha}(E,r,\varphi,z,t\,|\,E,r',\varphi',z',t')\,dt',$$

(5-2)

where $\vec{\Xi}_\alpha$ is the propagator based on Boltzmann formalism, and its derivation includes the spin and energy dependent elastic and inelastic scatterings, as well as velocities.[103,107] If we ignore the dependence on φ which is allowed due to the symmetries, the $\vec{\Xi}_\alpha$ derived in the literature for the case of infinite plane has been modified to account for the finite and meshed radial dimension. The propagator used to derive the flux of carriers $\vec{\Phi}_\alpha\left(E,r,\varphi,z,t\right)$ in Eq. (5-2) can be written for the three-dimensional case as

$$\vec{\Xi}_\alpha = \frac{\mathrm{Z}}{2\left(t-t'\right)^2} exp\left[-\left(t-t'\right)\left(\mathrm{T}\right)/\left(\mathrm{Z}\right)\right]\Theta\left(t-t'-|\mathrm{Z}|\right)\Theta\left(|\mathrm{Z}|/\left(t-t'\right)-\theta^-\right)\Theta\left(\theta^+-|\mathrm{Z}|/\left(t-t'\right)\right)$$
$$\left[cos\left(\left(\theta^+ + \theta^-\right)/2\right)\hat{z} + sin\left(\left(\theta^+ + \theta^-\right)/2\right)\hat{r}\right]$$

, where $\mathrm{Z} = \int_{z'}^{z} \frac{dz''}{v\left(z''\right)}$, $\mathrm{T} = \int_{z'}^{z} \frac{dz''}{\tau_{tot}\left(z''\right)v\left(z''\right)}$, $\theta^+ = arctan\left(\left|\frac{r-r'-\Delta r/2}{z-z'}\right|\right)$ and $\theta^- = arctan\left(\left|\frac{r-r'+\Delta r/2}{z-z'}\right|\right)$ (Δr is the radial mesh size).

$\vec{\Xi}_\alpha$ depends on the total scattering rate τ_{tot} which comprises several types of scattering, and can be written as

$$\frac{1}{\tau_{tot}} = \frac{1}{\tau_{d,in}} + \frac{1}{\tau_{d,el}} + \frac{1}{\tau_{sf}} + \frac{1}{\tau_{sd}} + \frac{1}{\tau_{ss}}, \tag{5-3}$$

where $\tau_{d,in}$ is the inelastic, $\tau_{d,el}$ is the elastic, and τ_{sf} is the spin-flip scattering. τ_{sd} indicates the exchange interaction between the bounded spin carriers (below E_f) and the non-equilibrium conduction carriers (at and above E_f), whereas τ_{ss} stands for the exchange interaction among the non-equilibrium conduction carriers.

At each point of time and space, the scattering rate from a state with an energy E', and spin channel α' into a state with an energy E and spin channel

α , is determined by $P(\alpha,\alpha',E,E',r,\varphi,z,t)$ which is related to different scattering mechanisms. The parts of P that are related to τ_{sd} and τ_{ss} can be written as $P_{sd}(\alpha,\alpha',E,E') = \frac{1}{\Delta_{sd}} \frac{m_\beta^2}{m_T^2} \varepsilon_{\alpha\beta\alpha'} \delta(E-E')$ and $P_{ss}(\alpha,\alpha',E,E') = \frac{1}{\Delta_{ss}} \frac{n_\beta^2}{n_T^2} \varepsilon_{\alpha\beta\alpha'} \delta(E-E')$. $\Delta_{sd(ss)}$ are the scattering rates of the two aforementioned exchange interactions. $m_T^2 = \sum_\alpha m_\alpha^2$ and $n_T^2 = \sum_\alpha n_\alpha^2$, where α sums over the spin channels, and m_α is the α -component of the magnetization. Based on $P_{sd(ss)}$, we can express $\tau_{sd(ss)}$ as $\frac{1}{\tau_{sd(ss)}} = \sum_{E'} \sum_{\alpha'} P_{sd(ss)}(\alpha',\alpha,E',E)$. Δ_{sd} depends on the magnetization of the carriers below E_f, $\frac{1}{\Delta_{sd}} \propto \left(n_{z_\uparrow} - n_{z_\downarrow}\right)_{E<E_f}$, and Δ_{ss} depends on the details of the density distribution of the different spin components of the conducting electrons. However, in our calculations, both of them are approximated to be constant values.

The part of P regarding the elastic and inelastic scattering is $P_{d,in} + P_{d,el} = \left[\delta_{\alpha,\alpha'} \frac{\Theta_{[E'-\Delta E_{max},E']}(E)}{\Delta E_{max}} + \chi \frac{\Theta_{[0,\Delta E_{max}]}(E)}{\Delta E_{max}} \right] \frac{1}{\tau_{d,in}} \left(1-\delta(E-E')\right) + \frac{1}{\tau_{d,el}} \delta_{\alpha,\alpha'} \delta(E-E')$,[103,107] where ΔE_{max} is the maximum of the energy scattering for the inelastic scattering, and $\Theta_{[\ldots]}$ is unity in the range indicated in brackets and zero otherwise. χ is defined to account for the excitation from E_f, which is a mixture of equilibrium electrons spin-polarized parallel to the quantization axis and non-equilibrium electrons polarized according to n_α . χ can be written as

$\chi = \left(Q \cdot C \cdot \frac{n_\alpha^2}{n_T^2} + Q \cdot (1-C) \cdot \frac{m_\alpha^2}{m_T^2} \right)$, where

$Q = 0.5\left(\delta_{\alpha,z_\uparrow} + \delta_{\alpha,z_\downarrow}\right) + \left(1 - \delta_{\alpha,z_\uparrow} - \delta_{\alpha,z_\downarrow}\right)$ and $0 \le C \le 1$. The parameter C accounts for the ratio of the electrons polarized transverse and parallel to the z axis. The value of C is a dynamic value with respect to time and depends on the density of states and the details of non-equilibrium spin of the thermalized electrons at the Fermi level. In the calculations, I use a small value of C = 0.01 not to overestimate the results for $S_{r,\varphi}$. Finally, the part of P regarding the spin-flip scattering can be written as $P_{sf} = \frac{1}{\tau_{sf}} \delta_{\alpha,\alpha'} \left(1 - \delta_{\alpha',z_\uparrow} - \delta_{\alpha',z_\downarrow}\right) + \frac{1}{\tau_{sf}} \left(1 - \delta_{\alpha,\alpha'}\right) \cdot \left(\delta_{\alpha',z_\uparrow} + \delta_{\alpha',z_\downarrow}\right)$.

The carrier density in each energy and spin channel is derived by solving the diffusion equation

$$\frac{\partial n_\alpha(E)}{\partial t} + \frac{n_\alpha(E)}{\tau_{tot}(E)} = \left(-\nabla \cdot \vec{\Phi}_\alpha(E) + \Lambda_\alpha(E) + \vartheta_\alpha(E) + \vartheta'_\alpha(E)\right), \quad (5\text{-}4)$$

where $\vartheta_\alpha(E)$ indicates the contribution of the SOI mechanisms, and can be defined based on the SOI induced currents discussed in Chapter 5.2, as $\vartheta_\alpha(E) = \left(\nabla \cdot \vec{J}^S\right) S_\alpha^{SC}$, where S_α^{SC} is the spin polarization of the scattered spin/charge current. We can write $\vec{J}^C = \vec{\Phi}_\alpha$ and use the tensors $\Gamma^{C \to S}$ and $\Gamma^{S \to C}$ to calculate $\vec{J}^S$ and $\vec{S}^{SC}$. To conserve the number of conducting carriers, I have included $\vartheta'_\alpha(E) = -\left(\nabla \cdot \vec{J}^S\right) \times \left\{ \sqrt{\left[\sum_{\alpha'} \left(S_{\alpha'}^{SC}\right)^2 \left(1 - \delta_{\alpha,\alpha'}\right) \right]} \right\} \times n_\alpha(E) / \left| n_\alpha(E) \right|$ in Eq. (5-4).

Knowing the spin density of the thermalized electrons above E_f (n_α) and below E_f ($n_{<E_f,z_{\uparrow(\downarrow)}}$) allows to determine the profile of m_s and $\vec{S}_{neq}$. Solving Eq. (5-4) provides n_α, and $n_{<E_f,z_{\uparrow(\downarrow)}}$ can be determined by

$$\frac{\partial n_{<E_f,z_\uparrow(z_\downarrow)}}{\partial t}=\left(-\int\Lambda_{qax,z_\uparrow(z_\downarrow)}(E)dE+\int\left[1-\sum_{\alpha'}\int P\left(\alpha',z_\uparrow(z_\downarrow),E',E\right)dE'\right]n_{z_\uparrow(z_\downarrow)}(E)dE\right)$$

.[103,107] Therefore, we can write

$$m_s=2\mu_B\left(n_{<E_f,z_\uparrow}-n_{<E_f,z_\downarrow}\right)+M_s,$$

$$\vec{S}_{neq}=2\mu_B\int\left[n_x\hat{x}+n_y\hat{y}+\left(n_{z_\uparrow}-n_{z_\downarrow}\right)\hat{z}\right]dE, \qquad (5\text{-}5)$$

where μ_B is the Bohr magneton, and M_s is the saturation magnetization of FM at room temperature. Since the torque on the non-equilibrium conduction spins are already included through the exchange terms in the scattering ($\tau_{sd(ss)}$), I calculate the torque on the bounded magnetization $\vec{m}=m_s\hat{z}$ separately. The torque on $\vec{m}$ can be written as $\vec{T}_m=-\frac{1}{\Delta_{sd}}\vec{m}\times\vec{S}_{neq}$. We can define the dynamic of $\vec{m}$ using the LLG equation $\frac{d\vec{m}}{dt}=\gamma\vec{m}\times\vec{H}+\vec{T}_m+\alpha\vec{m}\times\frac{d\vec{m}}{dt}$, where γ is the gyromagnetic ratio, α is the Gilbert damping constant, and $\vec{H}=\vec{H}_d+\vec{H}_{ex}+\vec{H}_{IF}+\vec{H}_{anis}+\vec{H}_{ext}$. $\vec{H}_d$ is the dipolar field, $\vec{H}_{ex}$ is the exchange field due to the possible non-collinear spatial functionality of $\vec{m}$ due to both isotropic and anisotropic Dzyaloshinskii-Moryia interaction (DMI)[239,240], $\vec{H}_{IF}$ is the field induced by the inverse optical Faraday effect due to ellipticity of optical excitation, $\vec{H}_{anis}$ is the anisotropy field, and $\vec{H}_{ext}$ is the external field.

5.4 Numerical results and discussions

I utilize the SOI mechanisms in Chapter 5.2 and the theoretical model of Chapter 5.3 in order to demonstrate the possibility of AOS in a magnetic system, which does not have any ferrimagnetic order and its FM layer has OOP crystalline anisotropy ($\vec{H}_{anis} = \frac{2K_u}{\mu_0 m_s}(\vec{m}\cdot\hat{z})\hat{z}$, where K_u is the anisotropy constant and μ_0 is the vacuum permeability). With assuming a circular symmetry of the system (circularly isotropic impurity distribution within the FM and circular shape of the light boundary) and zero DMI ($\vec{H}_{ex} = A\nabla^2\vec{m}$, where A is the isotropic exchange constant), we only need to consider the spin dynamics in the spatial variation in the radial and parallel to the z directions. In most of the experimental situations, the light spot radius (R_{las}) is much bigger than the thickness of the stack (d_{tot}). For reliable calculations we need the cell sizes in the z and r directions to be comparable (N_z (N_r) is the number of mesh cells in the z (radial) direction and $D_m = d_{tot} / N_z$ ($R_m = R_{las} / N_r$) is the respective mesh size). The experimental situation ($R_{las} \gg d_{tot}$) while keeping $D_m \sim R_m$ requires matrix sizes and calculation times that are beyond the limit of our numerical method. Therefore, I focus on R_{las} in the same order as d_{tot}. In addition, such a dimension is more relevant in the AOS application of high density magnetic storage. To simplify the calculations further, I approximate the τ_{tot} as a constant ($\frac{1}{\tau_{tot}} = \frac{1}{\tau_{d,in}} + \frac{1}{\tau_{d,el}} + \frac{1}{\tau_{sf}}$) while calculating $\vec{\Xi}_\alpha$.

For the inelastic scattering $\tau_{d,in}$ and carrier velocity $v_\alpha(E,z)$, I use the values of Fe for the FM layer, and use values of Pt for the NM layer.[235,236] I assume $\tau_{d,el} = 4/3\tau_{d,in}$, τ_{sf} to be 2000 fs and 20 fs for the FM and the NM (in the order of reported magnitudes for ferromagnets such as Co and Fe, and non-magnets such as Pt and W),[241] respectively. Δ_{sd} (Δ_{ss}) are assumed to be 1 fs (1 fs) for the FM and ∞ fs (1 fs) for the NM. $\Delta_{sd} = \hbar/\delta_{sd}$, where δ_{sd} is the exchange splitting and the reported value for Fe is around 2 eV,[242] making 1 fs a reasonable choice of Δ_{sd} for the calculations not to overestimate the results. The values for Δ_{ss} in FM and NM is chosen to account for the exchange interaction between the conduction electrons (based on the mean-field Weiss model), and at the same time not to overestimate the results for the transverse spin. The thicknesses of the FM and NM layers are assumed to be t_{FM} = 1.5 nm and t_{NM} = 2.5 nm, respectively. The other parameters are assumed to be $f(r) = exp\left(-2r^2/\left(aR_{las}\right)^2\right)\left(1-\Theta\left(r-R_{las}\right)\right)$ (Θ is a Heaviside function and a coefficient, a is assumed to be 2), $\Lambda_{las}(t) = P_{las}\,exp\left(-2\left(t-\varsigma/2\right)^2/\varsigma^2\right)\Theta(t)$ mW/m^2 (ς is the full width at half maximum of the Gaussian-shape laser pulse, and P_{las} is its peak of effectively absorbed power), ς = 50 fs, $E_{las} = \int_{-\infty}^{+\infty} P_{las}\,dt = 1$ mJ/m^2, Γ_{sh} = –0.3 is the spin-Hall angle of the NM (the values reported for Ta and W can be –0.3, the reported values for Pt are ~ 0.1)[27,223,243], Γ_{sk} = –0.1 is the skew scattering angle in the FM (a value as high as –0.24 is reported by skew scattering of Bi impurities in Cu which has

negligible intrinsic spin-Hall angle)[244], λ = 15 nm, $n_{d,\uparrow}$ = 0.5, $n_{d,\downarrow}$ = 0.5, $\vec{H}_{ext} = 0$, K_u = 10^6 J/m^3 (based on values reported for L_{10} FePt as well as multilayers such as Ta/CoFeB/MgO), γ = 2.2×10^5 m/(A·s), α = 0.1, R_{las} = 5 nm, N_z = 40, and N_r = 10. In the calculations I use the above parameters values unless otherwise specified. The direction of the inverse optical Faraday field is determined by the helicity of the optical excitation and can be assumed to be $\vec{B}_{IF} = -1\hat{z}$ T for a possible assistance of magnetization reversal (minus sign corresponds to a left-handed circularly polarized laser).[135] However, as this amplitude for $\vec{B}_{IF}$ contributes to the magnetization dynamics in a larger time scale (~ 1 ps) than the one due to spin-transfer torque (~ 10 fs) induced by the transverse spin accumulation, it can be set to zero (linear polarization of the optical excitation). This means that the reversal process presented here does not depend on the polarization of the shining light, however, it can be enhanced if $\vec{B}_{IF}$ is large enough and in the assisting direction (if switching from +z to –z, the sign of $\vec{B}_{IF}$ should be negative, in other words, left-handed circularly polarized laser for the present configuration).

I solve Eq. (5-4) self-consistently at $\varphi = \pi/2$ (corresponding to $\hat{r} = \hat{x}$ and $\hat{\varphi} = \hat{y}$). Figure 5-2(a) shows the spatial average (over $0 < r < R_{las}$ and $t_{NM} < z \le d_{tot}$) of the temporal evolution of $\vec{S}_{neq}$ and the change of m_s in the FM layer ($\vec{S}_{avg}$ and Δm_z, respectively) for up to 160 fs. The demagnetization (reduction of m_s) and the presence of transverse spins ($\vec{S}_{neq} \cdot (\hat{r} + \hat{\varphi}) \neq 0$) are evident from Fig. 5-2(a). Figures 5-2(b-d) show the radial average (over

$0 < r < R_{las}$) of the spatial distribution of $\vec{S}_{neq}$ in the $\hat{r}$, $\hat{\varphi}$, and $\hat{z}$ directions. It should be noted that the irregular oscillations in the z direction of some spatiotemporal regions in Figs. 5-2(b-e) are due to finite space and time mesh dimensions. However, I have checked that for the system under consideration, the mesh sizes used here give reliable results and main behaviors of the signals are captured properly (the artifact oscillations are averaged to negligible values). The non-equilibrium spin texture formed in the NM is originated mainly in the radial *rz*-variant SHE-induced spin currents which also diffuse along the *z* and *r* directions (going through reflections from the bottom boundary and diffusion into the FM). The spin texture in the FM layer is further affected by the OOP *rz*-variant skew-induced spin currents which also diffuse along the *z* and *r* directions (going through reflections from the top boundary and diffusion into the NM). In addition, the exchange interactions (τ_{sd} and τ_{ss}) are responsible for the correlation between the three coordinates of the non-equilibrium spins.

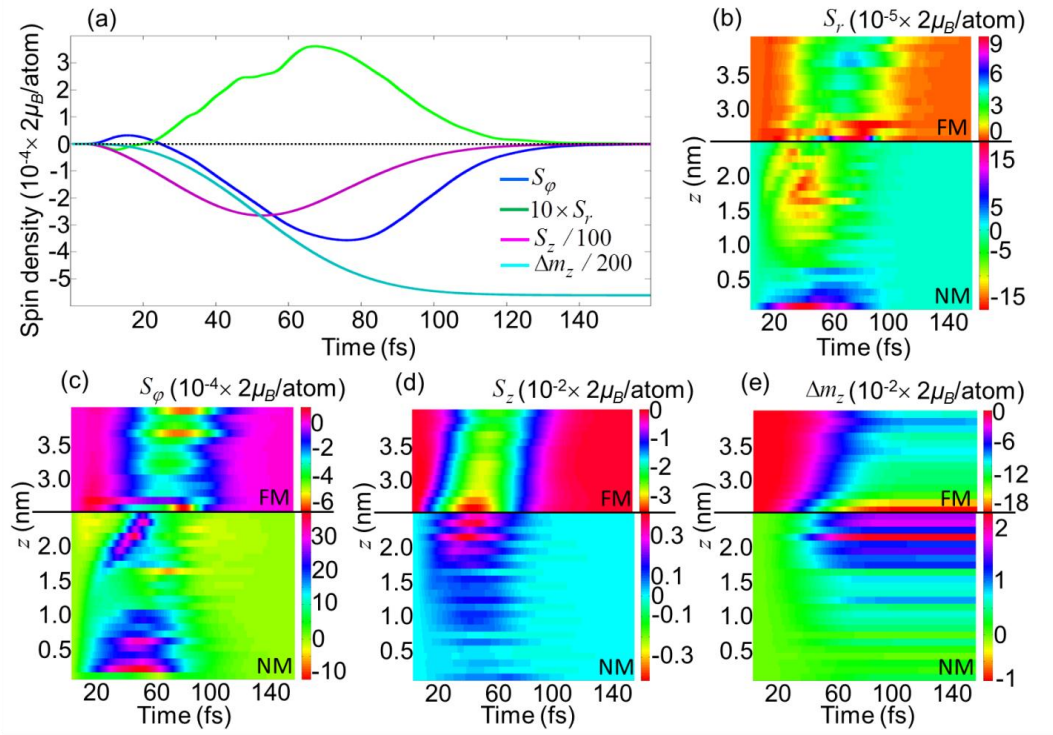

Figure 5-2. (a) Spatial average (average over $0 < r < R_{las}$ and $t_{NM} \le z < d_{tot}$) of the temporal evolution of $\vec{S}_{neq}$ and the change in m_s in the FM layer ($\vec{S}_{avg}$ and Δm_z, respectively) up to 160 fs. (b-d) The radial average (average over $0 < r < R_{las}$) of the spatiotemporal distribution of $\vec{S}_{neq}$ in the $\hat{r}$, $\hat{\varphi}$ and $\hat{z}$ directions, respectively. (e) The radial average of the spatiotemporal distribution of the change in m_s, Δm_z.

The dip of S_z in Fig. 5-2(a) at ~ 50 fs is the direct effect of the optical excitation in FM and diffusion of electrons into the NM which are initially spin-polarized along the magnetization (see also Fig. 5-2(d)). The velocities and scattering rates are different for spin-up and spin-down, resulting in different diffusion rates, which leads to a non-zero temporal profile of S_z in FM. The *sd* exchange interaction which turns the transverse-spins along the magnetization (*z* direction), affects S_z, however the effect is negligible due to $\left|\vec{S}_{neq} \cdot (\hat{r} + \hat{\varphi})\right| \ll S_z$

(see also Fig. 5-3(b)). The decay in all the components of non-equilibrium spins is expected as the transient charge and spin currents equilibrate. The demagnetization (Δm_z) becomes saturated as long as another temperature bath (e.g. lattice) is not included (see Fig. 5-2(a)). I focus on the transient currents in the presented time scale, where other temperature bathes can be neglected. Figure 5-2(e) shows the radial average of the spatial distribution of Δm_z. The demagnetization process is similar to the results from the models excluding the SOI mechanisms, where the spin-up and spin-down optically excited electrons diffuse with different velocities and scattering rates into the adjacent NM, causing the demagnetization.[8,14] Here, we have non-zero $\vec{S}_{neq} \cdot (\hat{r} + \hat{\varphi})$, but $\left|\vec{S}_{neq} \cdot (\hat{r} + \hat{\varphi})\right| \ll S_z$, therefore we expect similar demagnetization process.[97,103]

In Figs. 5-3(a-e) I present the effect of different parameters of the system on the temporal evolution of $\vec{S}_{neq}$ and Δm_z. Figure 5-3(a) shows the dynamics of $\vec{S}_{neq}$ for three different thicknesses of the NM (2.5 nm (case 1), 2.0 nm (case 2), and 3.0 nm (case 3)). With increasing t_{NM} the demagnetization increases (till it saturates) as the diffused electrons from FM into NM flow back less into FM. In addition, by increasing t_{NM} the amount of spin accumulation due to SHE increases, and consequently its diffusion into the FM leads to an increase in the amplitude of S_φ. Figure 5-3(b) shows the spin dynamics for three different strengths of the exchange interactions (Δ_{sd} (Δ_{ss}) = 1 (similar to case 1), 2, and 5 fs). Higher values of Δ_{sd} (Δ_{ss}) mean less scattering of $\left(\vec{S}_{neq} \cdot (\hat{r} + \hat{\varphi})\right)$ into S_z or m_z, resulting in higher amplitudes of S_φ. However, as $\left|\vec{S}_{neq} \cdot (\hat{r} + \hat{\varphi})\right| \ll S_z$,

change in demagnetization and S_z should be negligible as can be also seen in Fig. 5-3(b). Figure 5-3(c) shows the spin dynamics for four different cases of skew scattering (Γ_{sk} = -0.3 (case 4), -0.1 (similar to case 1), 0 (case 5), and 0.3 (case 6)). The effect of skew scattering dominates the initial stages of the spin dynamics where the SHE induced spins have not diffused into the FM yet. Therefore, the effect of the changes in the value and sign of Γ_{sk} is pronounced in the initial stages of the $\vec{S}_{neq} \cdot (\hat{r} + \hat{\varphi})$ (see S_{φ} in Fig. 5-3(c)). Again, the effect of Γ_{sk} value and sign on Δm_z and S_z is negligible as $\left|\vec{S}_{neq} \cdot (\hat{r} + \hat{\varphi})\right| \ll S_z$.

Figure 5-3(d) shows the spin dynamics for three different cases of the $f(r)$ lineshape coefficient a (a = 1 (case 7), 2 (similar to case 1), 4 (case 8)). The smaller a indicates higher concentration of light in the center, leading to an increase of spin accumulation due to the skew scattering and the SHE in NM at earlier times. The larger a is, the higher light absorption becomes and the higher amplitude signals have. It should be noted that the amplitude of the signals can be tuned by changing the laser power, while the lineshapes and the relative values of signal components remain unchanged (as long as a conduction channel is not saturated at higher laser powers). Figure 5-3(e) shows the spin dynamics for three different values of absorption length (λ = 5 (case 9), 15 (similar to case 1), and 25 nm (case 10)). For smaller λ, the absorption of light is steeper in the z direction leading to higher diffusive currents, which consequently results in higher diffused SHE-induced spin-accumulation into FM at later times. It can also be noticed that for smaller values of λ, the amplitude of S_z increases while the demagnetization decreases.

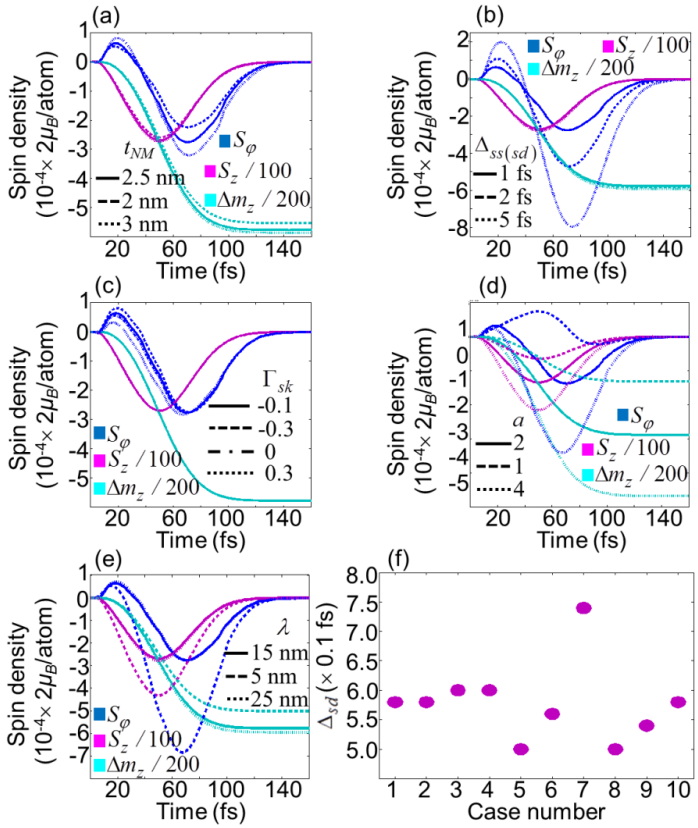

Figure 5-3. (a) S_φ, S_z and Δm_z for t_{NM} = 2.5 nm (continuous line, case 1), 2 nm (dashed line, case 2), and 3 nm (dotted line, case 3). (b) S_φ, S_z and Δm_z for Δ_{sd} (Δ_{ss}) = 1 fs (continuous line), 2 fs (dashed line), and 5 fs (dotted line). (c) S_φ, S_z and Δm_z for $\Gamma_{sk} = -0.3$ (dashed line, case 4), $\Gamma_{sk} = -0.1$ (continuous line), $\Gamma_{sk} = 0$ (dash-dotted line, case 5), and $\Gamma_{sk} = 0.3$ (dotted line, case 6). (d) S_φ, S_z and Δm_z for $a = 1$ (dashed line, case 7), $a = 2$ (continuous line), and $a = 4$ (dotted line, case 8). (e) S_φ, S_z and Δm_z for $\lambda = 5$ nm (dashed line, case 9), $\lambda = 15$ nm (continuous line), and $\lambda = 25$ nm (dotted line, case 10). For (a-e), t_{FM} = 1 nm, N_r = 5, and the continuous line represents a similar case (t_{NM} = 2.5 nm, Δ_{sd} (Δ_{ss}) = 1 fs, $\Gamma_{sk} = -0.1$, $a = 2$, and $\lambda = 15$ nm). (f) The value of Δ_{sd} that the magnetization reversal becomes possible while we keep $M_s + min(\Delta m_z) = 0.1$ μ_B/atom, for the cases 1 to 10 (the error bar for Δ_{sd} is ±0.01 fs and dot sizes reflect this error bar).

For the cases 1 to 10 presented in Figs. 5-3(a) and 5-3(c-e), I explore the possibility of magnetization reversal by solving the LLG dynamics of the magnetization $\vec{m}_{avg}$, while assuming that $\vec{S}_{neq}$ (see Eq. (5-5)) keeps its coordination throughout the time. To be consistent, I assume a laser energy that causes $min(m_s) = M_s + min(\Delta m_z) = 0.1$ μ_B/atom (the saturation magnetization of FM, M_s is assumed to be 0.65 μ_B/atom) for each of the cases 1 to 10, and then I vary Δ_{sd} to find its upper threshold for achieving magnetization reversal (see Fig. 5-3(f)). The existence of non-equilibrium transvers spin (S_r and S_φ) without longitudinal one (S_z) brings the magnetization towards in-plane but does not switch it. Therefore, both the amplitude ratio of S_φ to S_z (it should be noted that the amplitudes can be scaled by laser power, therefore only ratios and relative profiles are important), and overlap details of their temporal lineshapes are important to determine the reversal possibility for a particular Δ_{sd}. The possibility of reversal for all the considered cases at a reasonable value of Δ_{sd}, and few other important points can be inferred from Fig. 5-3(f) as follows. The presence, sign, and amplitude of skew scattering (with respect to the spin-Hall angle) can modulate the reversal possibility considerably (cases 1, 4, 5, and 6, see also Fig. 5-3(c)), due to the modulations it causes in the initial temporal stages of S_φ and the overlap of S_φ lineshape with S_z, which in turn determine the rate of reversal. From cases 1, 7, and 8, it can be inferred that the smaller the $f(r)$ lineshape coefficient a is (a lower value of a means a higher concentration of light in the center), the easier the magnetization reversal is. In the overlap

region of S_φ and S_z lineshapes, the relative amplitude of S_φ with respect to S_z is higher for the case 7 (a = 1) with respect to cases 1 (a = 2) and 8 (a = 4) (see Fig. 5-3(d)). Similar discussion is applicable for the effect of λ, where the cases 9 and 10 in Fig. 5-3(f) indicate an easier reversal for a larger λ. For a smaller λ, the absorption of light will be steeper in the z direction, resulting in higher spin-accumulation due to SHE in later times (where S_z is suppressed), which makes the magnetization remain in-plane up to smaller values of Δ_{sd}. In conclusion, by manipulating the SOI strengths and transient currents (determined by material structures as well as laser power and its spatiotemporal pattern), the non-equilibrium signal shape can be modified in order to manipulate the magnetization reversal for AOS applications.

As Figs. 5-3(d) and 5-3(f) suggest, the $f(r)$ lineshape coefficient a modifies the signals ($\vec{S}_{neq}$ and Δm_z) and the reversal possibility (compare the cases 1 and 7) more significantly than the other parameters. Figure 5-4(a) shows that amplitude of S_φ is enhanced at the earlier stage (0 < t < 40 fs) by decreasing a, and $|S_\varphi / S_z|$ increases. Consequently, the reversal possibility in Fig. 5-4(b) generally increases with decreasing a. Figures 5-4(c,d) and 5-4(e,f) show the spatiotemporal distribution of $\vec{S}_{neq}$ in the $\hat{\varphi}$ direction in the NM ($a = 1$ and 2) and FM ($a = 1$ and 2), respectively. For smaller a, the positive S_φ spin accumulation in NM shifts towards the center of the laser spot (see Fig. 5-4(c,d)), which results in more diffusion of positive S_φ from NM into FM at the

earlier stage (see Fig. 5-4(e,f)), leading the profile of S_{φ} to be more positive in FM.

After a fs laser pulse excitation, lattice temperature does not play a significant role until few hundreds of femtosecond, and spin and electron temperatures will dominate that time scale. However, the lattice contributes to the demagnetization process through the electron-phonon based Eliot-Yafet mechanism. This is an ongoing debate about whether superdiffusive current or Eliot-Yafet dominates demagnetization, and our focus in this work is the case of dominance of superdiffusive currents in the demagnetization process.

The model presented here is not able to capture the Eliot-Yafet based demagnetization. However, the reversal mechanism discussed here can occur even if the Eliot-Yafet mechanism dominates the super-diffusive contribution to the demagnetization. Since Eliot-Yafet spin-flips are mediated by excitation of a phonon or magnon, diffusion and accumulation of these two at the interface with NM will induce pure spin-currents in the NM and respective charge currents due to ISHE. For similar system symmetries, there will not be a transverse spin accumulation. However, for the elliptical light shape, there will be transverse spin in the second order of the spin-Hall angle. This transverse spin diffuses into the FM and induces spin-transfer torque on its magnetization. Overall, for the system studied here, if the super-diffusive picture dominates the demagnetization, the reversal is expected to be more feasible.

In this work, we used the LLG equation to determine if the reversal is possible or not. The LLG equation is based on the assumption that the magnetization amplitude is constant (magnetization in the context of averaging

over atoms of a particular ensemble). To tackle this issue, solving LLG atomistically in interaction with neighboring atoms and inclusion of the Langevin field (proportional to temperature) at finite temperature has been proposed. Another approach is to begin from the Landau-Lifshitz equation for a single magnetic atom, and derive the Landau-Lifshitz-Bloch (LLB) equation as $\frac{d\vec{m}}{dt} = \gamma\vec{m}\times\vec{H}_{eff} + \alpha_{\perp}\vec{m}\times\left(\vec{m}\times\vec{H}_{eff}\right) - \alpha_{\parallel}\left(\vec{m}\cdot\vec{H}_{eff}\right)\vec{m}$, where $\vec{H}_{eff}$ is temperature-dependent and includes the Langevin field and both $\alpha_{\parallel}$ and $\alpha_{\perp}$ depend on the Langevin field and are proportional to T/T_C and $(1\text{-}T/3T_c)$, respectively (T is the lattice temperature and T_C is the mean-field Curie temperature).[109] Both the LLB equation and atomistic LLG+Langevin can result in demagnetization in a micromagnetic approach. However, our use of the LLG equation is reasonable as the demagnetization has been calculated separately based on the super-diffusive transport, therefore the last term of the LLB equation can be ignored. The remaining terms of the LLB equation is equal to the LLG equation without spin-transfer torque. Since for T well below T_C which is expected for first tens of femtosecond, $\alpha_{\perp}$ can be approximated constant and the Langevin field is not comparable to the spin-transfer torque, the LLB equation can be approximated by the LLG equation used in our study.

Although the above calculations are based on several approximations, the results indicate the possibility of magnetization reversal through the coexistence of optically excited transport and different SOI mechanisms. In order to achieve a more accurate model, the Elliott-Yafet mechanisms should be included, the dependence of $\vec{\Xi}_{\alpha}$ in time and all the three dimensions should be

considered, the coefficients regarding the SOI mechanisms as well as Δ_{sd}, and Δ_{ss} should be derived through first-principle calculations, and the magnetization dynamics should be solved micromagnetically. In addition, Monte Carlo methods can be implemented to perform calculations for larger systems.

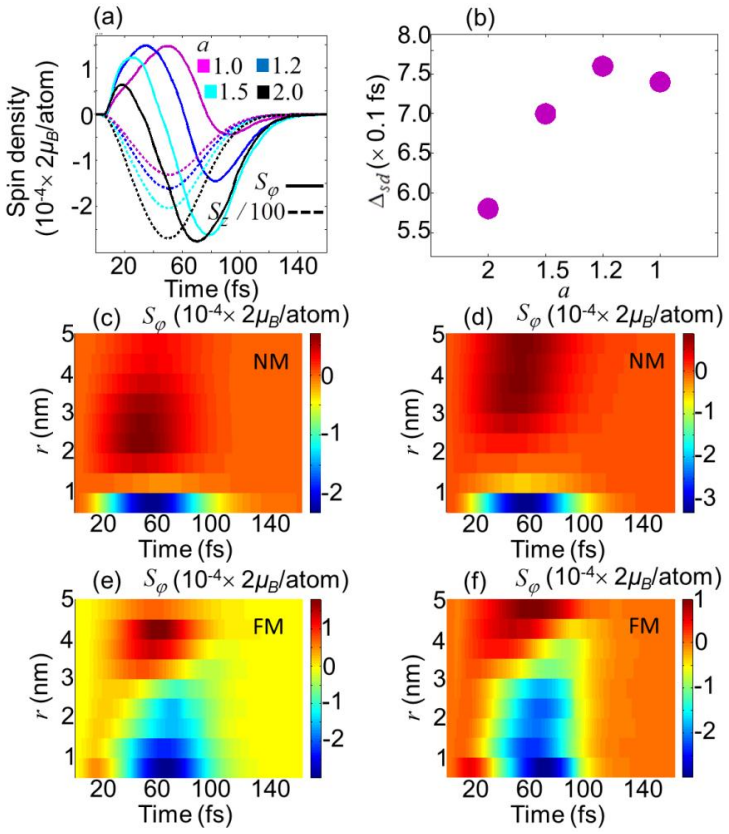

Figure 5-4. (a) S_φ and S_z for $a=1$, 1.2, 1.5, and 2. (b) The value of Δ_{sd} that the magnetization reversal becomes possible while we keep $M_s + min(\Delta m_z) = 0.1$ μ_B/atom, for the cases in (a) (the error bar for Δ_{sd} is ±0.01 fs and dot sizes reflect the error bar). (c-d) The spatiotemporal distribution of $\vec{S}_{neq}$ in the $\hat{\varphi}$ direction in the NM (averaged over $0 < z \le d_{NM}$) for $a=1$ and $a=2$, respectively. (e-f) The spatiotemporal distribution of $\vec{S}_{neq}$ in the $\hat{\varphi}$ direction in the FM (average over $d_{NM} < z < d_{tot}$) for $a=1$ and $a=2$, respectively.

5.5 Summary

The effect of SOI mechanisms under the fs optical excitation has been discussed. In perpendicularly magnetized ferromagnetic thin films adjacent to a non-magnetic heavy metal layer, the skew scattering and spin-Hall effect give rise to the generation of transverse spins, which in turn exerts torques on the magnetization. Such torques can cause deterministic magnetization reversal, enabling all-optical switching in ferromagnetic transition metals. In order to optimize the structure for such a reversal mechanism, the impurity type, the bulk of the heavy metal, and the Rashba coefficient at the interface should be designed so as to have their effects superimpose constructively. In addition, the shape of the light spot and the light absorption coefficients, which determine the transient charge currents, should be optimized in order to facilitate the magnetization reversal process.

Chapter 6: Transformation magnonics with focus on cloaking spin waves

6.1 Introduction

Invisibility cloaking of different types of waves have been pursued intensively in the last decade.[245-257] Different mechanisms for decreasing the scattering of objects with electromagnetic (EM) waves have been proposed and investigated.[245,247,250,251,257] Amongst those, the space transformation method intuitively provides a promising avenue to achieve the invisibility by designing a particular shell to hide the core. The Maxwell's equations are invariant under such a space transformation, leading to materials in the shell region being inhomogeneous and anisotropic.[250,255] This method or its simplified approximation has been demonstrated theoretically and experimentally for microwave EM waves by using EM metamaterials.[247,250,255-257] It has also been revealed that the 2D Schrodinger equation can be invariant under space transformation by using inhomogeneous and anisotropic effective mass and magnetic potential in the shell area.[253] Although it has been suggested that the perfect invariance for general three-dimensional elastodynamic waves is not possible,[249,258] the transformation based cloaking of such waves has been demonstrated for special cases. It has been also proven that the acoustic wave equations remain invariant in 2D and 3D by having a specific inhomogeneity and anisotropy in the mass density and the bulk moduli.[252,259,260] Recently, there have been demonstrations of bilayer cloaks for temperature, dc current, and

magnetostatic fields by utilizing bulk homogenous materials.[248,254,261-263] The conception of invisibility is not always reducing the wave scattering. It can be also referred to as hiding a feature of an object or space. As an example, it was proposed that in bilayer graphene, the confined states in the barrier can be cloaked due to chirality mismatch with the continuum states, for the normal and oblique incident currents.[264] Another example is cloaking polarizable discrete systems using an anomalous resonance technique.[251]

Another important type of wave that has been the subject studied for decades, is spin wave with magnon as its quanta.[137] The feature that makes spin waves interesting for applications is their wave-vectors as small as few nanometers and frequencies of tens of GHz. As it is possible to engineer different dispersions in magnetic lattices, the magnonics has thereby attracted a lot of attention as a promising candidate with low energy consumption and high throughput computation, which may possibly go beyond photonic or even electron devices. There have been many theoretical and experimental demonstrations of different types of passive and active magnonic systems and crystals, such as transistors, interferometers, waveguides, and logic gates.[137-140] In addition, due to the high nonlinearity in magnetization dynamics, spin waves have become a base for studying different phenomena such as time reversal and Bose condensation of magnons as Bosonic waves.[141,142]

As the transformation optics enabled new possibilities in photonics, the transformation magnonics can introduce new approaches in magnonics. Despite that a negative refraction index for spin waves[265] has been reported, there has not been a unified account of transformation magnonics for more sophisticated applications such as magnonic invisibility cloaks. As an alternative to the

transformation techniques for controlling waves, recent proposals and demonstrations of topologically protected edge modes for photons, phonons, and magnons can be utilized to cloak the defects in the edges.[266-269]

In this chapter, the invariance in the governing equations of the magnetization dynamics under the space transformation is investigated. The objective is to reduce the scattering of a non-magnetic core (blocking the magnons) by designing the magnetic characteristics in a surrounding shell, such as the magnetic moment, gyromagnetic factor, exchange constant, Gilbert damping, and external magnetic field. The spatial profiles of these parameters in the shell area can be designed such that the magnetization dynamics is rendered maximally invariant under the space transformation. The similar approach proposed here for making the magnetization dynamic invariant under space transformation can be used for other purposes other than cloaking an object, like concentrating spin waves that can be utilized in future for magnetization reversal (see Chapter 6.5)

6.2 Cloaking shell designs based on transformation magnonics

6.2.1 Governing equations of the magnons and possible cloaking approaches

The Landau-Lifshitz-Gilbert (LLG) equation governs the magnetization dynamics. The total magnetization $\vec{M}(\vec{\rho})$ can be written as

$\vec{M}(\vec{\rho}) = \vec{M}_0(\vec{\rho}) + \vec{M}_d(\vec{\rho})$, where $\vec{\rho}$ is the coordination vector, $\vec{M}_0(\vec{\rho})$ is the static part of the magnetization, and $\vec{M}_d(\vec{\rho})$ is the dynamic part of the magnetization. For media with isotropic magnetic moments, under the assumption of zero temperature, $\left|\vec{M}(\vec{\rho})\right|$ is temporally constant, implying $\vec{M}_0(\vec{\rho}) \cdot \vec{M}_d(\vec{\rho}) = 0$. More generally to account for possible anisotropy in the moment, we can write $\vec{M}(\vec{\rho}) = \bar{M}_s(\vec{\rho})\left(\vec{m}_0(\vec{\rho}) + \vec{m}_d(\vec{\rho})\right)$, where $\bar{M}_s(\vec{\rho})$ is defined as the moment tensor. $\vec{m}_0(\vec{\rho})$ and $\vec{m}_d(\vec{\rho})$ are the mathematical vectors [$\vec{m}_0(\vec{\rho}) + \vec{m}_d(\vec{\rho})$ is a unit vector] that determine the static ($\vec{M}_0(\vec{\rho})$) and dynamic ($\vec{M}_d(\vec{\rho})$) part of the magnetization, respectively, based on $\bar{M}_s(\vec{\rho})$ ($\vec{M}_0(\vec{\rho}) = \bar{M}_s(\vec{\rho})\vec{m}_0(\vec{\rho})$ and $\vec{M}_d(\vec{\rho}) = \bar{M}_s(\vec{\rho})\vec{m}_d(\vec{\rho})$). If the moment is isotropic ($\bar{M}_s(\vec{\rho})$ has equivalent diagonal and zero off-diagonal components) at position $\vec{\rho}$, $\vec{M}_0(\vec{\rho})$ ($\vec{M}_d(\vec{\rho})$) is parallel to $\vec{m}_0(\vec{\rho})$ ($\vec{m}_d(\vec{\rho})$), while in the case of anisotropic moment (e.g. if $\bar{M}_s(\vec{\rho})$ has non-equivalent non-zero diagonal and zero off-diagonal components), $\vec{M}_0(\vec{\rho})$ ($\vec{M}_d(\vec{\rho})$) is not necessarily parallel to $\vec{m}_0(\vec{\rho})$ ($\vec{m}_d(\vec{\rho})$). It must be noted that the vectors $\vec{m}_0(\vec{\rho})$ and $\vec{m}_d(\vec{\rho})$ are not physical parameters and should not be confused with the normalized unit vectors $\vec{M}_0(\vec{\rho}) / \left\|\vec{M}_0(\vec{\rho}) + \vec{M}_d(\vec{\rho})\right\|$ and $\vec{M}_d(\vec{\rho}) / \left\|\vec{M}_0(\vec{\rho}) + \vec{M}_d(\vec{\rho})\right\|$, respectively. The LLG equation can be written as

$$\bar{M}_s(\vec{\rho})\frac{\partial \vec{m}(\vec{\rho})}{\partial t} = \bar{\gamma}(\vec{\rho})\left(\bar{M}_s(\vec{\rho})\vec{m}(\vec{\rho}) \times \vec{H}(\vec{\rho})\right) + \bar{\alpha}(\vec{\rho})\bar{\gamma}(\vec{\rho})\left(\bar{M}_s^{-1}(\vec{\rho})\vec{M}_0(\vec{\rho}) \times \left(\bar{M}_s(\vec{\rho})\vec{m}(\vec{\rho}) \times \vec{H}(\vec{\rho})\right)\right), \quad (6\text{-}1)$$

where $\bar{\gamma}(\vec{\rho})$ is the gyromagnetic factor tensor and $\vec{H}(\vec{\rho})$ is the magnetic field that can be written as $\vec{H}(\vec{\rho}) = \vec{H}_{ext}(\vec{\rho}) + \vec{H}_{ex}(\vec{\rho}) + \vec{H}_{m}(\vec{\rho})$, while $\vec{H}_{ext}(\vec{\rho})$ is the external dc field, and $\vec{H}_{ex}(\vec{\rho})$ and $\vec{H}_{m}(\vec{\rho})$ are the exchange and dipolar fields induced by $\vec{M}(\vec{\rho})$, respectively. In the equilibrium, $\vec{M}_0(\vec{\rho}) \times \vec{H}_0(\vec{\rho}) = 0$, where $\vec{H}_0(\vec{\rho})$ is the static part of $\vec{H}(\vec{\rho})$. $\vec{H}_{0,ex}$ ($\vec{h}_{d,ex}$) and $\vec{H}_{0,m}$ ($\vec{h}_{d,m}$) are the exchange and dipolar fields arisen from $\vec{M}_0(\vec{\rho})$ ($\vec{M}_d(\vec{\rho})$), respectively. $\vec{m}(\vec{\rho}) = \vec{m}_0(\vec{\rho}) + \vec{m}_d(\vec{\rho})$, and $\bar{\alpha}(\vec{\rho})$ is the Gilbert damping constant tensor.

As a proof-of-concept demonstration, I focus on a cylindrical magnonic cloak. In order to assume dynamic invariance in the out-of-plane direction (i.e., *z* direction), the thickness of the thin film should be small such that the excitation frequency does not induce modes with out-of-plane wavenumbers. The cylindrical coordinates $r\varphi z$ is transformed into $r'\varphi' z'$, where $r' = g(r)$, $\varphi' = \varphi$, and $z' = z$, indicating that the mapping only occurs to the radial axis. The transformation function should satisfy the boundary conditions of $g(0) = c$ and $g(b) = b$, where *c* is the core radius, and *b* is the outer shell radius.

Under such a transformation, we can obtain $\vec{M}_d(\vec{\rho}) = T\vec{M}'_d(\vec{\rho}')$, where T is a diagonal matrix with components of $T_{rr} = \frac{\partial g(r)}{\partial r} = g'(r)$, $T_{\varphi\varphi} = \frac{r'}{r} = \frac{g(r)}{r}$, and $T_{zz} = 1$.[250,255] There are two types of spin waves in terms

of propagation, $\vec{q} \| \vec{M}_0$ and $\vec{q} \perp \vec{M}_0$, where $\vec{q}$ is the wave-vector. Figure 6-1(a) shows the schematic vector plot of $\vec{M}_d(\vec{\rho})$, where a cylindrical core is perfectly cloaked from propagating magnons of the $\vec{q} \perp \vec{M}_0$ type.

Equation (6-1) indicates that the magnetization dynamic has dual characteristics, which provide two degrees of freedom for controlling its inertia. One is the magnetic moment which is the manifestation of carrier and orbital spin population in a preferential direction in the Hilbert space ($\vec{M}$) and is determined by the moment tensor $\bar{\bar{M}}_s(\vec{\rho})$. The other one is the factor which determines the modification type and strength of gyration under an application of magnetic fields ($\bar{\bar{\gamma}}$). Conceptually, with any change in $\bar{\bar{M}}_s$ or $\bar{\bar{\gamma}}$, we can modify the point-wise dynamics, as it can be inferred from Eq. (6-1), and as schematically shown in Fig. 6-1(b) and (c). Figure 6-1(b) shows an isotropic magnetization vector ($\vec{M}$) precessing in an anisotropic $\bar{\bar{\gamma}}$. Figure 6-1(c) shows an anisotropic magnetization vector ($\vec{M}$) precessing in an isotropic $\bar{\bar{\gamma}}$. However, we should note that there are two strong non-local correlations in magnetic systems, exchange and dipolar interactions ($\vec{H}_{ex}(\vec{\rho})$ and $\vec{H}_m(\vec{\rho})$), which determine the dispersion relation of the spin waves for given $\bar{\bar{M}}_s$ and $\bar{\bar{\gamma}}$. First, a cloaking mechanism based on $\bar{\bar{\gamma}}$ is demonstrated. Subsequently, $\bar{\bar{M}}_s$ is utilized to cloak the cylindrical core. Finally, the feasibility of the proposed methods is discussed.

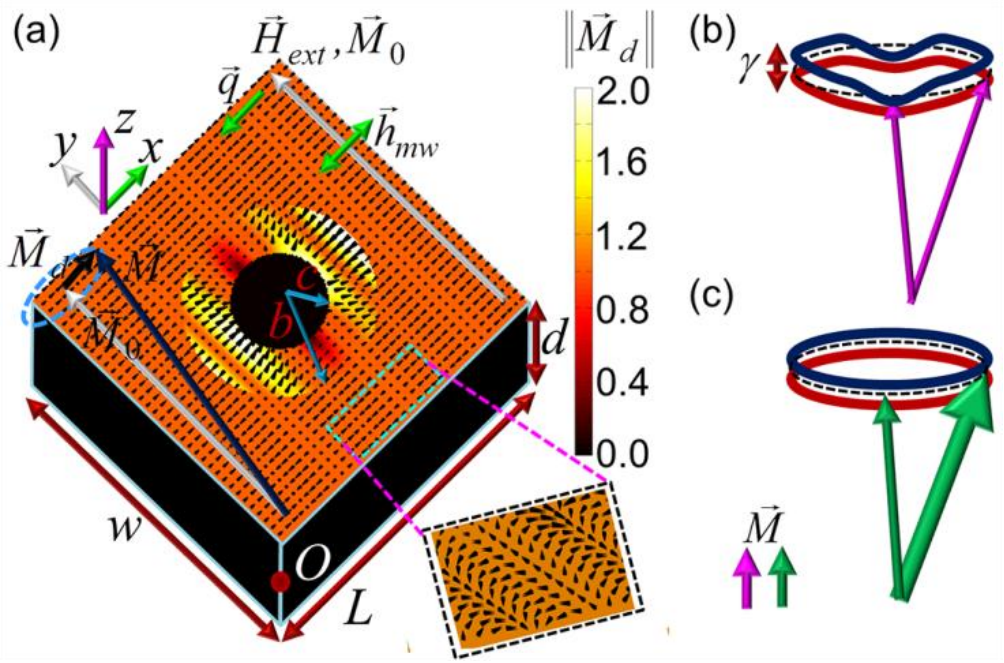

Figure 6-1. (a) The structural dimensions, fields and spin wave propagation direction, the respective Cartesian coordinate axes, $\vec{M}_0$ and $\vec{H}_{ext}$ outside the shell, and an example vector plot of $\vec{M}_d(\vec{\rho})$ (the color map represents the amplitude of $\vec{M}_d(\vec{\rho})$, $\|\vec{M}_d(\vec{\rho})\|$), where a cylindrical core is perfectly cloaked from propagating magnons (outside the shell, $\vec{M}_d(\vec{\rho}) = sin(2\pi/(100nm)\times x)\hat{x} + cos(2\pi/(100nm)\times x)\hat{z}$) of $\vec{q} \perp \vec{M}_0$ type. *O* represents the origin of the structure. The vector plot is magnified in the dashed box. (b) Schematic of magnetization precession in anisotropic $\bar{\gamma}$. (c) Schematic of magnetization precession in anisotropic $\bar{M}_s$. In (b) and (c), the distance between the red and blue curves indicate the amplitude of the gyromagnetic factor, while the black dashed curve indicates the trajectory of the magnetization $\vec{M}$. A thicker $\vec{M}$ indicates a higher moment in (c).

Based on the linear perturbation of Eq. (6-1), we can write the dynamic part of the magnetization as

$$\bar{M}_s(\vec{\rho})\frac{\partial \vec{m}_d(\vec{\rho})}{\partial t} = \left(\vec{\Pi} + \vec{\Omega}\right),$$

$$\vec{\Pi}(\vec{\rho}) = \bar{\gamma}(\vec{\rho})\left(\vec{M}_0(\vec{\rho}) \times \vec{h}_d(\vec{\rho}) + \bar{M}_s(\vec{\rho})\vec{m}_d(\vec{\rho}) \times \vec{H}_0(\vec{\rho})\right),$$

$$\vec{\Omega}(\vec{\rho}) = \bar{\alpha}(\vec{\rho})\bar{\gamma}(\vec{\rho})\left(\bar{M}_s^{-1}(\vec{\rho})\vec{M}_0(\vec{\rho}) \times \bar{\gamma}^{-1}(\vec{\rho})\vec{\Pi}(\vec{\rho})\right) \quad (6\text{-}2)$$

where $\vec{h}_d(\vec{\rho}) = \vec{h}_{d,ex}(\vec{\rho}) + \vec{h}_{d,m}(\vec{\rho})$. Here, the case of the propagating magnons of type $\vec{q} \perp \vec{M}_0$ (the similar discussions apply for $\vec{q} \parallel \vec{M}_0$) is considered, while outside the cloaking area (r > b) I assume homogeneous and isotropic magnetic moments $\bar{M}_s(\vec{\rho}) = M_{s,0}I$ (I is the identity matrix), and a gyromagnetic factor $\bar{\gamma}(\vec{\rho}) = \gamma_0 I$, where $\vec{M}_0 = M_{s,0}\hat{y}$. It is assumed that $W, L \to \infty$ and $d/W \ll 1$, where W is the width, L is the length, and d is the thickness of the structure (refer to Fig. 6-1(a)). Under this assumption, the dynamic part of the magnetization has the form $\vec{M}_d(\vec{\rho}) = \vec{M}_{d,0}(\vec{\rho})e^{-ik_x x}$ (k_x is the wavenumber in the x direction), and the dynamic demagnetization tensor $\bar{N}_d$ has only two non-zero components in the xyz coordination system, $N_{d,xx} = -\left[1-\left(1-e^{-k_x d}\right)\right]/k_x d$ and $N_{d,zz} = -1 - N_{d,xx}$.[270,271] The dynamic dipolar field is related to $\vec{M}_d(\vec{\rho})$ as $\vec{h}_{d,m}(\vec{\rho}) = \bar{N}_d\vec{M}_d(\vec{\rho})$. In addition, the static demagnetization tensor $\bar{N}_0$ has only one non-zero component $N_{d,zz} = -1$, while $\vec{H}_{0,m}(\vec{\rho}) = \bar{N}_0\vec{M}_0(\vec{\rho})$. The isotropic exchange field in the continuum limit can be written as $\vec{H}_{ex}(\vec{\rho}) = \Lambda\nabla^2\left[\vec{M}_0(\vec{\rho}) + \vec{M}_d(\vec{\rho})\right]$, where $\Lambda = A/2\pi M_{s,0}^2$ and A is the exchange constant. $\vec{h}_{d,ex}(\vec{\rho}) = -\Lambda k_x^2\vec{M}_d(\vec{\rho})$, while the homogeneity of $\vec{M}_0$ implies $\vec{H}_{0,ex}(\vec{\rho}) = 0$.

6.2.2 Cloaking shell designs based on anisotropic inhomogeneous $\bar{\gamma}$

In order to achieve cloaking, Eq. (6-2) should remain invariant if $\vec{M}_d(\vec{\rho})$ is rewritten as $T\vec{M}'_d(\vec{\rho}')$. The conditions for Eq. (6-2) to remain invariant in the transformed space are $T^{-1}\vec{\Pi}(\vec{\rho}') = \vec{\Pi}'$ and $T^{-1}\vec{\Omega}(\vec{\rho}') = \vec{\Omega}'$, where $\vec{\Pi}' = \bar{\gamma}'(\vec{\rho})\left(\vec{M}'_0(\vec{\rho}') \times \vec{h}'_d(\vec{\rho}') + M_{s,0}\vec{m}'_d(\vec{\rho}') \times \vec{H}'_0(\vec{\rho}')\right)$ and $\vec{\Omega}' = \bar{\alpha}'(\vec{\rho}')\bar{\gamma}'(\vec{\rho}')\left(\frac{1}{M_{s,0}}\vec{M}'_0(\vec{\rho}') \times \left(\gamma_0^{-1}\vec{\Pi}'\right)\right)$ (values with prime refer to the transformed space). In the $\bar{\gamma}$-based design, it is assumed that the moment is isotropic and $\bar{M}'_s(\vec{\rho}')$ can be replaced by the scalar $M'_{s,0}(\vec{\rho}')$. The invariant conditions to satisfy $T^{-1}\vec{\Pi}(\vec{\rho}') = \vec{\Pi}'$ and $T^{-1}\vec{\Omega}(\vec{\rho}') = \vec{\Omega}'$ are derived to be

$$H'_{0,\varphi}(\vec{\rho}') = T_{rr}H_{0,\varphi}(\vec{\rho}'),\ M'_{0,\varphi}(\vec{\rho}') = T_{rr}M_{0,\varphi}(\vec{\rho}'),$$

$$H'_{0,r}(\vec{\rho}') = T_{\varphi\varphi}H_{0,r}(\vec{\rho}'),\ M'_{0,r}(\vec{\rho}') = T_{\varphi\varphi}M_{0,r}(\vec{\rho}'),$$

$$\gamma'_{rr}(\vec{\rho}') = \gamma_0\frac{1}{T_{rr}^2},\ \gamma'_{\varphi\varphi}(\vec{\rho}') = \gamma_0\frac{1}{T_{\varphi\varphi}^2},\ \gamma'_{zz} = \gamma_0,$$

$$\alpha'_{rr(\varphi\varphi)}(\vec{\rho}') = \alpha_0,\ \alpha'_{zz}(\vec{\rho}') = \alpha_0\frac{\left(M_{0,r}(\vec{\rho}')\right)^2 + \left(M_{0,\varphi}(\vec{\rho}')\right)^2}{T_{\varphi\varphi}^2\left(M_{0,r}(\vec{\rho}')\right)^2 + T_{rr}^2\left(M_{0,\varphi}(\vec{\rho}')\right)^2}. \quad (6\text{-}3)$$

γ'_{ii} (α'_{ii}), i = r, φ, and z, are the diagonal components of $\bar{\gamma}'$ ($\bar{\alpha}'$). α_0 is the value of the homogeneous Gilbert damping constant outside the cloaking area (r > b). For the $\bar{\gamma}$-mechanism, $T^{-1}\vec{\Pi}(\vec{\rho}') = \vec{\Pi}'$ results in three coupled equations, which with a straightforward algebraic investigation, determine the

invariant conditions for different spatial coordinates of $\vec{H}_0'(\vec{\rho}')$ and $\vec{M}_0'(\vec{\rho}')$ based on the matrix components of *T*. Such invariance is achieved using the $\bar{\gamma}'(\vec{\rho}')$ tensor as a degree of freedom, as shown in Eq. (6-3). To be more specific, the $T^{-1}\vec{\Pi}(\vec{\rho}') = \vec{\Pi}'$ in the *z* direction leads to (note that $\vec{h}_d(\vec{\rho}) = T\vec{h}_d'(\vec{\rho}')$ and $\vec{M}_d(\vec{\rho}) = T\vec{M}_d'(\vec{\rho}')$)

$$\begin{matrix} \frac{\gamma_0}{T_{zz}}\left[\left(M_{0,r}T_{\varphi\varphi}h_{d,\varphi}' - M_{0,\varphi}T_{rr}h_{d,r}'\right) + \left(T_{rr}M_{d,r}'H_{0,\varphi} - T_{\varphi\varphi}M_{d,\varphi}'H_{0,r}\right)\right]\hat{z} = \\ \gamma_{zz}'\left[\left(M_{0,r}'h_{d,\varphi}' - M_{0,\varphi}'h_{d,r}'\right) + \left(M_{d,r}'H_{0,\varphi}' - M_{d,\varphi}'H_{0,r}'\right)\right]\hat{z} \end{matrix} . \qquad (6\text{-}4)$$

With T_{zz} = 1, Eq. (6-4) can be satisfied if $\gamma_{zz}' = \gamma_0$, $H_{0,\varphi}'(\vec{\rho}') = T_{rr}H_{0,\varphi}(\vec{\rho}')$, $M_{0,\varphi}'(\vec{\rho}') = T_{rr}M_{0,\varphi}(\vec{\rho}')$, $H_{0,r}'(\vec{\rho}') = T_{\varphi\varphi}H_{0,r}(\vec{\rho}')$, and $M_{0,r}'(\vec{\rho}') = T_{\varphi\varphi}M_{0,r}(\vec{\rho}')$. In the presence of the latter conditions and noting that $M_{0,z}(\vec{\rho}') = 0$ and $H_{0,z}(\vec{\rho}') = 0$, the invariance of $T^{-1}\vec{\Pi}(\vec{\rho}') = \vec{\Pi}'$ in the φ and *r* directions can be achieved if

$$\frac{\gamma_0}{T_{rr}}\left[\left(-\frac{M_{0,\varphi}'}{T_{rr}}T_{zz}h_{d,z}'\right) + \left(T_{zz}M_{d,z}'\frac{H_{0,\varphi}'}{T_{rr}}\right)\right]\hat{r} = \gamma_{rr}'\left[\left(-M_{0,\varphi}'h_{d,z}'\right) + \left(M_{d,z}'H_{0,\varphi}'\right)\right]\hat{r},$$

$$\frac{\gamma_0}{T_{\varphi\varphi}}\left[\left(\frac{M_{0,r}'}{T_{\varphi\varphi}}T_{zz}h_{d,z}'\right) + \left(-T_{zz}M_{d,z}'\frac{H_{0,r}'}{T_{\varphi\varphi}}\right)\right]\hat{\varphi} = \gamma_{\varphi\varphi}'\left[\left(M_{0,r}'h_{d,z}'\right) + \left(M_{d,z}'H_{0,r}'\right)\right]\hat{\varphi}. \qquad (6\text{-}5)$$

Equation (6-5) can be satisfied if $\gamma_{rr}'(\vec{\rho}') = \gamma_0\frac{1}{T_{rr}^2}$ and $\gamma_{\varphi\varphi}'(\vec{\rho}') = \gamma_0\frac{1}{T_{\varphi\varphi}^2}$, respectively. By using the invariance conditions that satisfy $T^{-1}\vec{\Pi}(\vec{\rho}') = \vec{\Pi}'$, the constraints on the components of the Gilbert damping tensor $\bar{\alpha}'$ are determined by considering $T^{-1}\vec{\Omega}(\vec{\rho}') = \vec{\Omega}'$, following similar procedures (see Eq. (6-3) for the $\bar{\alpha}'$ components).

It should be mentioned that the conditions in Eq. (6-3) satisfy the invariant conditions in all three directions of the cylindrical coordination system, if $\vec{h}_d(\vec{\rho}) = T\vec{h}'_d(\vec{\rho}')$ (note that $\vec{M}_d(\vec{\rho}) = T\vec{M}'_d(\vec{\rho}')$). This condition holds, because $\vec{h}_d(\vec{\rho})$ can be written as a linear function of $\vec{M}_d(\vec{\rho})$ ($\vec{h}_d(\vec{\rho}) = \left(\bar{N}_d - \Lambda k_x^2\right)\vec{M}_d(\vec{\rho})$, where $\bar{N}_d$ does not have a spatial functionality) under the assumptions given above ($\bar{M}_s(\vec{\rho}) = M_{s,0}I$, $W, L \to \infty$, $d/W \ll 1$, and $\vec{M}_d(\vec{\rho}) = \vec{M}_{d,0}(\vec{\rho})e^{-ik_x x}$).

The functionality of $M'_{0,\varphi(r)}(\vec{\rho}')$ in Eq. (6-3) will modify the static field $H_{0,\varphi(r)}(\vec{\rho}')$ through the exchange and dipolar fields, which will contradict the other assumptions which led to the established invariance conditions. To cancel the redundant static exchange and dipolar fields, $H_{0,\varphi(r)}(\vec{\rho}')$ should be modified as

$$H_{0,\varphi(r)}(\vec{\rho}') = H'_{0,\varphi(r)}(\vec{\rho}') + \left[-\left(\int_V \bar{G}(\vec{\rho}',\vec{\tau})\vec{M}'_0(\vec{\tau})\,d\tau\right) - \Lambda\nabla^2\left[\vec{M}'_0(\vec{\rho}')\right]\right]\cdot\hat{\varphi}(\hat{r}) \,, \quad (6\text{-}6)$$

where $\bar{G}(\vec{\rho}',\vec{\tau})$ is the dipolar Green function tensor in the cylindrical coordination system. Therefore, the perfect cloaking of magnons which are governed by Eq. (6-2) can be achieved for the aforementioned assumptions, if Eqs. (6-3, 6-6) are satisfied. This method is named as the $\bar{\gamma}$ -mechanism, contrasting the $\bar{M}_s$ -mechanism that will be described later. It can be inferred from Eq. (6-3), that in the $\bar{\gamma}$ -mechanism, $\bar{M}'_s(\vec{\rho}') = M'_s(\vec{\rho}')I$, where $M'_s(\vec{\rho}') = \left\|\vec{M}'_0(\vec{\rho}')\right\|$ is not homogeneous but is isotropic.

6.2.3 Cloaking shell designs based on anisotropic inhomogeneous $\bar{M}_s$

For the $\bar{\gamma}$-mechanism, the conditions that should be held for Eq. (6-2) to remain invariant under the space transformation required for cloaking ($T^{-1}\vec{\Pi}(\vec{\rho}') = \vec{\Pi}'$ and $T^{-1}\vec{\Omega}(\vec{\rho}') = \vec{\Omega}'$) are investigated. However, the magnetization is a vector field whose magnitude can be anisotropic, enabling another approach for rendering Eq. (6-2) invariant. In the transformed space, the dynamic part of the magnetization should be $\vec{M}'_d(\vec{\rho}') = T^{-1}\vec{M}_d(\vec{\rho})$, which can be achieved if

$$\bar{M}'_s(\vec{\rho}') = M_{s,0}T^{-1}. \tag{6-7}$$

The conditions to achieve invariance in Eq. (6-2) with the assumption of Eq. (6-7) become

$$H'_{0,\varphi}(\vec{\rho}') = H_{0,\varphi}(\vec{\rho}'),\ M'_{0,\varphi}(\vec{\rho}') = M_{0,\varphi}(\vec{\rho}'),\ m'_{0,\varphi}(\vec{\rho}') = T_{\varphi\varphi}m_{0,\varphi}(\vec{\rho}'),$$

$$H'_{0,r}(\vec{\rho}') = H_{0,r}(\vec{\rho}'),\ M'_{0,r}(\vec{\rho}') = M_{0,r}(\vec{\rho}'),\ m'_{0,r}(\vec{\rho}') = T_{rr}m_{0,r}(\vec{\rho}'),$$

$$\alpha'_{rr}(\vec{\rho}') = \frac{\alpha_0}{T_{\varphi\varphi}} \quad , \quad \alpha'_{\varphi\varphi}(\vec{\rho}') = \frac{\alpha_0}{T_{rr}} \quad ,$$

$$\alpha'_{zz}(\vec{\rho}') = \alpha_0 \frac{\left(M_{0,r}(\vec{\rho}')\right)^2 + \left(M_{0,\varphi}(\vec{\rho}')\right)^2}{T_{rr}\left(M_{0,r}(\vec{\rho}')\right)^2 + T_{\varphi\varphi}\left(M_{0,\varphi}(\vec{\rho}')\right)^2}. \tag{6-8}$$

For the $\bar{M}_s$-mechanism, $\vec{\Pi}(\vec{\rho}') = \vec{\Pi}'$ should be satisfied instead of $T^{-1}\vec{\Pi}(\vec{\rho}') = \vec{\Pi}'$, because the assumption in Eq. (6-7) for the $\bar{M}'_s$ tensor renders the left part of Eq. (6-2) invariant. To satisfy $\vec{\Pi}(\vec{\rho}') = \vec{\Pi}'$, the condition of Eq. (6-7) is only required, and the values of the bias field and the static part of the

magnetization in the prime and the physical space remain equivalent, $\vec{H}_0'(\vec{\rho}') = \vec{H}_0(\vec{\rho}')$ and $\vec{M}_0'(\vec{\rho}') = \vec{M}_0(\vec{\rho}')$. It should be noted that since $\bar{M}_s'$ is anisotropic, $\vec{M}_0'(\vec{\rho}')$ is not necessarily parallel to $\vec{m}_0'(\vec{\rho}')$ in the shell area (refer to Eq. (6-8)). Similar to the $\bar{\gamma}$-mechanism, the invariance of $\vec{\Pi}(\vec{\rho}') = \vec{\Pi}'$ is guaranteed only if $\vec{h}_d(\vec{\rho}) = T\vec{h}_d'(\vec{\rho}')$ and $\vec{M}_d(\vec{\rho}) = T\vec{M}_d'(\vec{\rho}')$, which is achieved under the assumptions stated previously ($\bar{M}_s(\vec{\rho}) = M_{s,0}I$, $W, L \to \infty$, $d/W \ll 1$, and $\vec{M}_d(\vec{\rho}) = \vec{M}_{d,0}(\vec{\rho})e^{-ik_x x}$). Finally, $\vec{\Omega}(\vec{\rho}') = \vec{\Omega}'$ should also be satisfied, which requires that the components of the tensor $\bar{\alpha}'$ to be as indicated in Eq. (6-8).

It should be noted that the gyromagnetic factor is assumed to be isotropic for the $\bar{M}_s$-mechanism, $\bar{\gamma}'(\vec{\rho}') = \gamma_0 I$. In contrast to the $\bar{\gamma}$-mechanism, $M_{0,r(\varphi)}'(\vec{\rho}') = M_{0,r(\varphi)}(\vec{\rho}')$ holds for the $\bar{M}_s$-mechanism (comparing Eq. (6-3) and Eq. (6-8)), therefore there is no modification in the static exchange or dipolar field ($H_{0,\varphi(r)}(\vec{\rho}') = H_{0,\varphi(r)}'(\vec{\rho}')$).

6.3 Numerical demonstration of the cloaking mechanisms

In order to demonstrate the functionality of the proposed magnonic cloak, an in-house code has been developed to solve the LLG equation (Eq. (6-1)) for the anisotropic $\bar{\gamma}$, $\bar{M}_s$, and $\bar{\alpha}$. In each time step, the exchange and dipolar fields were first calculated. Exchange fields were calculated using only the nearest neighbors. Dipolar fields were calculated using the fast Fourier

transform method. After field calculations, the anisotropic LLG differential equation, Eq. (6-1), multiplied by $\bar{M}_s^{-1}$ on both sides, was solved using the Runge-Kutta numerical method for the magnetization of each cell. The maximum time step of 0.01 ps was used. The time-steps were modified to meet the relative error criteria of 10^{-9}.

It is assumed that the structure dimensions in Fig. 6-1(a) are W = 420 nm, L = 820 nm, c = 50 nm, b = 100 nm, d = 3.8 nm, x_c = 550 nm, and y_c = 210 nm (x_c and y_c are the center positions of the cylindrical core along the x and y directions, respectively, with respect to the origin). The transformation function $g(r) = c + r(b-c)/b$ is employed. The meshing cells are cubic and have the dimensions of 2 nm × 2 nm × 3.8 nm. In the non-transformed area, it is assumed that $\vec{m}_0 \parallel \hat{y}$, $\vec{H}_{ext} = 10000\hat{y}$ Oe, $M_{s,0} = 8\times10^5$ A/m, $A = 0.5\times10^{-11}$ J/m, and $\gamma_0 = 2.2\times10^5$ Hz/(A·m). The microwave excitation is applied as $\vec{h}_{mw} = 1\times sin(\omega_{mw}t)\hat{x}$ Oe, at x = 800 nm. The microwave excitation frequency was set as $\omega_{mw} = 2\pi\times50\times10^9$ rad/s. Matched layers (ML) of 4 nm width were applied in all four in-plane boundaries. In the ML area $\alpha_0 = 1$, while $\alpha_0 = 0.01$ for the rest of the structure.

Figure 6-2 shows the snapshot of the magnetization in the z direction (M_z) at t = 2.2 ns (well before the wave reaches the ML layer at x = 0, in which case the reflection drives its adjacent magnetization dynamics unstable). The dashed lines at x = 800 nm represent the microwave excitation lines, inducing spin waves propagating in the $-x$ direction. The horizontal lines in Fig. 6-2 separate regions of each graph that have a specific color-code shown in their

right side. Figure 6-2(a) demonstrates the spin wave configuration when there is no cylindrical core (b = 0 and c = 0). It can be observed that due to the finite width (W = 420 nm), in addition to the propagating magnons in the $-x$ direction, standing spin waves are formed across the y direction ($k_y \neq 0$). Figure 6-2(b) shows a case with a cylindrical core while no cloaking mechanism was applied (b = 50 nm and c = 50 nm). The shadowing of the core in the spin wave configuration can be clearly observed in Fig. 6-2(b). Figure 6-2(c) and Figure 6-2(d) show the cases where the $\bar{\gamma}$-mechanism and $\bar{M}_s$-mechanism were applied, respectively, with b = 100 nm and c = 50 nm. Both Fig. 6-2(c) and Fig. 6-2(d) demonstrate the reduction of the shadow of the core in comparison with Fig. 6-2(b).

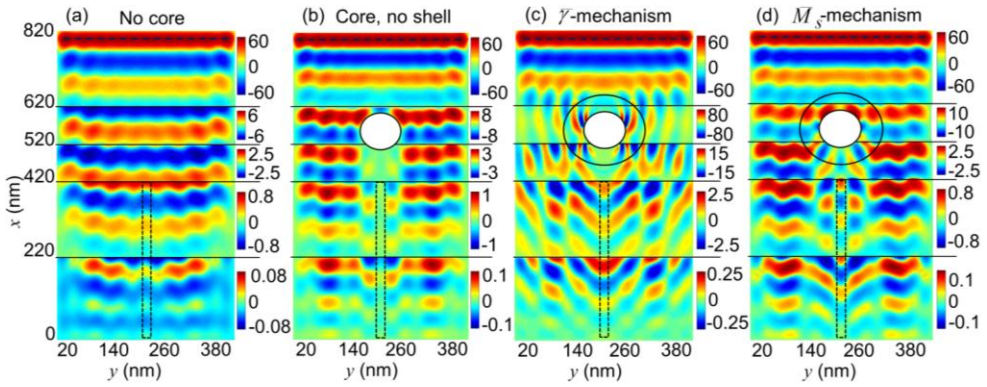

Figure 6-2. The magnetization in the z direction (M_z) after 2.2 ns of an excitation with $\vec{h}_{mw} = 1 \times sin\left(2\pi / \left(50GHz\right) \times t\right)\hat{x}$ Oe at x = 800 nm. (a) No cylindrical core (b = 0 and c = 0). (b) Cylindrical core but no cloaking shell (b = 50 nm and c = 50 nm). (c) Cylindrical core with the shell designed for the $\bar{\gamma}$-mechanism (b = 100 nm and c = 50 nm). (d) Cylindrical core with the shell designed for the $\bar{M}_s$-mechanism (b = 100 nm and c = 50 nm). The dashed boxes represent the shadow region used for calculation of $M_{z,sr}(x)$ plotted in Fig. 6-3(a). The inner circle shows the boundary of the core. The larger circle shows the outer boundary of the shell.

The values of $M_{z,sr}(x)=\frac{1}{20\,nm}\int_{y_c-10nm}^{y_c+10nm} M_z(x,y)\,dy$ are shown in Fig. 6-3(a) and 6-3(b) for $0\le x\le 420$ nm and $0\le x\le 820$ nm, respectively. In particular, Fig. 6-3(a) shows a quantitative comparison of M_z in the shadowing region (the dashed boxes in Fig. 6-2) for all the four cases in Fig. 6-2. It can be seen that the spin-waves are suppressed after the propagation through the core where no cloaking mechanism is applied, while both the cloaking mechanisms have the values of $M_{z,sr}(x)$ close to that of no core. Despite this signature of cloaking (reduction in the core shadow) shown in Fig. 6-2 and Fig. 6-3(a), Fig. 6-3(c), showing that the total average of M_z in the y direction ($M_{z,T}(x)=\frac{1}{420\,nm}\int_{0nm}^{420nm} M_z(x,y)\,dy$) for $0\le x\le 420$ nm, has almost the same value for all four cases. The reason is that the energy exchange between the standing spin wave in the y direction and the propagating spin wave in the x direction provides a nonlinear route for the magnon population to pass through such cores. This can also be justified by the results in Fig. 6-3(b) and (d) that show $M_{z,sr}(x)$ and $M_{z,T}(x)$ for the whole range of x, respectively, with similar amplitudes for all four cases. If such standing spin waves in the y direction are omitted from the system by expanding the width of the magnetic structure ($W\to\infty$), we can expect to observe higher reflection and shadow of the core with no cloaking mechanism, and clearer cloaking for both the $\bar{\gamma}$-mechanism and $\bar{M}_s$-mechanism.

The main reason behind the imperfection of the cloaking for both mechanisms (refer to Fig 6-2(c-d)) is that due to the existence of the waveform

in the *y* direction, the assumption of $\vec{h}_d(\vec{\rho}) = T\vec{h}'_d(\vec{\rho}')$, which was the basis for derivation of the material properties in the shell, is no longer perfectly satisfied. $\vec{h}_d(\vec{\rho}) = T\vec{h}'_d(\vec{\rho}')$ holds if only one of the $\vec{q} \perp \vec{M}_0$ or $\vec{q} \parallel \vec{M}_0$ modes exists. Other reasons for the cloaking imperfections observed in Fig. 6-2(c-d) are using cubic (aligned with the Cartesian axes) and a limited number of cells in the shell for the simulations. The difference between the results of the $\bar{\gamma}$-mechanism and $\bar{M}_s$-mechanism, corresponding to Fig. 6-2(c) and (d) respectively, originates from the degree of vulnerability of the methods with respect to the discrepancy of $\vec{h}_d(\vec{\rho}) = T\vec{h}'_d(\vec{\rho}')$ from perfection due to mixing of the $\vec{q} \perp \vec{M}_0$ and $\vec{q} \parallel \vec{M}_0$ modes. For the $\bar{M}_s$-mechanism, mixing affects the dynamic dipolar field ($\vec{h}'_{d,m}(\vec{\rho}')$) leading to distortion and inaccuracy of Eq. (6-8), while for the $\bar{\gamma}$-mechanism, in addition to the distortion induced by $\vec{h}'_{d,m}(\vec{\rho}')$, Eq. (6-3) no longer holds exactly. Therefore, more distortion for the $\bar{\gamma}$-mechanism in comparison with the $\bar{M}_s$-mechanism in the presence of mode-mixing is expected, as inferred by comparing Fig. 6-2(c) and Fig. 6-2(d).

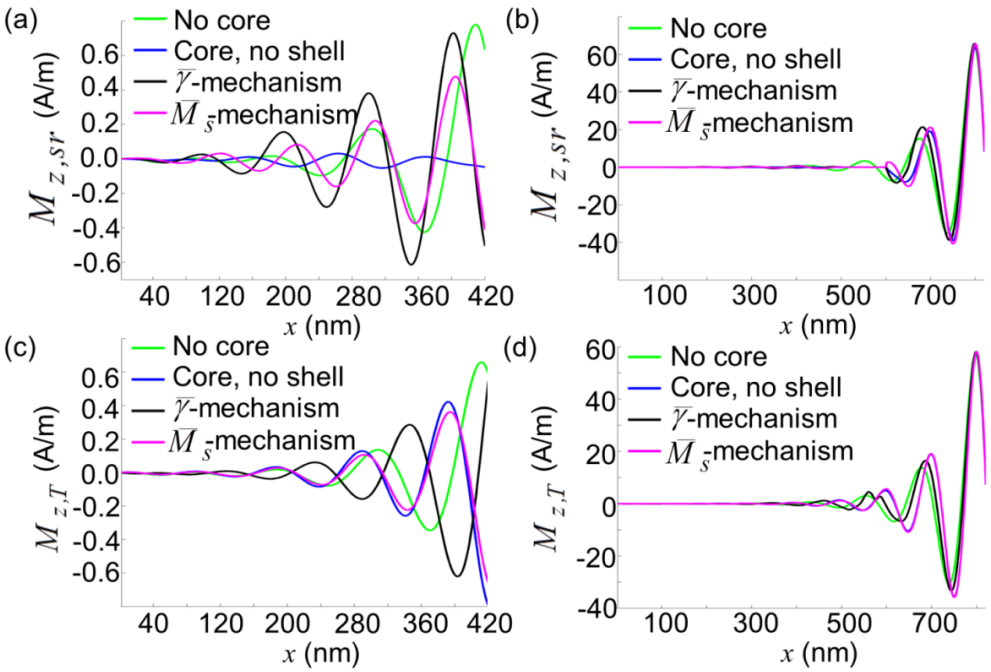

Figure 6-3. The variation of average M_z ($M_{z,sr}(x)=\frac{1}{20\,nm}\int_{y_c-10nm}^{y_c+10nm} M_z(x,y)dy$) for (a) $0\le x\le 420$ nm (the shadow region of the core), and (b) $0\le x\le 820$ nm. The variation of average M_z ($M_{z,T}(x)=\frac{1}{420\,nm}\int_{0nm}^{420nm} M_z(x,y)dy$) for (c) $0\le x\le 420$ nm and (d) $0\le x\le 820$ nm.

6.4 Spin-metamaterials for transformation magnonics

6.4.1 Physical feasibility of the $\bar{\gamma}$-mechanism

Figures 6-4(a-c) show the material properties ($\gamma_{rr}/\gamma_{\varphi\varphi}$, $M_s(\vec{\rho})$, and α_{zz}/α_0) and the direction of the external field $\vec{H}_{ext}(\vec{\rho})$ for the $\bar{\gamma}$-mechanism based on Eq. (6-3). Figure 6-5(a-b) show $M_{s,rr}/M_{s,\varphi\varphi}$ and α_{zz}/α_0 for the $\bar{M}_s$-mechanism based on Eq. (6-7) and Eq. (6-8). Magnon cloaking by the $\bar{\gamma}$-mechanism or the $\bar{M}_s$-mechanism cannot be achieved in metallic ferromagnets

as the large anisotropy in $\bar{\gamma}$ or $\bar{M}_s$ is not possible. In addition, the anisotropy and tuning range of $\bar{\gamma}$ is limited in the magnetic molecules or magnetic semiconductors for realizing the $\bar{\gamma}$-mechanism (refer to Fig. 6-4(a)).[272,273] However, high anisotropy and the large tuning range of $\bar{\gamma}$ is possible in quantum dot molecules (QDM) (refer to the box in Fig. 6-4(d) for a stacked quantum dot molecule schematic).[68,274-276] Spin states in quantum dots (QD) or QDMs are the main candidates for quantum computing.[277] It has been demonstrated theoretically and experimentally that the Lande g-factor or $\bar{\gamma}$ in our notation, can be tuned in a large range (including zero crossing) in quantum wells (QW), QDs, and QDMs with an electric field. However, for QDMs, the effect of the electric field is much richer on tuning both the amplitude and the anisotropy of the hole-spin Lande g-factor. There are rich crossings and anti-crossings for the ground, the excitonic, and the charged excitonic states.[67,68,161,274,275,278-282] The crossings and anti-crossings in QDMs occur due to bonding and anti-bonding of electron and hole wave functions between the two QDs in a typical stacked QDM (refer to Fig. 6-4(d)) which occur by changing the electric field.[68,274,278] In the right part of the Fig. 6-4(d), a schematic of a QDM, its respective Cartesian coordination, the applied electric field in the *z* direction ($E_{z,q}$, where q is the number of the QDM in the QDM ensemble) and the magnetic field $\vec{B}_q$ are depicted.

It has been demonstrated theoretically that for a QDM in Fig. 6-4(d), the axes of the Lande g-factor ($\bar{\gamma}$) ellipsoid are along the *z* direction, $\hat{x}_q + \hat{y}_q$, and $\hat{x}_q - \hat{y}_q$ (x_q and y_q are the local Cartesian directions for the QDM number q).

Based on this information about QDMs, it is proposed that the $\bar{\gamma}$-mechanism be utilized for an ensemble of QDMs as depicted schematically in the left part of Fig. 6-4(d). If we assume $\left(\hat{x}_q + \hat{y}_q\right) \| \hat{r}$ and $\left(\hat{x}_q - \hat{y}_q\right) \| \hat{\varphi}$, the value of γ_{zz} can be tuned for more than 100%, while γ_{rr} and $\gamma_{\varphi\varphi}$ can be tuned for up to 800% with varying $E_{z,q}$.[68] However, γ_{rr} and γ_{zz} are spatially constant in the shell, while varying $E_{z,q}$ for tuning $\gamma_{\varphi\varphi}$ will change γ_{rr} and γ_{zz} as well. To overcome this issue, the local angle (θ_q) of $\hat{x}_q + \hat{y}_q$ can be utilized with respect to $\hat{r}$ as another variable. In addition, the application of a spatially functionalized strain (adjacent piezoelectric layers) or doping can be used as other tuning factors for achieving the desired $\bar{\gamma}$ at the position of QDM number q (refer to Fig. 6-4(a)). To achieve the required $M_s\left(\vec{\rho}\right)$ configuration for the $\bar{\gamma}$-mechanism (refer to Fig. 6-4(b)), the density of the QDMs in the cloaking shell should be spatially functionalized. However, the inhomogeneous distribution of QDMs in the shell causes inhomogeneity of distance between the QDMs, which directly affects the respective exchange mechanisms. To compensate this effect, a spatially functionalized electric field can be applied in the semiconductor regions between the QDMs to tune the exchange strength.[162,283] The spin lifetime in QDs can be up to the order of μs,[284] and due to the atomic-like behavior of QDs, the phenomenological Gilbert damping and the required α_{zz} / α_0 configuration (refer to Fig. 6-4(c)) can be ignored.

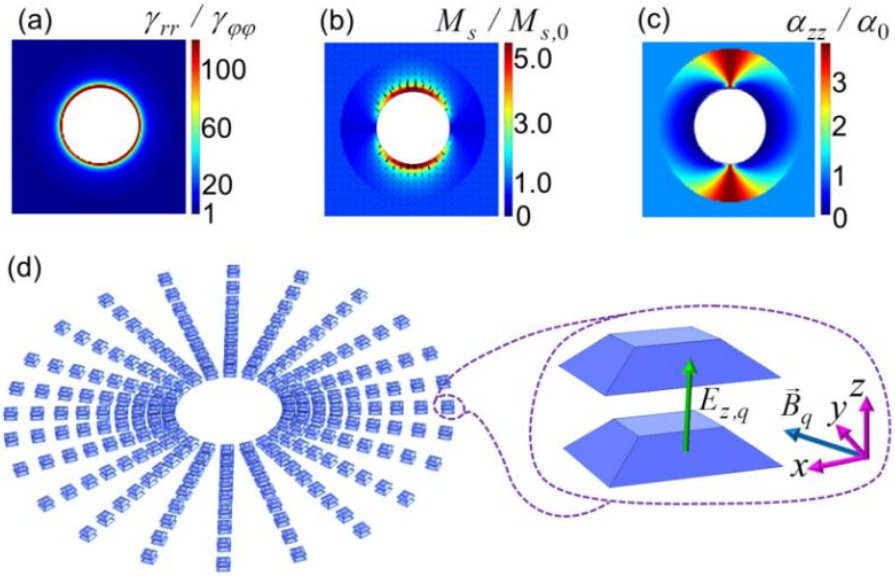

Figure 6-4. Spatial pattern of (a) $\gamma_{rr}/\gamma_{\varphi\varphi}$, (b) $M_s(\vec{\rho})$ (color map) and $\vec{H}_{ext}(\vec{\rho})$ (cone plot), and (c) α_{zz}/α_0 for the $\bar{\gamma}$ -mechanism. (d) The schematic of the ensemble of quantum dot molecules is in the left section. The schematic of an individual quantum dot molecule, its Cartesian coordination, the electric field ($E_{z,q}$), and magnetic field ($\vec{B}_q$) are in the right section. In (a-c), the white regions in the center are hollow and no value is assigned to them.

6.4.2 Physical feasibility of the $\bar{M}_s$-mechanism

There are theoretical and experimental demonstrations for anisotropies in both the moment and exchange interaction in magnetic semiconductors.[160,285-294] Those anisotropies stem from the spin orbit interactions (SOI) in the materials that lack the inversion symmetry. In bulk semiconductors with wurtzite or zinc-blende crystalline structures, the antisymmetric part of the anisotropic exchange of the localized electrons is dominated by Dzyaloshinskii-Moriya interaction (DMI)[239,240] which is the first-order perturbation in the SOI of Rashba[44] and Dyakonov-Kachorovskii[295] types. There have been

experimental demonstrations of anisotropic exchange by showing anisotropic dephasing in bulk GaN and impurity-bound electrons in n-doped ZnO.[287,288]

There have been theoretical and experimental demonstrations of magnetic orderings in semiconductors.[285,289,293,296-312] Such magnetic orderings have been achieved due to the presence of carrier-doping, cation vacancy, cation substitution, anion vacancy, anion substitution, interstitial impurities, structural strain, and a combination of them. Although a wide range of doping and defect gives rise to local spins or orbital moments, not all of them forms a long range magnetic order. The exchange interaction between local moments is governed by several mechanisms, such as double exchange and superexchange. In addition to large magnetic orderings, the anisotropy in moments has been demonstrated in several oxides like substituted ZnO, V doped SnO_2, HfO_2, and TiO_2, as well as $Li_2(Li_{1-x}Fe_x)N$.[285,286,289,293,298,312,313] The anisotropic moment arises due to lifting of the degeneracy in orbital interactions, and mixing of molecular orbitals surrounding the point defects induced by oxygen vacancies, cation vacancies and interstitial or substitution impurities. Molecular orbitals surrounding the point defects mix with the nearest neighbors and next nearest neighbors (source of magnetic ordering), enabling the possibility of different anisotropy patterns based on the respective position of the impurities (depends on the SOI strength of the defect).

In order to be more specific, a system of interstitial impurities and oxygen vacancies in a metal-oxide is proposed. Figure 6-5(c) shows a 2×2×1 supercell of rutile crystalline structure consisting of metal sites and oxygen sites, hosting two interstitial impurities and an oxygen vacancy, for example. The surrounding oxygen octahedral of the interstitial imposes a crystal field on the

impurity and possibly splits the degenerate bands based on the symmetry rules. If the bonding molecular orbitals induced by impurities are filled with carriers, an orbital moment can be generated. In the presence of spin-orbit coupling, the impurity induced spin-moment aligns with the orbital moment and if an exchange mechanism exists, both the orbital moment and spin moment can give rise to a macroscopic ferromagnetic order. The presence of oxygen vacancy (V_o) provides electrons, and if its defect state overlaps with the impurity induced bands, there could be both orbital moments and long-range exchange interaction.[285,289,293,297,302,304,305,308,309,311] Therefore, it is important to choose the host and interstitial metals in order to have the required interactions. The amplitude and the direction of the electric field $\vec{E}_i$ on the supercell *i* can determine the respective configuration of the impurities and defects.

In the rutile structure, there are four independent octahedral sites for interstitial impurities, as indicated in Fig. 6-5(d). Figure 6-5(d) shows a simplified demonstration of the molecular orbitals as charge rings $\sigma_{1(2,3,4)}$ that give rise to orbital moment vectors $\vec{v}_{1(2,3,4)}$. The coexistence of orbital moment and high SOI results in anisotropic moments. In order to control the axis of anisotropy, there is a need for at least two interacting interstitial impurities. Figure 6-5(e) shows a possible route to control the anisotropy axis in the entire three dimensions. If the distance of the V_o to the interstitial impurity in site *A* is less than its distance to site *B*, the carrier density in the charge ring of *A* will be higher than that of *B*. Therefore the orbital magnetization in *A* will be higher than that in *B* ($|\vec{v}_A| > |\vec{v}_B|$). Hybridization of *A* and *B* charge rings results in a net

orbital moment $\vec{v}_T$. It can be inferred from Fig. 6-5(d) and 6-5(e) that the direction of $\vec{v}_T$ can be tuned by placing the impurities in different octahedral sites and placing the oxygen vacancy in different oxygen sites. Spatial functionalization of the temperature,[289] impurity concentration, charge doping, and oxygen vacancy can be utilized for tuning the amplitude of the moment as is needed in addition to the anisotropy direction to achieve the desired $\bar{M}_s$.

The proposed method of transformation magnonics for spin wave cloaking may be very challenging to be realized experimentally, as it requires spatially varying anisotropic $\bar{\gamma}$ or $\bar{M}_s$ with precision on the nanometer scale. However, the proposed mechanisms may find plausible applications in simpler transformation designs such as magnon lenses, concentrators, bending waveguides, and ultimately spin-based quantum computing.

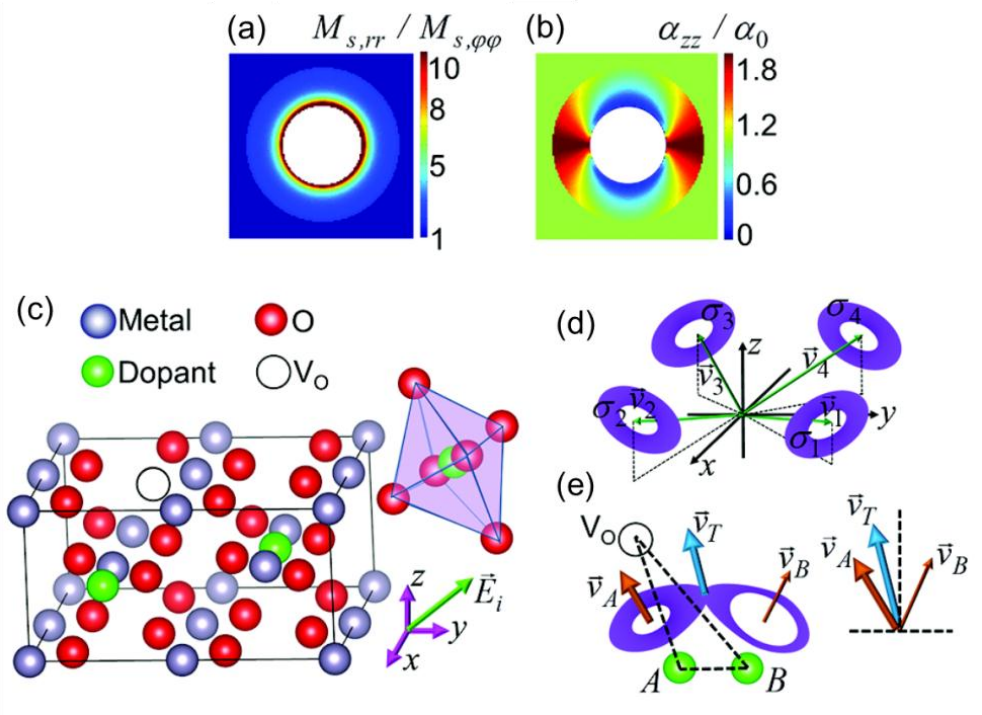

Figure 6-5. Spatial pattern of (a) $M_{s,rr} / M_{s,\varphi\varphi}$, and (b) α_{zz} / α_0 for the $\bar{M}_s$ -mechanism. (c) Example schematic of a rutile crystalline structure consisting of metal and oxygen sites, as well as an interstitial impurity and oxygen vacancy positions. The right panel is an example of the octahedral oxygen coordination of an interstitial impurity. $\vec{E}_i$ is the external electric field on the supercell i using Cartesian coordinates. Gray spheres represent metal (e.g. Sn, Hf, Ti etc.), red ones are O, green spheres are interstitial impurities (e.g. transition metals like V), and the hollow sphere is an oxygen vacancy V_o. (d) The schematic of the charge rings $\sigma_{1(2,3,4)}$ and the orbital moment directions $\vec{v}_{1(2,3,4)}$, for the four possible independent oxygen octahedral coordination of the interstitial impurities. (e) The schematic of the interaction of two adjacent interstitial impurity sites (A and B) with the nearby V_o, the resulting charge ring hybridization, and orbital moments. $\vec{v}_A$, $\vec{v}_B$, and $\vec{v}_T$ are the orbital moments of site A, site B, and the hybridization, respectively. It is assumed that V_o is closer to site A than to site B. In the right panel, the orbital moment vectors are shown with the same origin. In (a-b), the white regions in the center are hollow and no value is assigned to them.

6.5 Summary and outlook

Two transformation-magnonics based approaches for cloaking of a cylindrical non-magnetic core have been proposed. The $\bar{\gamma}$-mechanism imposes an inhomogeneous anisotropic gyromagnetic tensor in the cloaking shell, while the $\bar{M}_s$-mechanism is based on inhomogeneous and anisotropic magnetic moments. It was shown that the wavefront of the incident spin-wave remains invariant after propagating through the shell for both mechanisms, indicating that the non-magnetic cylindrical core has been invisible towards the incident magnons. The feasibility of the $\bar{\gamma}$-mechanism in the ensemble of quantum dot molecules was discussed. Functionalized defects in magnetic oxides are proposed for the feasibility of the $\bar{M}_s$-mechanism. The reported design mechanism of transformation magnonics for manipulating magnons in magnetic semiconductors or quantum dot ensembles paves an alternative way for realizing advanced functionalities such as magnonic cloaking, lensing, and concentrations, etc.

The transformation technique introduced in this chapter can be used in the future for concentrating spin waves, as it has been done for concentrating currents in Graphene and topological insulators (TI),[181,182] and light in photonic designs.[183,184] Concentrating spin waves in spatial points can be utilized as another method for focused excitations, which in turn can be used as an alternative for inducing magnetization reversal in adjacent bit matrices, with non-local excitation in larger dimensions than the targeted data bit. Figure 6-6 shows a memory concept based on using transformation magnonics for concentrating the spin wave power flow in desired spatial points. The blue dots

are functionalized such that a desired spin wave concentration is achieved by transformation of space. If the concentrated spin wave area covers a nanodot matrix, the method presented in Chapter 2 can be utilized to induce selective reversal in that matrix while other nanodot matrices remain unexcited or excited by low power spin waves.

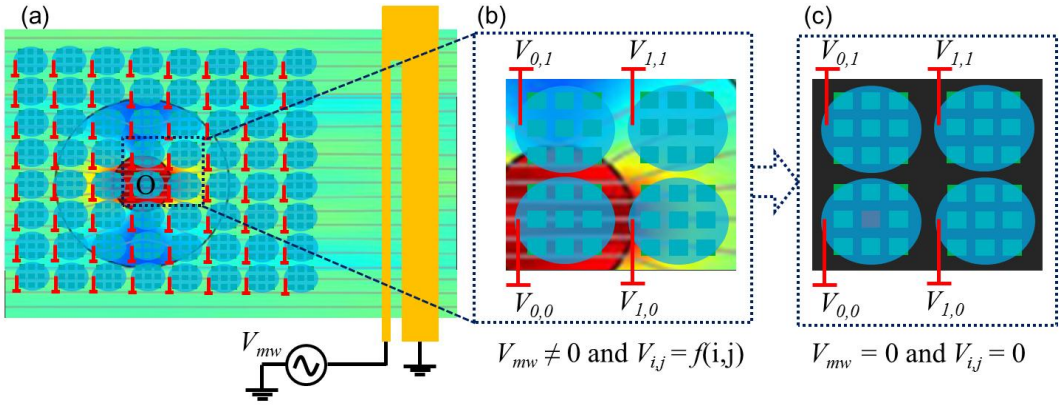

Figure 6-6. (a) Schematic of a magnetic memory proposal using concentrators based on transformation magnonics. Some parameters (e.g. Lande g-factor) of each blue dot (i,j) is controlled with a gating voltage $V_{i,j}$. The collection of blue dots determines the spin wave propagation. In (a), $V_{i,j} = f(i,j)$ can be assigned such that the power flow has a peak in a spatial point, indicated here as origin *O* (it can be any other point). The coplanar waveguide is fed by the microwave voltage V_{mw} and excites spin waves in the magnetic media. Each blue dot covers a matrix of magnetic dots used to store data in their magnetization. (b) The focused view of a boxed area in (a) while $V_{mw} \neq 0$ and $V_{i,j} = f(i,j)$ and concentration is on the nanodot matrix under blue dot (0,0) or *O*. Based on the reversal method presented in Chapter 2, the large enough spin wave can be used to selectively switch a pattern in the dot matrix. (c) An example of the reversal state in the targeted matrix, where the $V_{mw} = 0$ and $V_{i,j} = 0$ in the retention mode. In (a) and (b), the concentrator power flow color plot is adapted from ref. 184,[183] where a concentrator for optical waves based on transformation optics was demonstrated.

Chapter 7: Conclusions and future work

7.1 Conclusions

In Chapters 2 and 3, it is demonstrated how magnetostatic correlation in matrices of magnetic nanodots can be utilized to address the magnetization of individual bits by a common excitation. The method proposed in Chapter 2 can be utilized for HDD technology to go beyond its current storage capacity limitations by using existing write/read head dimensions while implementing microwave emitters of STOs. In Chapter 3, the proposed selectivity method can be applied to the MRAM technology to substantially increase the storage capacity while keeping the CMOS circuitry suitable for lower storage capacities of the current technological approach. Both the methods in Chapter 2 and Chapter 3 require microwave excitations, either as irradiation or current modulation. In Chapter 4, a method for synchronizing several STOs was proposed; the method was based on spin pumping and the recently discovered SHE and ISHE.

In Chapter 5, the fs-laser excitation was utilized to achieve AOS in magnetic transition metal/high spin-orbit scattering metal bilayers. It was shown that spin-dependent diffusive transport in the presence of SOI mechanisms can lead to ultrafast magnetization reversal if certain conditions in the parameter space are satisfied; specifically the light absorption pattern plays an important role. The specific features of this switching mechanism are that it is suitable for perpendicularly magnetized high anisotropy nanodots (main candidates for

magnetic memories), is ultrafast (tens of femtosecond), and is independent of the direction of magnetization or polarization of light.

Chapter 6 took a step beyond the existing methods for the manipulation of magnetization dynamics, and introduced transformation techniques in the thriving field of magnonics for the first time. The cloaking of a cylindrical hole with two different designs for a magnetic shell was demonstrated. Parameters such as the gyromagnetic ratio and moment were defined through tensors which were designed in order to transform space to make the environment for wave propagation as if there were no holes. It was also discussed how transformation magnonic can be extended in the future to provide an alternative memory concept.

All the proposals discussed in Chapters 2–6 will enable substantial advances in magnetic data manipulation through different flavors of excitations. All the methods have been proven by theoretical and numerical approaches, and can be used and modified based on the requirements of different applications, and should be elaborated in the context of experiments.

7.2 Future work

In the context of the different chapters of this thesis, the projected future works are to expand the possibilities enabled by the introduced transformation magnonic in Chapter 6. First, spin-metamaterial systems based on the proposals in Chapter 6, namely QD ensembles or defect engineering in magnetic oxides, should be theoretically and numerically elaborated to demonstrate the required tensors of the moment or gyromagnetic ratio. After that, other types of space transformation should be pursued to achieve applications such as spin wave

concentration, and the required spin-metamaterial systems should be designed and demonstrated.

Apart from the subjects discussed in Chapters 2–6, future work can address more futuristic types of manipulation that can be utilized for atomistic data retention through spatial scaling of spin manipulation in quantum many-body systems. Recently, manipulating the magnetization of single isolated Fe atom chains by scanning tunneling microscopy (STM) tips has been demonstrated.[314] It is therefore not far from reality that the future of magnetic data retention can involve the storage of data in the magnetization of single atoms. For the manipulation of single atom magnetization, there should be a method that can excite in atomistic dimensions, such as exciting by spin-polarized currents from STM tips. However, in the spirit of Chapters 2 and 3 of this thesis, a method that can excite in higher spatial dimension scales and yet manipulate magnetization in the atomistic level can be pursued.

The spin lattices have been a central subject of spin crystal, liquid and glass phases, and there have been studies on the effect of background curvature and geometry as a path for the manipulation of phase transitions.[315-318] Despite the recent revival of studies on geometric degrees of freedom in fractional quantum Hall (FQH) states of 2D electron gases, such studies have not been fully extended to the lattice counterpart, fractional Chern insulators, or quantum spin liquids.[319,320] The geometry of lattice and the many-body interactions can be utilized to modify the bulk-boundary correspondence and induce particular phase transitions. The objective of the future project could be to introduce negative curvature in many-body interactions on a topological band of a spin-polarized lattice to make correspondence between the boundary and bulk spatial

dimension scales. This correspondence can open up a path for atomistic control of magnetization with manipulation at larger scales down to a few nanometers.

References

1 H.-S. P. Wong, S. Raoux, S. B. Kim, J. Liang, J. P. Reifenberg, B. Rajendran, M. Asheghi, and K. E. Goodson, Proc. IEEE **98,** 2201 (2010).

2 H. Akinaga and H. Shima, Proc. IEEE **98,** 2237 (2010).

3 O. Y. Loh and H. D. Espinosa, Nat. Nanotechnol. **7,** 283 (2012).

4 Th. Gerrits, H. A. M. van den Berg, J. Hohlfeld, L.Bar, and T. Rasing, Nature **418,** 509 (2002).

5 G. Bertotti, I. Mayergoyz, and C. Serpico, *Nonlinear magnetization dynamics in nanosystems* (Elsevier Amsterdam, 2009).

6 C. Thirion, W. Wernsdorfer, and D. Mailly, Nat. Mater. **2,** 524 (2003).

7 G. Woltersdorf and C. H. Back, Phys. Rev. Lett. **99,** 227207 (2007).

8 H. T. Nembach, P. Pimentel, S. J. Hermsdoerfer, B. Leven, B. Hillebrands, and S. O. Demokritov, Appl. Phys. Lett. **90,** 062503 (2007).

9 J. Podbielski, D. Heitmann, and D. Grundler, Phys. Rev. Lett. **99,** 207202 (2007).

10 L. Lu, M. Wu, M. Mallary, G. Bertero, K. Srinivasan, R. Acharya, H. Schultheib, and A. Hoffmann, Appl. Phys. Lett. **103,** 042413 (2013).

11 M. Kammerer, H. Stoll, M. Noske, M. Sproll, M. Weigand, C. Illg, G. Woltersdorf, M. Fahnle, C. Back, and G. Schutz, Phys. Rev. B **86,** 134426 (2012).

12 T. Seki, K. Utsumiya, Y. Nozaki, H. Imamura, and K. Takanashi, Nat. Commun. **4,** 1726 (2013).

13 S. Rao, S. S. Mukherjee, M. Elyasi, C. S. Bhatia, and H. Yang, Appl. Phys. Lett. **104,** 122406 (2014).

14 G. Bertotti, C. Serpico, and I. D. Mayergoyz, Phys. Rev. Lett. **86,** 724 (2001).

15 W. Scholz and S. Batra, J. Appl. Phys. **103,** 07F539 (2008).

16 S. Okamoto, M. Furuta, N. Kikuchi, O. Kitakami, and T. Shimatsu, IEEE Trans. Magn. **50,** 3200906 (2014).

17 J. -G. Zhu, X. Zhu, and Y. Tang, IEEE Trans. Magn. **44,** 125 (2008).

18 S. Okamoto, N. Kikuchi, and O. Kitakami, Appl. Phys. Lett. **93,** 102506 (2008).

19 S. Okamoto, N. Kikuchi, and O. Kitakami, Appl. Phys. Lett. **93,** 142501 (2008).

20 R. Yanes, R. Rozada, F. García-Sánchez, O. Chubykalo-Fesenko, P. Martin Pimentel, B. Leven, and B. Hillebrands, Phys. Rev. B **79,** 224427 (2009).

21 D. Houssameddine, U. Ebels, B.Delaet, B.Rodmacq, I. Firastrau, F. Ponthenier, M. Brunet, C.Thirion, J.-P. Michel, L. Prejbeanu-Buda, M.-C. Cyrille, O. Redon, and B. Dieny, Nat. Mater. **6,** 447 (2007).

22 V. S. Pribiag, I. N. Krivorotov, G. D. Fuchs, P. M. Braganca, O. Ozatay, J. C. Sankey, D. C. Ralph, and R. A. Buhrman, Nat. Phys. **3,** 498 (2007).

23 A M. Deac, A. Fukushima, H. Kubota, H. Maehara, Y. Suzuki, S. Yuasa, Y. Nagamine, K. Tsunekawa, D. D. Djayaprawira, and N. Watanabe, Nat. Phys. **4,** 803 (2008).
24 V. E. Demidov, S. Urazhdin, H. Ulrichs, V. Tiberkevich, A. Slavin, D. Baither, G. Schmitz, and S. O. Demokritov, Nat. Mater. **11,** 1028 (2012).
25 L. Liu, C.-F. Pai, D. C. Ralph, and R. A. Buhrman, Phys. Rev. Lett. **109,** 186602 (2012).
26 I. M. Miron, K. Garello, G. Gaudin, P.-J. Zermatten, M. V. Costache, S. Auffret, S. Bandiera, B. Rodmacq, A. Schuhl, and P. Gambardella, Nature **476,** 189 (2011).
27 L. Liu, C.-F. Pai, Y. Li, H. W. Tseng, D. C. Ralph, and R. A. Buhrman, Science **336,** 555 (2012).
28 N. Locatelli, V. Cros, and J. Grollier, Nat. Mater. **13,** 11 (2013).
29 S. Ikeda, K. Miura, H. Yamamoto, K. Mizunuma, H. D. Gan, M. Endo, S. Kanai, J. Hayakawa, F. Matsukura, and H. Ohno, Nat. Mater. **9,** 721 (2010).
30 S. Mangin, D. Ravelosona, J. A. Katine, M. J. Carey, B. D. Terris, and E. E. Fullerton, Nat. Mater. **5,** 210 (2006).
31 S.-K. Kim, Y.-S. Choi, K.-S. Lee, K. Y. Guslienko, and D.-E. Jeong, Appl. Phys. Lett. **91,** 082506 (2007).
32 J. C. Slonczewski, J. Magn. Magn. Mater. **159,** L1 (1996).
33 V. E. Demidov, S. Urazhdin, H. Ulrichs, V. Tiberkevich, A. Slavin, D. Baither, G. Schmitz, and S. O. Demokritov, Nat. Mater. **11,** 1028 (2012).
34 X. Wang and A. Manchon, arXiv:1111.5466v1 [cond-mat.mtrl-sci] (2011).
35 A. Manchon, arXiv:1204.4869v1 [cond-mat.mes-hall] (2012).
36 I. M. Miron, G. Gaudin, S. Auffret, B. Rodmacq, A. Schuhl, S. Pizzini, J. Vogel, and P. Gambardella, Nat. Mater. **9,** 230 (2010).
37 N. Okamoto, H. Kurebayashi, P. Trypiniotis, I. Farrer, D. A. Ritchie, E. Saitoh, J. Sinova, J. Mašek, T. Jungwirth, and C. H. W. Barnes, Nat. Mater. **13,** 932 (2014).
38 H. Kurebayashi, J. Sinova, D. Fang, A.C. Irvine, T. D. Skinner, J. Wunderlich, V. Novak, R. P. Campion, B. L. Gallagher, E. K. Vehstedt, L. P. Zarbo, K. Vyborny, A. J. Ferguson, and T. Jungwirth, Nat. Nanotechnol. **9,** 211 (2014).
39 A. Manchon and S. Zhang, Phys. Rev. B **78,** 212405 (2008).
40 J.-H. Park, C. H. Kim, H.-W. Lee, and J. H. Han, Phys. Rev. B **87,** 041301 (2013).
41 P. M. Haney, H.-W. Lee, K.-J. Lee, A. Manchon, and M. D. Stiles, Phys. Rev. B **87,** 174411 (2013).
42 H.-A. Engel, B. I. Halperin, and E. I. Rashba, Phys. Rev. Lett. **95,** 166605 (2005).
43 J. Sinova, D. Culcer, Q. Niu, N. A. Sinitsyn, T. Jungwirth, and A. H. MacDonald, Phys. Rev. Lett. **92,** 126603 (2004).
44 E. I. Rashba, Sov. Phys. Solid State **2,** 1109 (1960).
45 E. I. Rashba, Phys. Rev. B **68,** 241315 (2003).
46 G. Dresselhaus, Phys. Rev. **100,** 580 (1955).

47 D. A. Pesin and A. H. MacDonald, Phys. Rev. B **86,** 014416 (2012).
48 N. F. Mott and H. S. W. Massey, *The theory of atomic collisions* (Oxford University Press, New York, 1965).
49 E. G. Mishchenko, A. V. Shytov, and B. I. Halperin, Phys. Rev. Lett. **93,** 226602 (2004).
50 L. Liu, C.-F. Pai, D. C. Ralph, and R. A. Buhrman, Phys. Rev. Lett. **109,** 186602 (2012).
51 R. H. Liu, W. L. Lim, and S. Urazhdin, Phys. Rev. Lett. **110,** 147601 (2013).
52 A. Chernyshov, M. Overby, X. Liu, J. K. Furdyna, Y. Lyanda-Geller, and L. P. Rokhinson, Nat. Phys. **5,** 656 (2009).
53 W. Jiang, P. Upadhyaya, W. Zhang, G. Yu, M. B. Jungfleisch, F. Y. Fradin, J. E. Pearson, Y. Tserkovnyak, K. L. Wang, O. Heinonen, S. G. E. te Velthuis, and A. Hoffmann, Science **349,** 283 (2015).
54 Z. Li and S. Zhang, Phys. Rev. Lett. **92,** 207203 (2004).
55 I. M. Miron, T. Moore, H. Szambolics, L. D. Buda-Prejbeanu, S. Auffret, B. Rodmacq, S. Pizzini, J. Vogel, M. Bonfim, A. Schuhl, and G. Gaudin, Nat. Mater. **10,** 419 (2011).
56 L. S. E. Alvarez, K.-Y. Wang, S. Lepadatu, S. Landi, S. J. Bending, and C. H. Marrows, Phys. Rev. Lett. **104,** 137205 (2010).
57 S. D. Gupta, S. Fukami, C. Zhang, H. Sato, M. Yamanouchi, F. Matsukura, and H. Ohno, Nat. Phys. **12,** 333 (2015).
58 K.-S. Ryu, L. Thomas, S.-H. Yang, and S. Parkin, Nat. Nanotechnol. **8,** 527 (2013).
59 S. S. P. Parkin, M. Hayashi, and L. Thomas, Science **320,** 190 (2008).
60 G. E. W. Bauer, E. Saitoh, and B. J. v. Wees, Nat. Mater. **11,** 391 (2012).
61 A. Slachter, F. L. Bakker, J. P. Adam, and B. J. v. Wees, Nat. Phys. **6,** 879 (2010).
62 S. Geprags, A. Kehlberger, F. D. Coletta, Z. Qiu, E.-J. Guo, T. Schulz, C. Mix, S. Meyer, A. Kamra, M. Althammer, H. Huebl, G. Jakob, Y. Ohnuma, H. Adachi, J. Barker, S. Maekawa, G. E. W. Bauer, E. Saitoh, R. Gross, S. T. B. Goennenwein, and M. Klaui, Nat. Commun. **7,** 10452 (2016).
63 D. Hinzke and U. Nowak, Phys. Rev. Lett. **107,** 027205 (2011).
64 A. B. Cahaya, O. A. Tretiakov, and G. E. W. Bauer, Appl. Phys. Lett. **104,** 042402 (2014).
65 M. Schreier, A. Kamra, M. Weiler, J. Xiao, G. E. W. Bauer, R. Gross, and S. T. B. Goennenwein, Phys. Rev. B **88,** 094410 (2013).
66 G. E. W. Bauer, S. Bretzel, A. Brataas, and Y. Tserkovnyak, Phys. Rev. B **81,** 024427 (2010).
67 Y. Kato, R. C. Myers, D. C. Driscoll, A. C. Gossard, J. Levy, and D. D. Awschalom, Science **299,** 1201 (2003).
68 T. Andlauer and P. Vogl, Phys. Rev. B **79,** 045307 (2009).
69 S.-P. Shen, Y.-S. Chai, J.-Z. Cong, P.-J. Sun, J. Lu, L.-Q. Yan, S.-G. Wang, and Y. Sun, Phys. Rev. B **90,** 180404 (2014).

70 U. Bauer, L. Yao, A. J. Tan, P. Agrawal, S. Emori, H. L. Tuller, S. van Dijken, and G. S. D. Beach, Nat. Mater. **14,** 174 (2014).
71 Y. Chen, T. Fitchorov, C. Vittoria, and V. G. Harris, Appl. Phys. Lett. **97,** 052502 (2010).
72 A. A. Kovalev, G. E. W. Bauer, and A. Brataas, Phys. Rev. B **75,** 014430 (2007).
73 J. C. Sankey, Y.-T. Cui, J. Z. Sun, J. C. Slonczewski, R. A. Buhrman, and D. C. Ralph, Nat. Phys. **4,** 67 (2007).
74 Z. Li, S. Zhang, Z. Diao, Y. Ding, X. Tang, D.M. Apalkov, Z. Yang, K. Kawabata, and Y. Huai, Phys. Rev. Lett. **100,** 246602 (2008).
75 S. Kaka, M. R. Pufall, W. H. Rippard, T. J. Silva, S. E. Russek, and J. A. Katine, Nature **437,** 389 (2005).
76 Z. Zeng, I. N. Krivorotov, G. Finocchio, Y. Huai, B. Zhang, J. Langer, P. K. Amiri, B. Azzerboni, J. A. Katine, K. L. Wang, and H. Jiang, Sci. Rep. **3,** 1426 (2013).
77 S. M. Mohseni, S. R. Sani, J. Persson, T. N. Anh Nguyen, S. Chung, Ye. Pogoryelov, P. K. Muduli, E. Iacocca, A. Eklund, R. K. Dumas, S. Bonetti, A. Deac, M. A. Hoefer, and J. Åkerman, Science **339,** 1295 (2013).
78 A. Giordano, M. Carpentieri, A. Laudani, G. Gubbiotti, B. Azzerboni, and G. Finocchio, Appl. Phys. Lett. **105,** 042412 (2014).
79 V. E. Demidov, H. Ulrichs, S. V. Gurevich, S. O. Demokritov, V. S. Tiberkevich, A. N. Slavin, A. Zholud, and S. Urazhdin, Nat. Commun. **5,** 3179 (2014).
80 Z. Duan, A. Smith, L. Yang, and B. Youngblood, Nat. Commun. **5,** 5616 (2014).
81 W. H. Rippard, M. R. Pufall, S. Kaka, T. J. Silva, S. E. Russek, and J. A. Katine, Phys. Rev. Lett. **95,** 067203 (2005).
82 A. N. Slavin and V. S. Tiberkevich, Phys. Rev. B **74,** 104401 (2006).
83 J. Grollier, V. Cros, and A. Fert, Phys. Rev. B **73,** 060409 (2006).
84 J. Persson, Y. Zhou, and J. Akerman, J. Appl. Phys. **101,** 09A503 (2007).
85 A. Ruotolo, V. Cros, B. Georges, A. Dussaux, J. Grollier, C. Deranlot, R. Guillemet, K. Bouzehouane, S. Fusil, and A. Fert, Nat. Nanotechnol. **4,** 528 (2009).
86 A. Dussaux, A. V. Khvalkovskiy, J. Grollier, V. Cros, A. Fukushima, M. Konoto, H. Kubota, K. Yakushiji, S. Yuasa, K. Ando, and A. Fert, Appl. Phys. Lett. **98,** 132506 (2011).
87 Y. Zhou, J. Persson, S. Bonetti, and J. Åkerman, Appl. Phys. Lett. **92,** 092505 (2008).
88 S. Urazhdin, P. Tabor, V. Tiberkevich, and A. Slavin, Phys. Rev. Lett. **105,** 104101 (2010).
89 V. Tiberkevich, A. Slavin, E. Bankowski, and G. Gerhart, Appl. Phys. Lett. **95,** 262505 (2009).
90 J.-Y. Bigot, M. Vomir, and E. Beaurepaire, Nat. Phys. **5,** 515 (2009).
91 G. Lefkidis, G. P. Zhang, and W. Hubner, Phys. Rev. Lett. **103,** 217401 (2009).

92 L. C. Bassett, F. J. Heremans, D. J. Christle, C. G. Yale, G. Burkard, B. B. Buckley, and D. D. Awschalom, Science **345,** 1333 (2014).
93 H. Vonesch and J.-Y. Bigot, Phys. Rev. B **85,** 180407 (2012).
94 A. J. Schellekens, K. C. Kuiper, R. R. J. C. de Wit, and B. Koopmans, Nat. Commun. **5,** 4333 (2014).
95 B. Pfau, S. Schaffert, L. Müller, C. Gutt, A. Al-Shemmary, F. Büttner, R. Delaunay, S. Düsterer, S. Flewett, R. Frömter, J. Geilhufe, E. Guehrs, C.M. Günther, R. Hawaldar, M. Hille, N. Jaouen, A. Kobs, K. Li, J. Mohanty, H. Redlin, W.F. Schlotter, D. Stickler, R. Treusch, B. Vodungbo, M. Kläui, H.P. Oepen, J. Lüning, G. Grübel, and S. Eisebitt, Nat. Commun. **3,** 1100 (2012).
96 D. Rudolf, C. La-O-Vorakiat, M. Battiato, R. Adam, J. M. Shaw, E. Turgut, P. Maldonado, S. Mathias, P. Grychtol, H. T. Nembach, T. J. Silva, M. Aeschlimann, H. C. Kapteyn, M. M. Murnane, C. M. Schneider, and P. M. Oppeneer, Nat. Commun. **3,** 1037 (2012).
97 A. Eschenlohr, M. Battiato, P. Maldonado, N. Pontius, T. Kachel, K. Holldack, R. Mitzner, A. Föhlisch, P. M. Oppeneer, and C. Stamm, Nat. Mater. **12,** 332 (2013).
98 B. Koopmans, G. Malinowski, F. D. Longa, D. Steiauf, M. Fähnle, T. Roth, M. Cinchetti, and M. Aeschlimann, Nat. Mater. **9,** 259 (2010).
99 C. Stamm, T. Kachel, N. Pontius, R. Mitzner, T. Quast, K. Holldack, S. Khan, C. Lupulescu, E. F. Aziz, M. Wietstruk, H. A. Durr, and W. Eberhardt, Nat. Mater. **6,** 740 (2007).
100 G. Malinowski, F. Dalla Longa, J. H. H. Rietjens, P. V. Paluskar, R. Huijink, H. J. M. Swagten, and B. Koopmans, Nat. Phys. **4,** 855 (2008).
101 P. Nemec, E. Rozkotová, N. Tesarova, F. Trojánek, E. De Ranieri, K. Olejník, J. Zemen, V. Novák, M. Cukr, P. Malý, and T. Jungwirth, Nat. Phys. **8,** 411 (2012).
102 K. Carva, M. Battiato, D. Legut, and P. M. Oppeneer, Phys. Rev. B **87,** 184425 (2013).
103 M. Battiato, K. Carva, and P. M. Oppeneer, Phys. Rev. B **86,** 024404 (2012).
104 M. Krauß, T. Roth, S. Alebrand, D. Steil, M. Cinchetti, M. Aeschlimann, and H. C. Schneider, Phys. Rev. B **80,** 180407 (2009).
105 S. Essert and H. C. Schneider, Phys. Rev. B **84,** 224405 (2011).
106 E. Turgut, C. La-o-vorakiat, J. M. Shaw, P. Grychtol, H. T. Nembach, D. Rudolf, R. Adam, M. Aeschlimann, C. M. Schneider, T. J. Silva, M. M. Murnane, H. C. Kapteyn, and S. Mathias, Phys. Rev. Lett. **110,** 197201 (2013).
107 M. Battiato, K. Carva, and P. M. Oppeneer, Phys. Rev. Lett. **105,** 027203 (2010).
108 G. P. Zhang, Phys. Rev. Lett. **101,** 187203 (2008).
109 A. Kirilyuk, A. V. Kimel, and T. Rasing, Rev. Mod. Phys. **82,** 2732 (2010).
110 J. Barker, U. Atxitia, T. A. Ostler, O. Hovorka, O. Chubykalo-Fesenko, and R. W. Chantrell, Sci. Rep. **3,** 3262 (2013).

111 G.-M. Choi, B.-C. Min, K.-J. Lee, and D. G. Cahill, Nat. Commun. **5,** 4334 (2014).
112 J.-Y. Bigot , M. Vomir, L. H. F. Andrade, and E. Beaurepaire, Chem. Phys. **318,** 137 (2005).
113 B. Y. Mueller, T. Roth, M. Cinchetti, M. Aeschlimann, and B. Rethfeld, New J. Phys. **13,** 123010 (2011).
114 B. Y. Mueller and B. Rethfeld, Phys. Rev. B **87,** 035139 (2013).
115 E. Carpene, E. Mancini, C. Dallera, M. Brenna, E. Puppin, and S. D. Silvestri, Phys. Rev. B **78,** 174422 (2008).
116 B. Y. Mueller, A. Baral, S. Vollmar, M. Cinchetti, M. Aeschlimann, H. C. Schneider, and B. Rethfeld, Phys. Rev. Lett. **111,** 167204 (2013).
117 K. Carva, M. Battiato, and P. M. Oppeneer, Phys. Rev. Lett. **107,** 207201 (2011).
118 K. Vahaplar, A. M. Kalashnikova, A. V. Kimel, D. Hinzke, U. Nowak, R. Chantrell, A. Tsukamoto, A. Itoh, A. Kirilyuk, and T. Rasing, Phys. Rev. Lett. **103,** 117201 (2009).
119 C. -H. Lambert, S. Mangin, B. S. D. Ch. S. Varaprasad, Y. K. Takahashi, M. Hehn, M. Cinchetti, G. Malinowski, K. Hono, Y. Fainman, M. Aeschlimann, and E. E. Fullerton, Science **345,** 1337 (2014).
120 L. Le Guyader, M. Savoini, S. El Moussaoui1, M. Buzzi, A. Tsukamoto, A. Itoh, A. Kirilyuk, T. Rasing, A. V. Kimel, and F. Nolting, Nat. Commun. **6,** 5839 (2015).
121 C. E. Graves, A. H. Reid, T. Wang, B. Wu, S. de Jong, K. Vahaplar, I. Radu, D. P. Bernstein, M. Messerschmidt, L. Müller, R. Coffee, M. Bionta, S.W. Epp, R. Hartmann, N. Kimmel, G. Hauser, A. Hartmann, P. Holl, H. Gorke, J. H. Mentink, A. Tsukamoto, A. Fognini, J. J. Turner, W. F. Schlotter, D. Rolles, H. Soltau, L. Strüder, Y. Acremann, A. V. Kimel, A. Kirilyuk, T. Rasing, J. Stöhr, A.O. Scherz, and H. A. Dürr, Nat. Mater. **12,** 293 (2013).
122 S. Mangin, M. Gottwald, C. -H. Lambert, D. Steil, V. Uhlíř, L. Pang, M. Hehn, S. Alebrand, M. Cinchetti, G. Malinowski, Y. Fainman, M. Aeschlimann, and E. E. Fullerton, Nat. Mater. **13,** 286 (2014).
123 M. Deb, M. Vomir, J.-L. Rehspringer, and J.-Y. Bigot, Appl. Phys. Lett. **107,** 252404 (2015).
124 R. Chimata, L. Isaeva, K. Kadas, A. Bergman, B. Sanyal, J. H. Mentink, M. I. Katsnelson, T. Rasing, A. Kirilyuk, A. Kimel, O. Eriksson, and M. Pereiro, Phys. Rev. B **92,** 094411 (2015).
125 J. H. Mentink, J. Hellsvik, D. V. Afanasiev, B. A. Ivanov, A. Kirilyuk, A. V. Kimel, O. Eriksson, M. I. Katsnelson, and T. Rasing, Phys. Rev. Lett. **108,** 057202 (2012).
126 T. A. Ostler, J. Barker, R. F. L. Evans, R. W. Chantrell, U. Atxitia, O. Chubykalo-Fesenko, S. El Moussaoui, L. Le Guyader, E. Mengotti, L. J. Heyderman, F. Nolting, A. Tsukamoto, A. Itoh, D. Afanasiev, B. A. Ivanov, A. M. Kalashnikova, K. Vahaplar, J. Mentink, A. Kirilyuk, T. Rasing, and A. V. Kimel, Nat. Commun. **3,** 666 (2012).

127 T. D. Cornelissen, R. Córdoba, and B. Koopmans, Appl. Phys. Lett. **108,** 142405 (2016).
128 A. Kamra, H. Keshtgar, P. Yan, and G. E. W. Bauer, Phys. Rev. B **91,** 104409 (2015).
129 K. Shen and G. E. W. Bauer, Phys. Rev. Lett. **115,** 197201 (2015).
130 I. Radu, K. Vahaplar, C. Stamm, T. Kachel, N. Pontius, H. A. Dürr, T. A. Ostler, J. Barker, R. F. L. Evans, R. W. Chantrell, A. Tsukamoto, A. Itoh, A. Kirilyuk, Th. Rasing, and A. V. Kimel, Nature **472,** 205 (2011).
131 S. Tacchi, F. Montoncello, M. Madami, G. Gubbiotti, G. Carlotti, L. Giovannini, R. Zivieri, F. Nizzoli, S. Jain, A. O. Adeyeye, and N. Singh, Phys. Rev. Lett. **107,** 127204 (2011).
132 G. Malinowski, K. C. Kuiper, R. Lavrijsen, H. J. M. Swagten, and B. Koopmans, Appl. Phys. Lett. **94,** 102501 (2009).
133 T. Kampfrath, M. Battiato, P. Maldonado, G. Eilers, J. Notzold, S. Mahrlein, V. Zbarsky, F. Freimuth, Y. Mokrousov, S. Blugel, M. Wolf, I. Radu, P. M. Oppeneer, and M. Munzenberg, Nat. Nanotechnol. **8,** 256 (2013).
134 Z. Jin, A. Tkach, F. Casper, V. Spetter, H. Grimm, A. Thomas, T. Kampfrath, M. Bonn, M. Klaui, and D. Turchinovich, Nat. Physics **11,** 761 (2015).
135 T. J. Huisman, R. V. Mikhaylovskiy, J. D. Costa, F. Freimuth, E. Paz, J. Ventura, P. P. Freitas, S. Blügel, Y. Mokrousov, Th. Rasing, and A. V. Kimel, Nat. Nanotechnol. **11,** 455 (2016).
136 Y. Wu, M. Elyasi, X. Qiu, Y. Liu, M. Chen, L. Ke, and H. Yang, Submitted to Adv. Mat. (2016).
137 M. Krawczyk and D. Grundler, J. Phys.: Condens. Mater. **26,** 123202 (2014).
138 J. H. Kwon, S. S. Mukherjee, P. Deorani, M. Hayashi, and H. Yang, Appl. Phys. A **111,** 369 (2013).
139 M. Jamali, J. H. Kwon, S.-M. Seo, K.-J. Lee, and H. Yang, Sci. Rep. **3,** 3160 (2013).
140 A. V. Chumak, A. A. Serga, and B. Hillebrands, Nat. Commun. **5,** 4700 (2014).
141 A. V. Chumak, V. S. Tiberkevich, A. D. Karenowska, A. A. Serga, J. F. Gregg, A. N. Slavin, and B. Hillebrands, Nat. Commun. **1,** 141 (2010).
142 S. O. Demokritov, V. E. Demidov, O. Dzyapko, G. A. Melkov, A. A. Serga, B. Hillebrands, and A. N. Slavin, Nature **443,** 430 (2006).
143 B. D. Terris and T. Thomson, J. Phys. D: Appl. Phys. **38** R199 (2005).
144 V. V. Kruglyak, A. Barman, R. J. Hicken, J. R. Childress, and J. A. Katine, Phys. Rev. B **71,** 220409 (2005).
145 B. Lenk, H. Ulrichs, F. Garbs, and M. Münzenberg, Phys. Rep. **507,** 107 (2011).
146 K. Y. Guslienko, Appl. Phys. Lett. **75,** 394 (1999).
147 G. N. Kakazei, P. E. Wigen, K. Yu. Guslienko, V. Novosad, A. N. Slavin, V. O. Golub, N. A. Lesnik, and Y. Otani, Appl. Phys. Lett. **85,** 443 (2004).

148 A. Yu. Galkin, B. A. Ivanov, and C. E. Zaspel, Phys. Rev. B **74,** 144419 (2006).
149 A. Vogel, M. Martens, M. Weigand, and G. Meier, Appl. Phys. Lett. **99,** 042506 (2011).
150 R. Verba, G. Melkov, V. Tiberkevich, and A. N. Slavin, Phys. Rev. B **85,** 014427 (2012).
151 R. Verba, V. Tiberkevich, K. Yu. Guslienko, G. Melkov, and A. N. Slavin, Phys. Rev. B **87,** 134419 (2013).
152 S. Saha, R. Mandal, S. Barman, D. Kumar, B. Rana, Y. Fukuma, S. Sugimoto, Y. Otani, and A. Barman, Adv. Func. Mater. **23,** 2378 (2013).
153 A. V. Chumak, V. I. Vasyuchka, A. A. Serga, and B. Hillebrands, Nat. Phys. **11,** 453 (2015).
154 J. Ding, M. Kostylev, and A. O. Adeyeye, Phys. Rev. Lett. **107,** 047205 (2011).
155 K. Di, V. L. Zhang, M. H. Kuok, H. S. Lim, S. C. Ng, K. Narayanapillai, and H. Yang, Phys. Rev. B **90,** 060405 (2014).
156 A. J. Bennett, Nat. Commun. **4,** 1522 (2013).
157 J. R. Petta, A. C. Johnson, J. M. Taylor, E. A. Laird, A. Yacoby, M. D. Lukin, C. M. Marcus, M. P. Hanson, and A. C. Gossard, Science **309,** 2180 (2005).
158 W. Chen, J. Hu, Y. Duan, B. Braverman, H. Zhang, and V. Vuletić, Phys. Rev. Lett. **115,** 250502 (2015).
159 M. Pioro-Ladrière, T. Obata, Y. Tokura, Y.-S. Shin, T. Kubo, K. Yoshida, T. Taniyama, and S. Tarucha, Nat. Phys. **4,** 776 (2008).
160 S. Gangadharaiah, J. Sun, and O. A. Starykh, Phys. Rev. Lett. **100,** 156402 (2008).
161 J. R. Petta and D. C. Ralph, Phys. Rev. Lett. **89,** 156802 (2002).
162 F. Baruffa, P. Stano, and J. Fabian, Phys. Rev. Lett. **104,** 126401 (2010).
163 M. P. Nowak, B. Szafran, F. M. Peeters, B. Partoens, and W. J. Pasek, Phys. Rev. B **83,** 245324 (2011).
164 G. Salis, Y. Kato, K. Ensslin, D. C. Driscoll, A.C. Gossard, and D. D. Awschalom, Nature **414,** 619 (2001).
165 S. Takahashi, R. S. Deacon, K. Yoshida, A. Oiwa, K. Shibata, K. Hirakawa, Y. Tokura, and S. Tarucha, Phys. Rev. Lett. **104,** 246801 (2010).
166 J. Simon, H. Tanji, S. Ghosh, and V. Vuletic, Nature **3,** 765 (2007).
167 E. Barnes, D.-L. Deng, R. E. Throckmorton, Y.-L. Wu, and S. D. Sarma, Phys. Rev. B **93,** 95420 (2016).
168 Z.-L. Xiang, S. Ashhab, J. Q. You, and F. Nori, Rev. Mod. Phys. **85,** 623 (2013).
169 R. Hisatomi, A. Osada, Y. Tabuchi, T. Ishikawa, A. Noguchi, R. Yamazaki, K. Usami, and Y. Nakamura, arXiv:1601.03908v2 (2016).
170 Y. Tabuchi, S. Ishino, T. Ishikawa, R. Yamazaki, K. Usami, and Y. Nakamura, Phys. Rev. Lett. **113,** 083603 (2014).

171 C. Grezes, B. Julsgaard, Y. Kubo, W. L. Ma, M. Stern, A. Bienfait, K. Nakamura, J. Isoya, S. Onoda, T. Ohshima, V. Jacques, D. Vion, D. Esteve, R. B. Liu, K. Mølmer, and P. Bertet, Phys. Rev. A **92,** 020301 (2015).
172 C. Grezes, Y. Kubo, B. Julsgaard, T. Umeda, J. Isoya, H. Sumiya, H. Abe, S. Onoda, T. Ohshima, K. Nakamura, I. Diniz, A. Auffeves, V. Jacques, J.-F. Roch, D. Vion, D. Esteve, K. Mølmer, and P. Bertet, arXiv:1510.06565v1 (2015).
173 Y. Tabuchi, S. Ishino, A. Noguchi, T. Ishikawa, R. Yamazaki, K. Usami, and Y. Nakamura, arXiv:1508.05290v1 (2015).
174 Y. Tabuchi, S. Ishino, A. Noguchi, T. Ishikawa, R. Yamazaki, K. Usami, and Y. Nakamura, Science **349,** 405 (2015).
175 S. Depenbrock, I. P. McCulloch, and U. Schollwock, Phys. Rev. Lett. **109,** 067201 (2012).
176 S. Yan, D. A. Huse, and S. R. White, Science **332,** 1173 (2011).
177 L. Balents, Nature **464,** 199 (2010).
178 H.-C. Jiang, Z. Wang, and L. Balents, Nat. Phys. **8,** 902 (2012).
179 C. Nayak, S. H. Simon, A. Stern, M. Freedman, and S. D. Sarma, Rev. Mod. Phys. **80,** 1083 (2008).
180 C. Castelnovo, R. Moessner, and S. L. Sondhi, Nature **451,** 42 (2008).
181 L. Zhao, P. Tang, B.-L. Gu, and W. Duan, Phys. Rev. Lett. **111,** 116601 (2013).
182 V. V. Cheianov, V. Fal'ko, and B. L. Altshuler, Science **315,** 1252 (2007).
183 M. Rahm, D. Schurig, D. A. Roberts, S. A. Cummer, D. R. Smith, and J. B. Pendry, Phot. Nano. Fund. Appl. **6,** 87 (2008).
184 M. Yan, W. Yan, and M. Qiu, Phys. Rev. B **78,** 125113 (2008).
185 A. S. Kovalev and J. E. Prilepsky, Low Temp. Phys. **28,** 921 (2002).
186 J. Shibata and Y. Otani, Phys. Rev. B **70,** 012404 (2004).
187 B. Pigeau, G. de Loubens, O. Klein, A. Riegler, F. Lochner, G. Schmidt, L. W. Molenkamp, V. S. Tiberkevich, and A. N. Slavin, Appl. Phys. Lett. **96,** 132506 (2010).
188 S. Jain, V. Novosad, F. Y. Fradin, J. E. Pearson, V. Tiberkevich, A. N. Slavin, and S. D. Bader, Nat. Commun. **3,** 1330 (2012).
189 C. F. Adolff, M. Hanze, A. Vogel, M. Weigand, M. Martens, and G. Meier, Phys. Rev. B **88,** 224425 (2013).
190 M. Igarashi, K. Watanabe, Y. Hirayama, and Y. Shiroishi, IEEE Trans. Magn. **48,** 3284 (2012).
191 J.-U. Thiele, L. Folks, M. F. Toney, and D. K. Weller, J. Appl. Phys. **84,** 5686 (1998).
192 M. Beleggiaa, S. Tandonb, Y. Zhua, and M. D. Graef, J. Magn. Magn. Mater. **278,** 270 (2004).
193 T. Tanaka, Y. Otsuka, Y. Furomoto, K. Matsuyama, and Y. Nozaki, J. Appl. Phys. **113,** 143908 (2013).
194 S. L. Zhang, J. Y. Zhang, and T. Hesjedal, Sci. Rep. **4,** 61109 (2014).
195 D. Charrier, S. Capponi, M. Oshikawa, and P. Pujol, Phys. Rev. B **82,** 075108 (2010).

196 F. Pollmann, E. Berg, A. M. Turner, and M. Oshikawa, Phys. Rev. B **85,** 075125 (2012).
197 F. D. M. Haldane, Phys. Rev. Lett. **50,** 1153 (1983).
198 P. A. Ivanov, N. I. Karchev, N. V. Vitanov, and D. G. Angelakis, Phys. Rev. A **90,** 012325 (2014).
199 B. Lenk, H. Ulrichs, F. Garbs, and M. Münzenberg, Phys. Rep. **507,** 107 (2011).
200 M. Krawczyk and D. Grundler, J. Phys.: Condens. Matter **26,** 123202 (2014).
201 R. P. Tiwari and D. Stroud, Phys. Rev. B **81,** 220403(R) (2010).
202 R. Verba, G. Melkov, V. Tiberkevich, and A. N. Slavin, Phys. Rev. B **85,** 014427 (2012).
203 S. Saha, R. Mandal, S. Barman, D. Kumar, B. Rana, Y. Fukuma, S. Sugimoto, Y. Otani, and A. Barman, Adv. Func. Mater. **23,** 2378 (2013).
204 S. Jain, V. Novosad, F. Y. Fradin, J. E. Pearson, V. Tiberkevich, A. N. Slavin, and S. D. Bader, Nat. Commun. **3,** 1330 (2012).
205 C. F. Adolff, M. Hanze, A. Vogel, M. Weigand, M. Martens, and G. Meier, Phys. Rev. B **88,** 224425 (2013).
206 M. Elyasi, C. S. Bhatia, and H. Yang, Sci. Rep. **5,** 7908 (2015).
207 Q. Stainer, L. Lombard, K. Mackay, D. Lee, S. Bandiera, C. Portemont, C. Creuzet, R. C. Sousa, and B. Dieny, Appl. Phys. Lett. **105,** 032405 (2014).
208 X. Lou, Z. Gao, D. V. Dimitrov, and M. X. Tang, Appl. Phys. Lett. **93,** 242502 (2008).
209 A. Dussaux, A. V. Khvalkovskiy, J. Grollier, V. Cros, A. Fukushima, M. Konoto, H. Kubota, K. Yakushiji, S. Yuasa, K. Ando, and A. Fert, Appl. Phys. Lett. **98,** 132506 (2011).
210 J. Grollier, V. Cros, and A. Fert, Phys. Rev. B **73,** 060409 (2006).
211 V. E. Demidov, H. Ulrichs, S. V. Gurevich, S. O. Demokritov, V. S. Tiberkevich, A. N. Slavin, A. Zholud, and S. Urazhdin, Nat. Commun. **5,** 3179 (2014).
212 A. N. Slavin and V. S. Tiberkevich, IEEE Trans. Magn. **45,** 1875 (2009).
213 A. N. Slavin and V. S. Tiberkevich, Phys. Rev. B **72,** 092407 (2005).
214 M. Elyasi, C. S. Bhatia, and H. Yang, J. Appl. Phys. **117,** 063907 (2015).
215 J. E. Hirsch, Phys. Rev. Lett. **83,** 1834 (1999).
216 T. Kimura, Y. Otani, T. Sato, S. Takahashi, and S. Maekawa, Phys. Rev. Lett. **98,** 156601 (2007).
217 O. Mosendz, J. E. Pearson, F. Y. Fradin, G. E. W. Bauer, S. D. Bader, and A. Hoffmann, Phys. Rev. Lett. **104,** 046601 (2010).
218 C. Hahn, G. de Loubens, M. Viret, O. Klein, V.V. Naletov, and J. B. Youssef, Phys. Rev. Lett. **111,** 217204 (2013).
219 L. Liu, T. Moriyama, D. C. Ralph, and R. A. Buhrman, Phys. Rev. Lett. **106,** 036601 (2011).
220 P. Deorani and H. Yang, Appl. Phys. Lett. **103,** 232408 (2013).
221 A. Ganguly, K. Kondou, H. Sukegawa, S. Mitani, S. Kasai, Y. Niimi, Y. Otani, and A. Barman, Appl. Phys. Lett. **104,** 072405 (2014).

222 A. Ganguly, R. M. Rowan-Robinson, A. Haldar, S. Jaiswal, J. Sinha, A. T. Hindmarch, D. A. Atkinson, and A. Barman, Appl. Phys. Lett. **105,** 112409 (2014).
223 Y. Wang, P. Deorani, X. Qiu, J. H. Kwon, and H. Yang, Appl. Phys. Lett. **105,** 152412 (2014).
224 M. Jamali, K. Narayanapillai, X. Qiu, L. M. Loong, A. Manchon, and H. Yang, Phys. Rev. Lett. **111,** 246602 (2013).
225 X. Qiu, P. Deorani, K. Narayanapillai, K.-S. Lee, K.-J. Lee, H.-W. Lee, and H. Yang, Sci. Rep. **4,** 4491 (2014).
226 Y. Zhou and J. Åkerman, Appl. Phys. Lett. **94,** 112503 (2009).
227 B. A. Kalinikos, N. G. Kovshikov, and C. E. Patton, Phys. Rev. Lett. **80,** 4301 (1998).
228 M. M. Scott, B. A. Kalinikos, and C. E. Patton, Appl. Phys. Lett. **78,** 970 (2001).
229 J. Stoer and R. Bulirsch, *Introduction to Numerical Analysis*, 2nd ed. (Springer, New York, 1993).
230 D. V. Berkov, Phys. Rev. B **87,** 014406 (2013).
231 S. I. Kiselev, J. C. Sankey, I. N. Krivorotov, N. C. Emley, R. J. Schoelkopf, R. A. Buhrman , and D. C. Ralph, Nature **425,** 380 (2003).
232 A. Slavin and V. Tiberkevich, IEEE Trans. Magn. **45,** 1875 (2009).
233 C. -F. Pai, L. Liu, Y. Li, H. W. Tseng, D. C. Ralph, and R. A. Buhrman, Appl. Phys. Lett. **101,** 122404 (2012).
234 M. Bauer, A. Marienfeld, and M. Aeschlimann, Progress in Surface Science **90,** 319 (2015).
235 V. P. Zhukov, E. V. Chulkov, and P. M. Echenique, Phys. Rev. B **72,** 155109 (2005).
236 V. P. Zhukov, E. V. Chulkov, and P. M. Echenique, Phys. Rev. B **73,** 125105 (2006).
237 F. Freimuth, S. Blugel, and Y. Mokrousov, Phys. Rev. B **90,** 174423 (2014).
238 P. M. Oppeneer and A. Liebsch, J. Phys.: Condens. Matter **16,** 5519 (2004).
239 T. Moriya, Phys. Rev. A **120,** 91 (1960).
240 I. Dzyaloshinskii, Phys. Chem. Solids **4,** 241 (1958).
241 J. Bass and W. P. P. Jr, J. Phys.: Condens. Matter **19,** 183201 (2007).
242 A. Santoni and F. J. Himpsel, Phys. Rev. B **43,** 1305 (1991).
243 C.-F. Pai, L. Liu, Y. Li, H. W. Tseng, D. C. Ralph, and R. A. Buhrman, Appl. Phys. Lett. **101,** 122404 (2012).
244 Y. Niimi, Y. Kawanishi, D. H. Wei, C. Deranlot, H. X. Yang, M. Chshiev, T. Valet, A. Fert, and Y. Otani, Phys. Rev. Lett. **109,** 156602 (2012).
245 A. Alù and N. Engheta, Phys. Rev. E **72,** 016623 (2005).
246 B. Liao, M. Zebarjadi, K. Esfarjani, and G. Chen, Phys. Rev. Lett. **109,** 126806 (2012).
247 D. Schurig, J. J. Mock, B. J. Justice, S. A. Cummer, J. B. Pendry, A. F. Starr, and D. R. Smith, Science **314,** 977 (2006).

248 F. Gömöry, M. Solovyov, J. Šouc, C. Navau, J. P.-Camps, and A. Sanchez, Science **335,** 1466 (2012).
249 G. W. Milton, M. Briane, and J. R. Willis, New J. Phys. **8,** 248 (2006).
250 J. B. Pendry, D. Schurig, and D. R. Smith, Science **312,** 1780 (2006).
251 N.-A. P. Nicorovici, G. W. Milton, R. C. McPhedran, and L. C. Botten, Optic Express **15,** 6314 (2007).
252 S. A. Cummer and D. Schurig, New J. Phys. **9,** 45 (2007).
253 S. Zhang, D. A. Genov, C. Sun, and X. Zhang, Phys. Rev. Lett. **100,** 123002 (2008).
254 T. Han, X. Bai, D. Gao, J. T. L. Thong, B. Li, and C.-W. Qiu, Phys. Rev. Lett. **112,** 054302 (2014).
255 U. Leonhardt and T. G. Philbin, New J. Phys. **8,** 247 (2006).
256 W. Cai, U. K. Chettiar, A. V. Kildishev, and V. M. Shalaev, Nat. Photon. **1,** 224 (2007).
257 W. Cai, U. K. Chettiar, A. V. Kildishev, V. M. Shalaev, and G. W. Milton, Appl. Phys. Lett. **91,** 111105 (2007).
258 S. A. Cummer, B.-I. Popa, D. Schurig, D. R. Smith, J. Pendry, M. Rahm, and A. Starr, Phys. Rev. Lett. **100,** 024301 (2008).
259 A. Diatta and S. Guenneau, Appl. Phys. Lett. **105,** 021901 (2014).
260 M. Farhat, S. Guenneau, and S. Enoch, Phys. Rev. B **85,** 020301 (2012).
261 A. Sanchez, C. Navau, J. P.-Camps, and D.-X. Chen, New J. Phys. **13,** 093034 (2011).
262 T. Han, H. Ye, Y. Luo, S. P. Yeo, J. Teng, S. Zhang, and C.-W. Qiu, Adv. Mater. **26,** 3478 (2014).
263 B. Zhang, Y. Luo, X. Liu, and G. Barbastathis, Phys. Rev. Lett. **106,** 033901 (2011).
264 N. Gu, M. Rudner, and L. Levitov, Phys. Rev. Lett. **107,** 156603 (2011).
265 S.-K. Kim, S. Choi, K.-S. Lee, D.-S. Han, D.-E. Jung, and Y.-S. Choi, Appl. Phys. Lett. **92,** 212501 (2008).
266 L. Zhang, J. Ren, J.-S. Wang, and B. Li, Phys. Rev. Lett. **105,** 225901 (2010).
267 A. Mook, U. Henk, and I. Mertig, Phys. Rev. B **91,** 174409 (2015).
268 R. Shindou, R. Matsumoto, S. Murakami, and J.-I. Ohe, Phys. Rev. B **87,** 174427 (2013).
269 A. B. Khanikaev, S. H. Mousavi, W.-K. Tse, M. Kargarian, A. H. MacDonald, and G. Shvets, Nat. Mater. **12,** 233 (2012).
270 B. A. Kalinikos and A. N. Slavin, J. Phys. C: Solid State Phys. **19,** 7013 (1986).
271 M. P. Kostylev, G. Gubbiotti, J.-G. Hu, G. Carlotti, T. Ono, and R. L. Stamps, Phys. Rev. B **76,** 054422 (2007).
272 A. Trueba, P. Garcia-Fernandez, F. Senn, C. A. Daul, J. A. Aramburu, M. T. Barriuso, and M. Moreno, Phys. Rev. B **81,** 075107 (2010).
273 G. Cucinotta, M. Perfetti, J. Luzon, M. Etienne, P.-E. Car, A. Caneschi, G. Calvez, K. Bernot, and R. Sessoli, Angew. Chem. **51,** 1606 (2012).

274 H. J. Krenner, M. Sabathil, E. C. Clark, A. Kress, D. Schuh, M. Bichler, G. Abstreiter, and J. J. Finley, Phys. Rev. Lett. **94,** 057402 (2005).
275 W. Sheng and J.-P. Leburton, Phys. Rev. Lett. **88,** 167401 (2002).
276 R. Roloff, W. Potz, T. Eissfeller, and P. Vogl, arXiv **1003.0897v1** (2010).
277 D. Loss and D. P. DiVincenzo, Phys. Rev. A **57,** 120 (1998).
278 E. A. Stinaff, M. Scheibner, A. S. Bracker, I. V. Ponomarev, V. L. Korenev, M. E. Ware, M. F. Doty, T. L. Reinecke, and D. Gammon, Science **311,** 636 (2006).
279 T. P. Mayer Alegre, F. G. G. Hernandez, A. L. C. Pereira, and G. Medeiros-Ribeiro, Phys. Rev. Lett. **97,** 236402 (2006).
280 V. Jovanov, T. Eissfeller, S. Kapfinger, E. C. Clark, F. Klotz, M. Bichler, J. G. Keizer, P. M. Koenraad, G. Abstreiter, and J. J. Finley, Phys. Rev. B **83,** 161303 (2011).
281 M. T. Björk, A. Fuhrer, A. E. Hansen, M. W. Larsson, L. E. Fröberg, and L. Samuelson, Phys. Rev. B **72,** 201307(R) (2005).
282 A. J. Bennett, M. A. Pooley, Y. Cao, N. Skold, I. Farrer, D. A. Ritchie, and A. J. Shields, Nat. Commun. **4,** 1522 (2013).
283 Y.-P. Shim, S. Oh, X. Hu, and M. Friesen, Phys. Rev. Lett. **106,** 180503 (2011).
284 C. Lü, J. L. Cheng, and M. W. Wu, Phys. Rev. B **71,** 075308 (2005).
285 B.Shao, Y.-F. He, M. Feng, Y. Lu, and X. Zuo, J. Appl. Phys. **115,** 17A915 (2014).
286 D. Y. Li, Y. J. Zeng, L. M. C. Pereira, D. Batuk, J. Hadermann, Y. Z. Zhang, Z. Z. Ye, K. Temst, A. Vantomme, M. J. V. Bael, and C. V. Haesendonck, J. Appl. Phys. **114,** 033909 (2013).
287 J. H. Buß, J. Rudolph, F. Natali, F. Semond, and D. Hägele, Appl. Phys. Lett. **95,** 192107 (2009).
288 J. Lee, A. Venugopal, and V. Sih, Appl. Phys. Lett. **106,** 012403 (2015).
289 J. Zhang, R. Skomski, Y. F. Lu, and D. J. Sellmyer, Phys. Rev. B **75,** 214417 (2007).
290 K. V. Kavokin, Phys. Rev. B **64,** 075305 (2001).
291 K. V. Kavokin, Phys. Rev. B **69,** 075302 (2004).
292 L. P. Gor'kov and P. L. Krotkov, Phys. Rev. B **67,** 033203 (2003).
293 M. Venkatesan, C. B. Fitzgerald, J. G. Lunney, and J. M. D. Coey, Phys. Rev. Lett. **93,** 177206 (2004).
294 Rui Li and J. Q. You, Phys. Rev. B **90,** 035303 (2014).
295 M. I. Dyakonov and V. Y. Kachorovskii, Sov. Phys. Semicond. **20,** 110 (1986).
296 Y. Yamada, K. Ueno, T. Fukumura, H. T. Yuan, H. Shimotani, Y. Iwasa, L. Gu, S. Tsukimoto, Y. Ikuhara, and M. Kawasaki, Science **332,** 1065 (2011).
297 S. B. Ogale, Adv. Mater. **22,** 3125 (2010).
298 A. Jesche, R. W. McCallum, S. Thimmaiah, J. L. Jacobs, V. Taufour, A. Kreyssig, R. S. Houk, S. L. Budko, and P. C. Canfiel, Nat. Commun. **5,** 3333 (2014).

299 L.-Te Chang, C.-Yen Wang, J. Tang, T. Nie, W. Jiang, C.-Pu Chu, S. Arafin, L. He, M. Afsal, L.-J. Chen, and K. L. Wang, Nano Lett. **14,** 1823 (2014).
300 K. Yang, R. Wu, L. Shen, Y. P. Feng, Y. Dai, and B. Huang, Phys. Rev. B **81,** 125211 (2010).
301 P. Liu, S. Khmelevskyi, B. Kim, M. Marsman, D. Li, X.-Qiu Chen, D. D. Sarma, G. Kresse, and C. Franchini, Phys. Rev. B **92,** 054428 (2015).
302 G. Mattioli, F. Filippone, P. Alippi, and A. A. Bonapasta, Phys. Rev. B **78,** 241201 (2008).
303 H. Wu, A. Stroppa, S. Sakong, S. Picozzi, M. Scheffler, and P. Kratzer, Phys. Rev. Lett. **105,** 267203 (2010).
304 T. S. Herng, D.-C. Qi, T. Berlijn, J. B. Yi, K. S. Yang, Y. Dai, Y. P. Feng, I. Santoso, C. S.-Hanke, X. Y. Gao, A. T. S. Wee, W. Ku, J. Ding, and A. Rusydi, Phys. Rev. Lett. **105,** 207201 (2010).
305 X. Du, Q. Li, H. Su, and J. Yang, Phys. Rev. B **74,** 233201 (2006).
306 I. S. Elfimov, A. Rusydi, S. I. Csiszar, Z. Hu, H. H. Hsieh, H.-J. Lin, C.T. Chen, R. Liang, and G. A. Sawatzky, Phys. Rev. Lett. **98,** 137202 (2007).
307 K. Sato, L. Bergqvist, J. Kudrnovsky, P. H. Dederichs, O. Eriksson, I. Turek, B. Sanyal, G. Bouzerar, H. K.-Yoshida, V. A. Dinh, T. Fukushima, H. Kizaki, and R. Zeller, Rev. Mod. Phys. **82,** 1633 (2010).
308 K. Yang, Y. Dai, B. Huang, and Y. P. Feng, Phys. Rev. B **81,** 033202 (2010).
309 J. M. D. Coey, M. Venkatesan, and C. B. Fitzgerald, Nature **4,** 173 (2005).
310 H. Raebiger, S. Lany, and A. Zunger, Phys. Rev. Lett. **101,** 027203 (2008).
311 R. Janisch and N. A. Spaldin, Phys. Rev. B **73,** 035201 (2006).
312 P. Novak and F. R. Wagner, Phys. Rev. B **66,** 184434 (2002).
313 J. M. D. Coey, M. Venkatesan, P. Stamenov, C. B. Fitzgerald, and L. S. Dorneles, Phys. Rev. B **72,** 024450 (2005).
314 S. Loth, S. Baumann, C. P. Lutz, D. M. Eigler, and A. J. Heinrich, Science **335,** 196 (2012).
315 Y. Sakaniwa and H. Shima, Phys. Rev. E **80,** 021103 (2009).
316 S. K. Baek, P. Minnhagen, H. Shima, and B. J. Kim, Phys. Rev. E **80,** 011133 (2009).
317 F. Sausset, G. Tarjus, and P. Viot, Phys. Rev. Lett. **101,** 155701 (2008).
318 A. Gendiar, R. Krcmar, S. Andergassen, M. Daniska, and T. Nishino, Phys. Rev. E **86,** 021105 (2012).
319 B. Yang, Z. Papic, E. H. Rezayi, R. N. Bhatt, and F. D. M. Haldane, Phys. Rev. B **85,** 165318 (2012).
320 E. Dobardzic, M. V. Milovanovic, and N. Regnault, Phys. Rev. B **88,** 115117 (2013).